Max-Planck-Institut
für Meteorologie

MAX-PLANCK-GESELLSCHAFT

International Max Planck Research School
on Earth System Modelling

The role of wind induced near-inertial waves on the energetics of the ocean

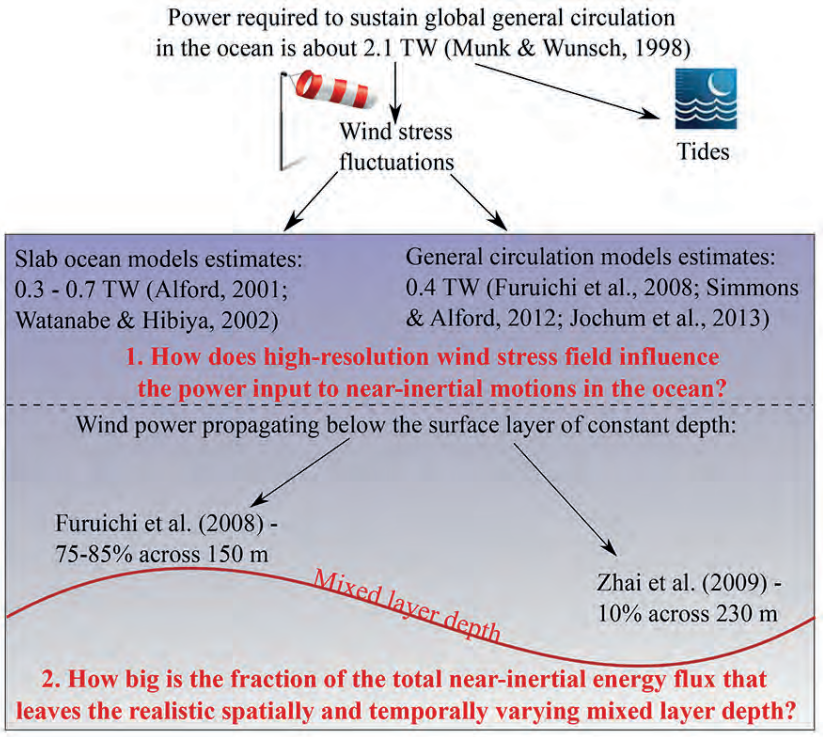

Antonija Rimac

Hamburg 2014

Berichte zur Erdsystemforschung
Reports on Earth System Science

160
2014

Hinweis

Die Berichte zur Erdsystemforschung werden vom Max-Planck-Institut für Meteorologie in Hamburg in unregelmäßiger Abfolge herausgegeben.

Sie enthalten wissenschaftliche und technische Beiträge, inklusive Dissertationen.

Die Beiträge geben nicht notwendigerweise die Auffassung des Instituts wieder.

Die "Berichte zur Erdsystemforschung" führen die vorherigen Reihen "Reports" und "Examensarbeiten" weiter.

Notice

The Reports on Earth System Science are published by the Max Planck Institute for Meteorology in Hamburg. They appear in irregular intervals.

They contain scientific and technical contributions, including Ph. D. theses.

The Reports do not necessarily reflect the opinion of the Institute.

The "Reports on Earth System Science" continue the former "Reports" and "Examensarbeiten" of the Max Planck Institute.

Anschrift / Address

Max-Planck-Institut für Meteorologie
Bundesstrasse 53
20146 Hamburg
Deutschland

Tel./Phone: +49 (0)40 4 11 73 - 0
Fax: +49 (0)40 4 11 73 - 298

name.surname@mpimet.mpg.de
www.mpimet.mpg.de

Layout

Bettina Diallo and Norbert P. Noreiks
Communication

Copyright

Max-Planck-Institut
für Meteorologie

MAX-PLANCK-GESELLSCHAFT

International Max Planck Research School
on Earth System Modelling

The role of wind induced near-inertial waves on the energetics of the ocean

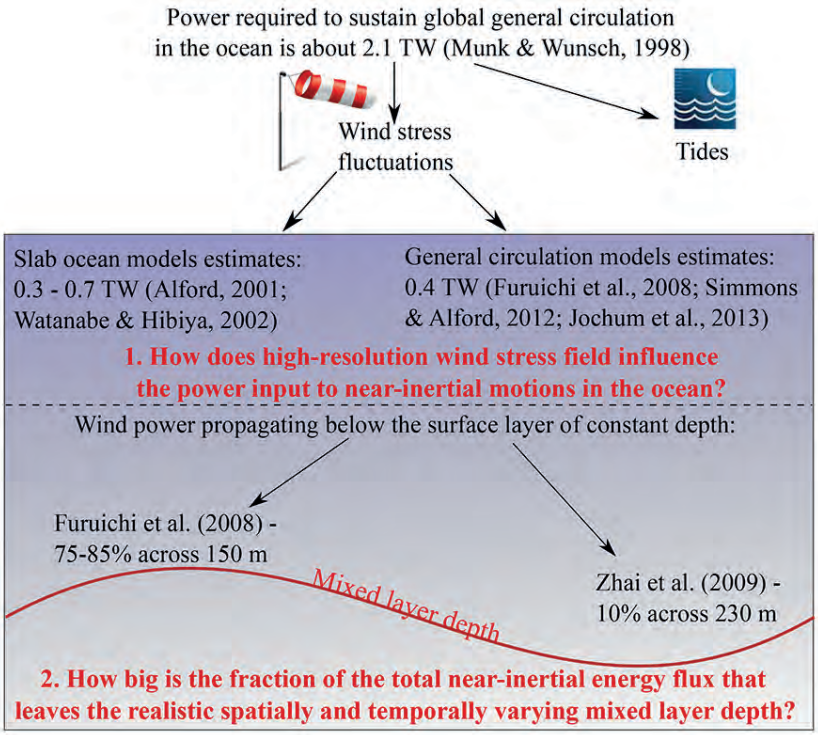

Antonija Rimac

Hamburg 2014

Berichte zur Erdsystemforschung
Reports on Earth System Science

160
2014

Antonija Rimac
aus Varaždin, Kroatien

Max-Planck-Institut für Meteorologie
Bundesstrasse 53
20146 Hamburg

Als Dissertation angenommen
vom Fachbereich Geowissenschaften der Universität Hamburg

auf Grund der Gutachten von
Prof. Dr. Carsten Eden
und
Dr. (habil.) Jin-Song von Storch

Hamburg, den 2. Juli 2014
Professor Dr. Christian Betzler
Leiter des Departments Geowissenschaften

ISSN 1614-1199

Abstract

In this thesis we investigate wind-induced near-inertial waves and their influence on the energetics of the ocean. This is a relevant subject as the ocean general circulation appears to be a mechanically driven phenomenon. The energy source needed to drive the meridional overturning circulation and induce deep-ocean mixing is mainly supplied by wind stress fluctuations and deep tides. The tidal component can account for approximately half of the required power, whereas the winds provide the remainder. One important way for winds to provide energy, is to generate near-inertial waves at the ocean surface. We are particularly interested in the influence of high-resolution wind forcing on the near-inertial kinetic energy and the wind-power input at the ocean surface. Our aim is to reduce the uncertainty in the estimates of the wind-power input to near-inertial motions based on slab ocean models and forced by wind stress forcing fields at low temporal and horizontal resolutions. Next, we are interested in a vertical structure of near-inertial kinetic energy and the fraction of the total near-inertial energy flux that leaves the realistic, temporally and spatially varying mixed layer and hence can be dissipated in the oceanic interior. Here, we consider the mixed layer as being dynamically more relevant structure than a surface layer of a constant depth. Another objective of our work is to provide a systematic analysis of near-inertial waves based on frequency and wavenumber spectra. In addition, we aim to quantify the horizontal and vertical propagation of near-inertial waves because our knowledge about the characteristics of near-inertial waves is still limited. Finally, we are interested in the difference between near-inertial kinetic energy simulated with Ocean General Circulation Model (OGCM) at two different resolutions, one at 1/10° horizontal resolution where a significant bulk of mesoscale eddies is resolved, and one at 0.4° horizontal resolution where mesoscale eddies are hardly resolved.

The wind-power input to near-inertial motions is studied using a global OGCM at 0.4° horizontal resolution. The model is forced by high- (1-hourly, at approximately 0.35° resolution) and low-resolution (6-hourly, at approximately 1.875° resolution) wind stress data. A change from low- to high-resolution wind forcing results in an increase in near-inertial kinetic energy by a factor of three, and raises the wind generated power input to near-inertial motions from 0.3 TW to 1.1 TW. Time and space filtering of the wind stress fields yield less near-inertial kinetic energy, with a larger decrease of the kinetic energy coming from time filtering. This strong sensitivity of the near-inertial kinetic energy and the wind-power input to the resolution of the used wind forcing points to a possible underestimation of the wind-generated energy available for deep-ocean mixing in previous studies based on wind data with low horizontal and temporal resolution.

The general properties of near-inertial waves are addressed using a global 1/10° OGCM. Vertical profile of the zonal mean of near-inertial kinetic energy shows that the energy is drained into the deep ocean. High levels of the near-inertial kinetic energy at the ocean surface, and the strong vertical energy propagation are seen in the mid-latitudes for both January and July 2005. Equatorial regions show strong near-inertial kinetic energy throughout the water column. Spatial

averages of near-inertial kinetic energy over areas with distinctly different mixed layer depths show energy enhancement at the base of the mixed layer. Energy enhancement suggests additional excitation of the near-inertial waves at the base of the mixed layer.

The fraction of the total wind-induced near-inertial energy flux leaving the mixed layer is estimated using a global 1/10° OGCM with a temporally and spatially varying mixed layer. Of 0.34 TW of the mean wind-power input to surface near-inertial motions, the mean near-inertial energy flux leaving the mixed layer amounts to 0.037 TW, resulting in a mean fraction of 10.8%. The fraction tends to decrease with increasing depth of the mixed layer and with increasing strength of wind stress variability, indicating the strong control of the turbulent dissipation inside the mixed layer on the fraction. Our results suggest a possible overestimation of the wind-power input to near-inertial waves and point towards the need for other energy sources for deep mixing.

Characteristic scales of near-inertial waves are addressed on a global domain and at several oceanic levels using vertical velocity simulated by the 1/10° OGCM. Wavenumber and frequency spectra, coherence and phase are used to analyze the variability, and horizontal and vertical propagation of near-inertial waves. Spectra of two-dimensional wavenumbers do not reveal a clearly defined wavelength, reflecting the fact that the crests and troughs of the simulated waves are oriented mainly in the zonal direction. Integrating the two dimensional wavenumber spectra over all zonal wavenumbers, we found the dominant meridional wavelengths of about 200-500 km. Frequency spectra show strong maximum near the local inertial frequency f and a lower maximum around the double inertial frequency $2f$. Spectra show that the highest energy does not occur exactly at f and $2f$ but at higher frequencies. This frequency shift is less prominent at 100 m than at 500 m, and for the areas further from the equator than for the areas closer to the equator. Frequency spectra do not show universal spectral shape near the inertial frequency. The estimated horizontal coherence scale at f is of about 20 to 240 km while the vertical coherence scale is about 60 m and longer. The analysis of phase suggests that near-inertial waves propagate horizontally towards the equator and vertically from the deep ocean towards its surface.

To evaluate the possible influence of mesoscale eddies on wind-induced near-inertial waves in the ocean, we compare experiments performed with the Max Planck Institute Ocean Model (MPIOM) at two different resolutions: one at 1/10° resolution, an experiment in which a significant bulk of mesoscale eddies is simulated, and the other at 0.4° resolution, an experiment which hardly resolves eddies. The model is forced by National Centers for Environmental Prediction reanalysis data (approximately 1.875° horizontal and 6-hourly temporal resolution). Given the length scales of the near-inertial waves of about 200 to 500 km, we expect that the long near-inertial waves simulated by the 1/10° model are by and large simulated by the 0.4° model, so that a comparison can indicate the influence of eddies on the simulated waves. Despite the differences in horizontal resolution used in the experiments, the spatial distributions of the near-inertial kinetic energy near the ocean surface and the total wind-power input to near-inertial motions at the surface show similarities likely related to the large-scale patterns of wind stress variability connected to mid-latitude storms. A change from the 0.4° experiment that hardly resolves eddies to the 1/10° experiment with strong eddy activity results in a threefold increase in near-inertial kinetic energy in the ocean interior. Vertical transects reveal high levels of near-inertial kinetic energy leaking into the deep ocean in the experiment with eddies. The strong sensitivity of the near-inertial kinetic energy to the presence of mesoscale eddies points to a possibility that the presence of mesoscale eddies plays a crucial role for vertical penetration of near-inertial waves.

Contents

1 Introduction

1.1 Motivation

In this thesis we deal with near-inertial internal waves in the world's oceans. Near-inertial waves are internal gravity waves in a stratified rotating fluid influenced by Earth's rotation, i.e., by the Coriolis force. Before going into details about near-inertial waves, their generation mechanism and their dissipation in the ocean interior, we would like to explain how they fit into the large scale picture of the ocean circulation and why they are worth studying.

The global Meridional Overturning Circulation (MOC) is a system of surface and deep currents enclosing all ocean basins. It is associated with a net meridional heat transport that warms high latitudes, it influences water-mass distribution and stratification, and also cycles and stores tracers like carbon dioxide in the deep ocean. The MOC is defined by four main branches of oceanic flows. In the Atlantic, the MOC consists of a warm and salty surface current that flows poleward where the water masses are cooled and become denser. The dense water then sinks into the deep ocean in localized regions, mainly in the Nordic Seas and in the Labrador Sea. Deep currents transport the deep and dense water southward along the American continent at depths of 2000-4000 m. Deep water crosses the equator and flows into the south polar area. There, the deep water forms a part of the Antarctic Circumpolar Current (ACC). After leaving the Southern Ocean and upwelling in the North Pacific, the deep waters return as part of surface currents through the Indonesian Archipelago into the Indian Ocean and round the Cape of Good Hope again into the Atlantic Ocean. The surface currents could follow some other paths from the Pacific into the Atlantic Ocean such as around the Cape Horn. A review on the MOC is given by Kuhlbrodt et al. (2007).

The strength of the MOC is closely bound to the distribution and intensity of deep-ocean mixing. If the vertical mixing in the ocean is too small or if there is no mixing, the deep ocean would fill up with cold and salty water with an equilibrium temperature of the deepest convecting element within a few thousand years (Munk, 1966, Baines and Turner, 1969). This can be traced

back to a theorem by Sandström (1908). Motivated by the oceanographic question of whether the poleward heat transport in the ocean is forced by meridional gradient of heating of the ocean surface, he performed a series of laboratory experiments (Coman et al., 2006). He analyzed under which conditions buoyancy forcing alone, applied at different depths, would lead to deep overturning circulation in a water tank. Sandström (1908) claimed that: "There must be heating as well as cooling if a sustained thermal circulation is to develop in the ocean." In his experiments the flow depended on the relative vertical position of a heating and a cooling source. When the heating source was placed at a deeper level than the cooling source, convection persisted, and the long-term circulation was confined to the depths between two sources (Coman et al., 2006). When the heat source was placed at shallower level than the cooling source or as in later experiment when the heating and the cooling source were at the same level (Sandström, 1916), a density stratification developed during an initial transient period, after which the circulation has vanished. In the conclusion he stated: "From these experiments we derive the conclusion that a sustained thermal circulation can occur only if the heat source is below the cold source."

To explain the MOC in the ocean, we need heating sources at depth (when no other external forces such as mechanical forcing by winds are present). The ocean is heated at the surface in the tropics where it expands, and it is cooled in the high latitudes where it contracts. According to the theorem by Sandström (1908, 1916), a deep circulation in such an ocean should not exist. On the other hand, the solar radiation can act as the external force. In the tropics where the fluid is heated, the solar radiation can penetrate down to 100 m, and since cooling only occurs at the ocean surface, the ocean would therefore be heated at the higher depth than cooled. In such case a very weak circulation would be significant only in a thin surface layer of the ocean, but the deep ocean would be of an uniform density. However, there are currents in the deep ocean, and in particular, the deep-water masses do upwell, return to the surface and thus close the overturning circulation. Therefore, there must be another heat source at depth. The gap between the theorem by Sandström (1908, 1916) and the real oceanic circulation was closed by Jeffreys (1925). He showed that when turbulent mixing is included, any horizontal density gradient, created by heating and cooling, induces a circulation. Mixing transports heat to large depths below the cooling levels, and a deep overturning circulation can develop. In that sense, for the oceanic MOC, we can conclude that the surface buoyancy fluxes are not the only factors that drive the circulation (Kuhlbrodt et al., 2007). Instead, the ocean is forced at its surface by atmospheric winds and through its volume by tides. Winds and tides result in turbulent mixing and are the ultimate drivers of the deep-oceanic circulation (e.g., Kuhlbrodt et al., 2007).

The questions that follow are, how much energy does the ocean need to sustain the deep circulation, and how much of this energy is supplied by winds and tides (and possibly other external energy sources such as geothermal heating through the sea-floor). Using the Levitus (1982) climatological data of oceanic density, Munk and Wunsch (1998) estimated that 2.1 TW of power are required to maintain the global deep-ocean mixing (i.e., bottom water had to be returned vertically up to about 1500 m) against 30 Sv ($1\,\mathrm{Sv} = 10^6\,\mathrm{m}^3/\mathrm{s}$) of deep-water formation. Their estimate was based on the global deep-water formation rate and a constant diffusivity. The global deep-water formation rate was first estimated by Munk (1966). He used the one-dimensional balance equation between vertical advection and vertical diffusion to determine a ratio between eddy-diffusivity and vertical velocity by profile fitting between temperature and salinity measurements as functions of depth. He also used observations of oceanic carbon to determine

eddy-diffusivity and vertical velocity separately. Although Munk (1966) estimated 25 Sv of deep-water formation rate, this value was considered numerically ill-posed (Munk and Wunsch, 1998). In their study, Munk and Wunsch (1998) used a nominal value of 30 Sv which is well within very broad limits of previous estimates (Munk and Wunsch, 1998, references therein). Another value of the power required for deep-ocean mixing was estimated by St.Laurent and Simmons (2006). They obtained their result by using a constant mixing efficiency and diffusivity, and a spatially varying stratification where a density structure on the global scale of the oceanic basins was assessed using the Levitus (1982) climatology. They obtained the total power required for mixing the entire water column of 3 TW.

As stated earlier, a number of authors (e.g., Kuhlbrodt et al., 2007, references therein) argued that the oceanic general circulation is a mechanically driven system. The possible sources of mechanical energy are winds, deep-water tides and geothermal heating through the sea-floor. Here, based on the studies by Munk and Wunsch (1998) and Wunsch and Ferrari (2004), we give a brief overview of the mentioned sources of mechanical energy for the sake of completeness. From our discussion it becomes clear what the main sources for the general circulation are and why the wind generated near-inertial waves, which are the topic of the present thesis, are important from the energetic point of view.

Wind origin: The wind can mix the ocean interior directly through excitation of near-inertial waves at the surface of the ocean, and indirectly through interaction of the wind-driven large-scale geostrophic motions with the bottom topography, or through radiation of wind-generated internal waves from the surface into the interior of the ocean (Munk and Wunsch, 1998). In the past decade, several studies have been carried out to assess the source of mechanical energy provided by the wind. These studies can be divided into two types. The first type equates the wind-power input as a scalar product of the wind stress and the surface flow (geostrophic + non-geostrophic). Using a 1/10° Ocean general circulation model For the Earth Simulator (OFES) based on primitive equations, and forced with daily wind stress from the National Centers for Environmental Prediction (NCEP) reanalysis (Kalnay et al., 1996), von Storch et al. (2007) showed that the integral of wind-power input over the sea surface of the model yields the net power supply of about 3.8 TW. About 2 TW of the total power can be attributed to the time-mean currents, while about 1.8 TW to the time-varying currents. Later, von Storch et al. (2012) addressed the Lorentz energy cycle using accumulated second moments produced by the Max Planck Institute Ocean Model (MPIOM) at a 1/10° resolution. They showed that the power supplied by the time-mean winds to the time-mean circulation (which includes geostrophic eddies and internal waves) amounts to 1.9 TW, and that supplied by the time-varying winds to the time-varying circulation amounts to 2.2 TW. Even though different models are used, both studies, von Storch et al. (2007, 2012), stressed the importance of time-varying winds in determining the wind-power input to the surface time-varying circulation.

The second type equates the wind-power input as a scalar product of the wind stress and the surface geostrophic flow (Wunsch, 1998, von Storch et al., 2007). When this power is integrated over the ocean area, it can be interpreted as the energy transferred via pressure work at the bottom of the Ekman layer (Stern, 1975). Wunsch (1998) used the Ocean TOPography EXperiment (TOPEX)/Poseidon satellite altimeter data (MacMillan et al.,

2004) and daily wind stress products from the NCEP reanalysis to estimate that about 1 TW of the wind-power is transferred to the general circulation. Using a 1/10° ocean model (OFES) and daily wind stress products from the NCEP reanalysis, von Storch et al. (2007) estimated about 1.1 TW of wind-power input to the surface geostrophic flows.

Through instabilities, energy in the general circulation is transferred to a vigorous eddy field. It is believed that the eddy field can loose its energy through friction at the bottom boundary layer and along the western boundaries (Zhai et al., 2010), and through internal wave generation at the bottom topography (Nikurashin and Ferrari, 2011). Small-scale topographic features act as a significant energy sink for the geostrophic flows, interaction of mesoscale eddies with the topography is an important mechanism for internal lee wave generation and the associated turbulent mixing in the ocean. Nikurashin and Ferrari (2010) estimated that about 0.2 TW or 20% of the wind-power input to surface geostrophic flows is converted into internal lee waves globally when geostrophic eddies flow over the smallâĂŘscale topography. The energy conversion into lee waves is largest in the Southern Ocean (about 0.1 TW) where bottom geostrophic flows are strong and topography is rough. Lee waves are characterized by short vertical scales which are highly non-linear and tend to break close to the generation site (Nikurashin and Ferrari, 2010). Based on idealized numerical simulations, Nikurashin and Ferrari (2010) estimated that up to 50% of the lee wave energy is dissipated locally within a kilometer of the topography.

Tidal origin: Tides are large-scale barotropic motions that move through the oceans in response to the forces exerted by the Moon and the Sun. Their spatial and temporal structure has been mapped accurately using satellite altimeter data. The total power coming from the Earth-Moon-Sun system is 3.7 TW (Dickey et al., 1994). A tiny portion of this power is dissipated in the atmosphere (about 0.02 TW) due to frictional processes, and in the solid Earth (about 0.2 TW) due to high temperatures in the upper mantle (Munk and Wunsch, 1998). From the remaining power, Kantha et al. (1995) computed that 2.6 TW is dissipated in the shallow marginal seas, based on the tidal currents and drag. This value is comparable to 2.5±0.05 TW derived from astronomical measurements (Munk and Wunsch, 1998). In the deep ocean with a rough topography, strong internal waves at tidal periods are commonly observed due to interaction of tides with the topography. The global energy conversion rate from barotropic to internal tides in the abyssal ocean was estimated to be 1 TW from altimetric observations (Egbert and Ray, 2000) and numerical experiments (e.g., Simmons et al., 2004). In the last few years, new estimates have been made on this topic. Green and Nycander (2012) used three different tidal conversion formulations and the TOPEX/Poseidon satellite altimeter data. They estimated the global energy conversion rate beneath 500 m of 0.91-1.35 TW. Recently, Müller (2013) used numerical simulations with the 1/10° MPIOM forced by the lunar-solar tidal potential and obtained an energy flux associated with the conversion from barotropic to baroclinic waves of about 1.2 TW beneath 1000 m.

Geothermal heating: Heat within the Earth's interior is a possible source of energy. Geothermal heat flux through the ocean bottom is closely related to the age of the bottom floor. Geothermal heat is released near the axis of the mid-ocean ridge as the newly formed sea-floor cools down. As the sea-floor ages, the heat flux declines. This rate of the potential

energy has a typical value of 0.05 TW (Huang, 1999, Wunsch and Ferrari, 2004).

So far we could see that the ocean circulation appears to be a mechanically driven phenomenon, and the energy source in the deep ocean is mainly supplied by tides and the wind that generates internal waves. Tidal mixing can account for approximately half of the required power, with the wind providing the remainder. However, it is still debatable how much of the wind-induced power goes to near-inertial waves, how much can be transported into the deep ocean via near-inertial waves and what are the main characteristics of these near-inertial waves. This thesis aims to answer these questions. Before addressing these questions, we first introduce near-inertial waves as an important mode of oceanic variability.

Near-inertial waves generated by wind stress fluctuations at the sea surface are fundamental motions in the oceanic mixed layer. Once generated, near-inertial waves propagate downward and equatorward away from their generation area. Near-inertial waves eventually decay because of the interaction with the internal waves of different frequencies or with the mesoscale flow field, or due to shear-driven turbulence at the base of the mixed layer (Alford, 2001).

Wind-driven near-inertial waves are an important contributor to the kinetic energy within the mixed layer as well as in the deep ocean. This can be demonstrated with the frequency spectrum of kinetic energy. Various databases contain over 2000 records of spectral kinetic energy estimates from a few representative locations in the deep open ocean. Qualitatively, however, there are some nearly universal features of such records. Figure 1.1, taken from Ferrari and Wunsch (2009), represents kinetic energy spectra of the horizontal velocity from instruments on a mooring over the Mid-Atlantic Ridge near 27° N. North Atlantic diurnal tides are comparatively weak, relative both to the semidiurnal tides in the North Atlantic and to the diurnal tides in other oceans (Munk and Wunsch, 1998). Therefore, it is possible to make a correct estimate of the energy contained near the local inertial frequency. All spectral estimates display a low-frequency flat band at periods longer than 1000 h. This band then falls into a quasi-geostrophic eddy-frequency band. A conspicuous energy peak exists around the inertial frequency f. The inertial frequency separates the eddy-frequency band from the high-frequency band. At frequencies higher than f there is another frequency band usually identified as internal waves. It can be seen that in all records, the peak centered near the inertial frequency is broader and higher (except when the instrument is at 3900 m) than the surrounding peaks and the one appearing at the M_2 frequency. The total energy content in the near-inertial peak compared to the rest of the internal wave frequency band in the upper ocean records is about 50%, while it is about 20% in the M_2 peak. In the lower record (at 3900 m) the energy content is reversed, meaning that about 57% is content in the M_2 peak while only 18% is content in the inertial peak when the comparison is made to the rest of the internal wave frequency band. Moreover, the spectral power at the near-inertial frequencies is marked by two distinct peaks located at O_1 and K_1 frequencies, indicating the dominance of diurnal tides over near-inertial waves at that depth. All estimates display a near power-law behavior with the typical slope in range of -0.8 to -1.5. This estimates deviate from the theoretical power-law by Garrett and Munk (1975). The extent to which the presented spectra are real and are the result of wave-interaction nonlinearities, as opposed to nonlinearities in the instruments or advection is not known (Ferrari and Wunsch, 2009).

Figure 1.2 illustrates the kinetic energy spectra of horizontal velocity at 122, 1525 and 3770 m simulated by the model used in the present study. The model does not include tides and is forced by 1-hourly wind stress at approximately 0.35° horizontal resolution. Spectra are calculated for

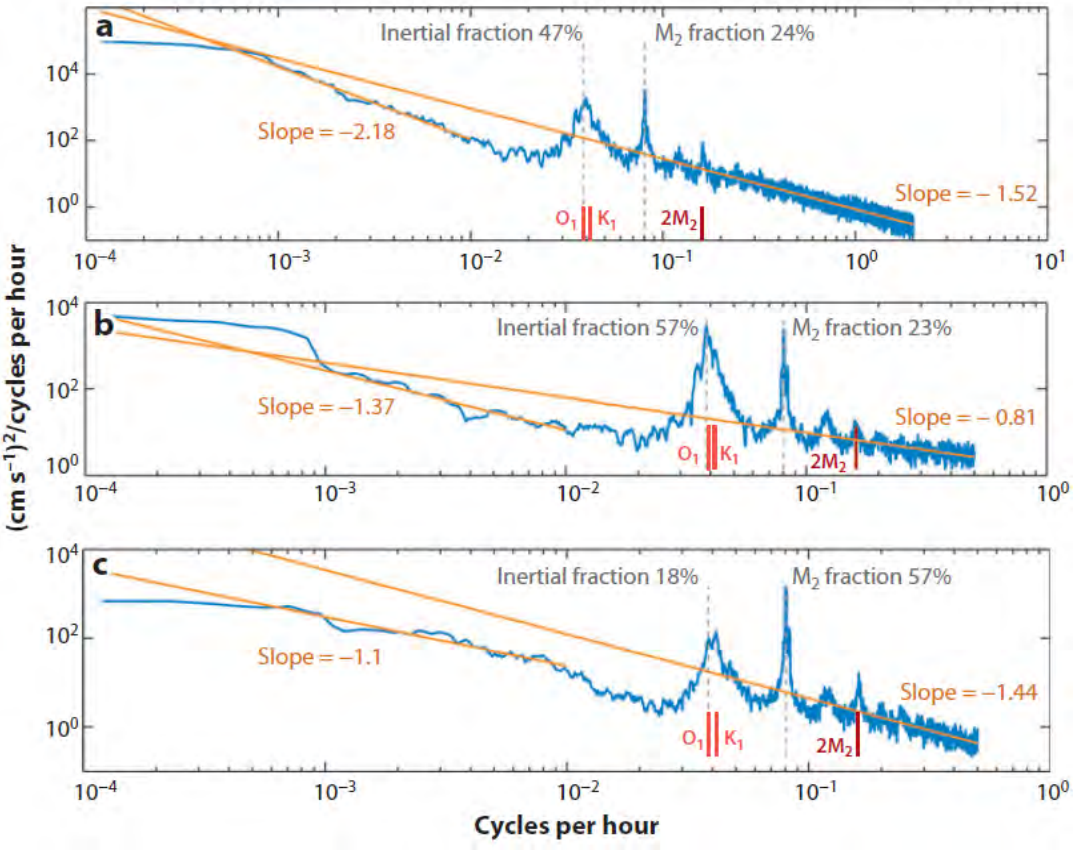

Figure 1.1: Kinetic energy spectral estimates from instruments on a mooring over the Mid-Atlantic Ridge near 27° N (Fu, 1981). The inertial, principal lunar semidiurnal M_2, and diurnal O_1 and K_1 tidal peaks are marked. The approximate percentage of energy of the internal wave band lying in the inertial peak and in the M_2 peak is noted. Least-squares power-law for periods between 10 and 2 h and for periods lying between 100 and 1000 h are shown. Some spectra show first overtone $2M_2$ of the semidiurnal tide. Instruments were positioned at (a) 128 m, (b) 1500 m and (c) 3900 m (near the bottom). Note that the vertical and horizontal axes scales differ. The energy spectrum from the deepest instrument (at 3900 m) shows a suppressed inertial energy, possibly due to a reflection of the waves from the nearby topography. The figure is taken from Ferrari and Wunsch (2009).

January-March 2005 for several grid points centered at 27° N in the Mid-Atlantic Ridge region. As in the observations (Ferrari and Wunsch, 2009), the simulated near-inertial waves are an important mode of variability in the ocean. Frequency spectrum calculated for 122 m shows broad peak and a relatively strong energy around the local inertial frequency f and around the double $2f$. The spectra calculated for 1525 and 3900 m show still broad peak but suppressed energy in the inertial band. Our model results show broad spectral peaks around f as in the observations, but lower energy level at all depths possibly due to lower horizontal resolution of the model, or due to shorter period used to estimate the spectra. At frequencies higher than 10 h our model results show differences compared to observations. These differences are mostly connected to lower variance and increased energy seen in spectrum at 1525 and 3900 m depth. The reason for this difference is not obvious and we can only speculate about the possible influences. One might be the lack of tides and inverse barometric effect in our model. Also, the variability could

be suppressed due to low-resolution of the forcing fields (only wind stress forcing was at high horizontal and temporal resolution) or due to numerics within the model. Overall, in both cases, in the model and in the observations, we can conclude that near-inertial waves represent the most energetic motions in the kinetic energy spectrum.

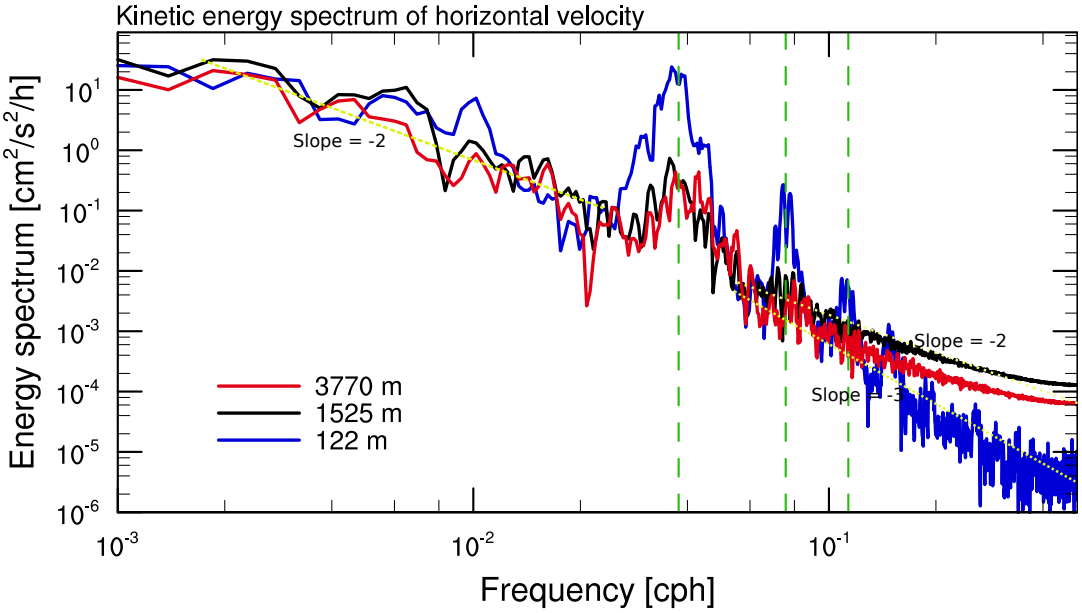

Figure 1.2: Kinetic energy spectra of horizontal velocity at 122 m (blue), 1525 m (black) and 3770 m (red). Velocity is taken from the model simulation with a high-resolution wind stress data (1-hourly temporal and approximately 0.35° horizontal resolution) used. Green lines represent (from left to right) the local inertial frequency of 0.0378 h^{-1} at 27° N and the frequencies of harmonics at 2f and 3f. Power-law, with the slope of about -3 for depth of 122 m and -2 for the rest, for periods between 10 and 2 h, and power-law of about -2 for periods between 1000 and 30 h is shown in yellow.

1.2 Brief overview of the past research

Previous estimates on the wind-power input to surface near-inertial waves have been made mostly using ocean models with simplified dynamics, so called slab ocean models, forced by realistic wind stress products at low temporal and spatial resolutions (e.g., 6-hourly temporal and about 1.875° horizontal resolution). Using slab ocean models, the wind-power input to surface near-inertial waves was estimated to be 0.3-0.7 TW (Alford, 2001, Watanabe and Hibiya, 2002, Alford, 2003a). Plueddemann and Farrar (2006) argued that slab ocean models do not allow for interaction between the mixed layer and the stratified ocean below. Therefore, these ocean models do not reproduce the kinetic energy balance for strong forcing events and they systematically overestimate the wind work. Also, one dimensional simulations, such as those form slab ocean models do not account for processes unrelated to the local wind forcing, such as local advection of the inertial flow by the mean currents that may change the amplitude and phase of inertial waves in the mixed layer (Plueddemann and Farrar, 2006). Hence, a more realistic representation using general circulation models based on primitive equations was needed. Using a general circulation model Furuichi et al. (2008), Simmons and Alford (2012), Jochum et al. (2013) obtained the total wind-power input to near-inertial waves of 0.4 TW. The possible impact of the temporal

resolution of the wind forcing was studied using a slab ocean model by Klein et al. (2004a) who attributed the increased near-inertial kinetic energy integrated over the water column to better temporal resolution of the wind forcing. On the other hand, Jiang et al. (2005) stressed the importance of the higher spatial resolution of the wind forcing to the increased near-inertial energy flux from winds to surface near-inertial waves. However, the combination of different spatial and temporal resolutions and their relative importance on the wind-power input remains unclear. In general, it is still debatable how big is the power provided by winds at the ocean surface.

One way for surface winds to provide power for deep-ocean mixing is via near-inertial waves that are excited at the surface of the ocean. Near-inertial wave energy is then partly dissipated in the oceanic mixed layer and partly transported via propagating near-inertial waves horizontally towards the equator and vertically into deep layers of the ocean. The energy that escapes the turbulent mixed layer can propagate more freely into the stratified ocean as internal gravity waves. When this waves break in the oceanic interior, they can contribute to the deep mixing. Therefore, the fraction of the total wind-induced near-inertial energy flux is important quantity for understanding the global general circulation and energetics of the ocean. Previous studies based on general circulation models (Furuichi et al., 2008, Zhai et al., 2009) estimated that only a small fraction, about 10-25%, of the wind power input passes through a surface layer of the ocean. In both studies the estimates were made for specific regions in the ocean (e.g., for the North Atlantic) and not for the global ocean. More importantly, the estimates were made across the oceanic level of a constant depth (e.g., across 230 m). However, the energy flux out of the mixed layer, rather than the energy flux through a fixed level as previously considered, is dynamically more relevant. Since near-inertial waves can only propagate freely below the mixed layer, and since the mixed layer varies spatially (and temporally) it is necessary to reexamine the wind-power input to surface near-inertial motions as well as the fraction of the wind-induced near-inertial energy flux leaving the oceanic mixed layer using a global ocean general circulation model at a high (1/10°) horizontal resolution. Moreover, it is important to address the influence of the wind stress and the depth of the mixed layer on the fraction of the total near-inertial energy flux that leaves the mixed layer because the wind stress influences mixing of momentum and therefore the dissipation of the near-inertial energy flux. Mixed layer depth signifies the turbulent oceanic layer that near-inertial waves have to pass through before being able to freely propagate into the deep ocean.

Characteristic scales of near-inertial waves have been studied mostly based on observations (e.g., Fu, 1981, Alford, 2010, Alford et al., 2012) and regional ocean models (e.g., Danioux et al., 2008, 2011). The strong variability of the velocity field has been shown to extend from the top to deep layers of the ocean throughout the winter season (Leaman and Sanford, 1975, Fu, 1981, Silverthorne and Toole, 2009, Alford et al., 2012) with two distinct maxima, one in the lower thermocline between 100 and 500 m and one in the deep ocean between 1700 and 2500 m (Danioux et al., 2008, 2011). Frequency spectra show a changing spectral shape around the local inertial frequency f and around the double $2f$. Fu (1981) characterized the changing spectral shape based on the physical environment where the measurement was taken (e.g., in the deep ocean around the Mid-Atlantic Ridge). The energy maximum in the frequency spectrum is not centered at f but slightly above (Fu, 1981, Simmons and Alford, 2012). Fu (1981) also estimated a horizontal coherence scale of about 60 km and a vertical coherence scale of about 200 m in the upper thermocline and about 1000 m in the deep ocean. Analyses of the spectral phase showed that near-inertial waves have in horizontal direction equatorward propagation and

in vertical direction they propagate from the top of the ocean to depth. In the deep ocean some standing wave features were observed (Fu, 1981). Based on the observational studies, it is known that near-inertial waves make up about half of the internal wave energy spectrum (Figure 1.1). Furthermore, based on numerical models, it has been estimated that the energy provided by the wind to near-inertial waves is a considerable fraction of the energy needed to sustain the global general circulation in the ocean. Therefore, it is necessary to understand some basic characteristics (e.g., wavelength, spectral shape and propagation) of these waves. To get a correct inference of the characteristics of near-inertial waves we need to extend the analysis from localized regions to the global domain.

The mesoscale eddy field strongly influences near-inertial energy in the ocean (Zhai et al., 2007). It can distort near-inertial wave structure and decrease its wavelength down to values of about 100 km and smaller (Klein et al., 2004b, Danioux et al., 2011). To quantify the influence of mesoscale eddies on the near-inertial wave energy, Zhai et al. (2005) used a channel model for the Southern Ocean. To make the clear difference between ocean influenced by eddies and ocean without that influence, they applied the storm forcing to the zonal wind stress or at the resting ocean, respectively. They showed that in the presence of mesoscale eddies the leakage of the near-inertial energy out of the surface layer is enhanced. Zhai et al. (2005) also showed the great importance played by anticyclonic eddies that act as pathways by which near-inertial energy enters the ocean and is ultimately available for deep-ocean mixing. Even though, the important role is played by mesoscale eddies on the near-inertial energy and its distribution in the ocean, the direct comparison between model at different resolutions, i.e., one that fully resolves eddies and one that does not, is still lacking.

1.3 Thesis objective

In this thesis we investigate near-inertial waves and their influence on the energetics of the ocean, in particular the energy that is available for deep-ocean mixing. We use a global Ocean General Circulation Model (OGCM) at a medium (0.4°) and a high (1/10°) horizontal resolution, forced by wind stress at low (approximately 1.875°, 6-hourly) and high (approximately 0.35°, 1-hourly) horizontal and temporal resolution respectively. Previous studies based on slab ocean models and later OGCMs indicate a large uncertainty in the magnitude of the wind-power input to near-inertial waves. By using state-of-the-art global OGCM forced by high- and low-resolution wind stress, we want to investigate the influence of resolution of the winds on the power input to near-inertial waves in the ocean. This will reduce uncertainty and provide a better estimate of the power available for deep-ocean mixing. This brings us to our first research question:

1.) *How does a high-resolution wind stress forcing field influence the power input to near-inertial waves in the ocean?*

Next, we want to investigate the vertical structure of near-inertial kinetic energy, the fraction of near-inertial energy flux that leaves the oceanic mixed layer, and the general properties of near-inertial waves. Here we are interested in the near-inertial kinetic energy distribution in the ocean's interior. We are also interested in the fraction of the wind-power input from the surface that is passed through the mixed layer and enters the stratified deep ocean. Generally, our knowledge about the characteristics of near-inertial waves is still limited. Here, we provide a more systematic

analysis based on frequency and wavenumber spectra. We also further quantify the horizontal and vertical propagation of near-inertial waves simulated with our ocean model. This leads us to our second set of research questions regarding the general properties of the wind-induced near-inertial waves:

2.) *What is the vertical distribution of the near-inertial kinetic energy? What is the fraction of near-inertial energy induced by winds that leaves the mixed layer? What are the characteristic scales of near-inertial waves and how do wind-induced near-inertial waves propagate horizontally and vertically?*

Finally, we analyze the difference in near-inertial kinetic energy obtained by using a global OGCM at two different horizontal resolutions, one at 1/10° and the other at 0.4° horizontal resolution. In general, scales of mesoscale eddies extend from 50 to 100 km (Danioux et al., 2008, 2011) while scales of near-inertial waves are about 200 to 600 km in meridional and up to a basin scale in zonal direction (Simmons and Alford, 2012). This means that a significant bulk of mesoscale eddies is resolved in 1/10° model while in 0.4° model eddies are hardy resolved (Jungclaus et al., 2013). Even though we cannot make a direct comparison between the OGCMs with and without eddies, we can make a qualitative comparison between two model resolutions, one that resolves mesoscale eddies (eddy-resolving model) and one which parametrizes mesoscale eddies (eddy-permitting model). Here, we will address our third research question:

3.) *How is the near-inertial kinetic energy in the ocean characterized in the eddy-permitting and in the eddy-resolving OGCM?*

1.4 Outline of the thesis

This thesis comprises five chapters and one appendix. Our primary results and research questions are structured regarding to the following basic ideas. Initially, we focus on near-inertial kinetic energy and wind-power input to near-inertial motions at the ocean surface. For this analysis, a global ocean general circulation model at a medium horizontal resolution is sufficient, but wind stress forcings at high temporal and spatial resolution are required. Following, we study the distribution of the near-inertial kinetic energy in the ocean interior and the energy flux across the realistic mixed layer depth. We analyze the general characteristics and propagation of near-inertial waves. Since for a correct simulation of general characteristics of near-inertial waves a high-resolution ocean model is needed, we use a 1/10° ocean general circulation model. In the end, we compare some of the results obtained in the previous two chapters using the same ocean general circulation model but at two different horizontal resolutions. Chapters 2, 3 and 4 form the main results of the thesis. Chapter 2 has already been published in *Geophysical Research Letters* (Rimac et al., 2013). Second part of Chapter 3 has recently been submitted to *Journal of Physical Oceanography*.

In Chapter 2 we address the first research question where we focus on understanding the influence of resolution of the wind stress on the wind-power input to near-inertial motions in the ocean. For this purpose, experiments with high-resolution wind forcing and experiments with modified wind forcing are performed. We use an ocean general circulation model, the Max Planck Institute Ocean Model (MPIOM) at a medium (0.4°) horizontal resolution driven by two

wind stress products, a low-resolution one from the National Centers for Environmental Prediction/National Centers for Atmospheric Research (NCEP/NCAR) reanalysis (6-hourly, at approximately 1.875° horizontal resolution; Kalnay et al., 1996) and a high-resolution one from Climate Forecast System Reanalysis (CFSR; 1-hourly, at approximately 0.35° horizontal resolution; Saha et al., 2010).

In Chapter 3 we address the second set of research questions. Since near-inertial waves are better simulated using a model at higher resolution, MPIOM at 1/10° horizontal resolution is used. This chapter is comprised of three parts. First, we study the vertical distribution of the near-inertial kinetic energy and second, the fraction of the wind-induced power that leaves the oceanic mixed layer. This we do with MPIOM, which simulates a realistic temporally and spatially varying mixed layer depth. Finally, we analyze the characteristic scales of near-inertial waves simulated with our ocean model, their propagation in the horizontal direction as well as into the interior of the ocean.

In Chapter 4 we address the third research question of the thesis. In this chapter we study the influence of the model resolution on the near-inertial kinetic energy in the ocean. We compare the results obtained from the 0.4° (eddy-permitting model) and 1/10° resolution model (eddy-resolving model). The model is forced by low-resolution NCEP/NCAR wind stress forcing.

In Chapter 5, we give a brief overview of the most important findings of the thesis and an outline of the possible implications of the thesis to future research on the topic of near-inertial waves in the ocean. In Appendix A we give a brief overview of the mathematical methods used to analyze our data.

2

The influence of the resolution of wind stress forcing on the power input to near-inertial motions in the ocean

In this chapter, which has been published as Rimac et al. (2013), the wind-power input to near-inertial motions is studied using a global eddy-permitting Ocean General Circulation Model (OGCM). The model is forced by high- (1-hourly, at approximately 0.35° resolution) and low-resolution (6-hourly, at approximately 1.875° resolution) wind stress data. A change from low- to high-resolution wind forcing results in an increase in near-inertial kinetic energy by a factor three, and raises the wind generated power input to near-inertial motions from 0.3 TW to 1.1 TW. Time and space filtering of the wind stress fields yield less near-inertial kinetic energy, with a larger decrease of the kinetic energy coming from time filtering. This strong sensitivity of the near-inertial kinetic energy and the wind-power input to used wind forcing points to a possible underestimation of the wind-generated energy available for deep-ocean mixing in previous studies based on wind data with low horizontal and temporal resolution.

2.1 Introduction and motivation

It has long been known that the ocean kinetic energy spectrum reveals a pronounced maximum near the inertial frequency (e.g., Munk, 1981). The near-inertial waves are excited by winds at the surface of the ocean, and are an important source for deep-ocean mixing. About 2 TW of power input, mainly supplied by winds and tides, are required for mixing to sustain the global general circulation in the ocean (Munk and Wunsch, 1998, Wunsch and Ferrari, 2004). However, the exact magnitude of the wind induced power input to near-inertial motions and the relative importance of tidal and wind forcing is still under debate.

The wind-power input to near-inertial motions has often been studied using realistic wind

The content of this chapter has been published in Geophysical Research Letters as Rimac et al. (2013).

stress products but simplified ocean dynamics (using slab ocean models), with varying estimates of the globally integrated rates: Alford (2001) found the wind-power input of 0.3 TW for oceans extending from 50° S to 50° N. He used wind stress calculated from a global National Centers for Environmental Prediction (NCEP) reanalysis surface winds at 2.5° horizontal and 6-hourly temporal resolution. Watanabe and Hibiya (2002), who used wind stress compiled by the Japanese Meteorological Agency at 1.875° horizontal and 6-hourly temporal resolution and introduced an amplification factor for inertial current velocity, found 0.7 TW. Alford (2003a) repeated his previous analysis but now using a frequency-dependent damping parameter and obtained a new estimate of 0.5 TW. He attributed the former, larger result from Watanabe and Hibiya (2002) to an inadequate sea-ice mask and a constant damping parameter. Plueddemann and Farrar (2006) pointed out that slab ocean models do not account for the energy lost due to vertical shear instability and therefore may systematically overestimate the wind work. Furthermore, slab ocean models miss the energy radiating into the deep ocean (Furuichi et al., 2008). Using an Ocean General Circulation Model (OGCM) at 1/7° resolution with the vertical mixing scheme by Mellor and Blumberg (2004) and forced by 6-hourly wind stress field at 1.25° resolution from Japanese reanalysis data, Furuichi et al. (2008) estimated 0.4 TW of wind-power input for a computational domain extending from 72° S to 72° N and divided into three subregions. Recently, Simmons and Alford (2012) found a global wind generated power input of 0.4 TW using an eddy-resolving OGCM with a shear-driven entrainment scheme (Jackson et al., 2008), a refined bulk mixed layer scheme (Hallberg, 2003) and forced with Common Ocean-ice Reference Experiment (CORE) atmospheric forcing fields (Griffies et al., 2009).

The wind-power input to near-inertial motions, for slab ocean models, is sensitive to the resolution of the wind stress field. For instance, Jiang et al. (2005) used 6-hourly wind stress fields and found an increase in the energy flux from the wind to ocean inertial motions with increasing horizontal resolution. Klein et al. (2004a) pointed out on the importance of temporal resolution by showing a 20% decrease in the total near-inertial kinetic energy integrated over the water column when wind stress fields are changed from 3- to 6-hourly mean values. D'Asaro (1985) and Niwa and Hibiya (1999) showed that insufficient time resolution of the wind stress field may lead to aliasing errors.

These different estimates indicate the need for systematically reconsidering the wind-power input using a realistic OGCM and wind stress fields at higher temporal and spatial resolutions. We use the Max Planck Institute Ocean Model (MPIOM) with two different wind stress forcing fields: one from the National Centers for Environmental Prediction/National Centers for Atmospheric Research (NCEP/NCAR) reanalysis and one from the Climate Forecast System Reanalysis (CFSR). We address the following questions: Is the kinetic energy of near-inertial motions enhanced when high-resolution wind stress forcing fields are used? If so, is this due to a higher level of overall wind variability or due to a better spatial or temporal resolution of the wind forcing? And finally, what is the magnitude of the wind-power input to near-inertial motions?

2.2 The ocean model and the wind forcing

The ocean model

In this thesis we use integrations from MPIOM (Marsland et al., 2003, Jungclaus et al., 2013). MPIOM is a global OGCM based on the primitive equations, thus including the hydrostatic and Boussinesq approximation (Olbers et al., 2012). A primitive-equation model can correctly simulate long near-inertial motions that fall into the hydrostatic regime (Gill, 1982, Simmons and Alford, 2012). However, for a better simulation of the vertical propagation of the near-inertial waves, higher spatial resolution of the model is necessary. In this chapter we use the model set-up based on a TriPolar grid at 0.4° horizontal resolution and with 40 vertical levels (TP04L40). Thickness of the vertical levels increases from 12 m near the surface to several hundreds of meters in the deep ocean.

For the vertical mixing and diffusion, MPIOM uses the Richardson number-dependent mixing scheme (Pacanowski and Philander, 1981). In their study, Pacanowski and Philander (1981) included non-constant parametrization of vertical eddy viscosity and eddy diffusivity depending on the Richardson number. They showed that vertical eddy viscosity and eddy diffusivity vary considerably in the tropical oceans and have large values in the surface mixed layer, but have small values below the thermocline. This mixing scheme, in its classical form, underestimates turbulent mixing close to the ocean surface (Marsland et al., 2003). Therefore an additional parametrization for wind induced stirring is included. The near-surface wind mixing is a function of a local 10 m wind speed, it decays exponentially with depth and depends on a local static stability. The surface wind mixing is also reduced in proportion to the fractional sea-ice cover. The mixing scheme used in MPIOM provides a more realistic dissipation of near-inertial energy in the upper ocean and a more realistic Mixed Layer Depth (MLD) than a slab ocean model with a simple Rayleigh drag does.

The MLD is diagnosed from the potential temperature and salinity fields using a potential density criterion defined by Levitus (1982). The MLD is defined as the depth at which a density change from the ocean surface of 0.125 kg/m^3 has occurred. Figure 2.1 shows the zonal mean of the MLD. The MLD is obtained from an annual mean of potential temperature and salinity fields taken from the experiments with NCEP (purple line) and CFSR (green line) wind stress data (for detailed analysis see next subsection), from NCEP climatological data (red line) and from Polar science center Hydrographic Climatology (PHC, black line, Steele et al., 2001). We calculate MLD from climatological data (NCEP and PHC climatology) using the annual mean of potential temperature and salinity fields of years 1948 to 2000 into account, while for the rest (experiments with NCEP and CFSR wind data) we use the annual mean of year 2005 into account. The simulated mean MLD in our experiments is in broad agreement with the one derived from the PHC climatology. Some differences between observations (PHC climatology) and simulated data appear around 50° S and 40°-50° N because of strong negative temperature and salinity biases seen there (Jungclaus et al., 2013).

The wind stress data

In this chapter we drive the ocean model with two different wind stress forcing fields:

1. NCEP wind stress: 6-hourly wind stress forcing taken from the NCEP/NCAR reanalysis on

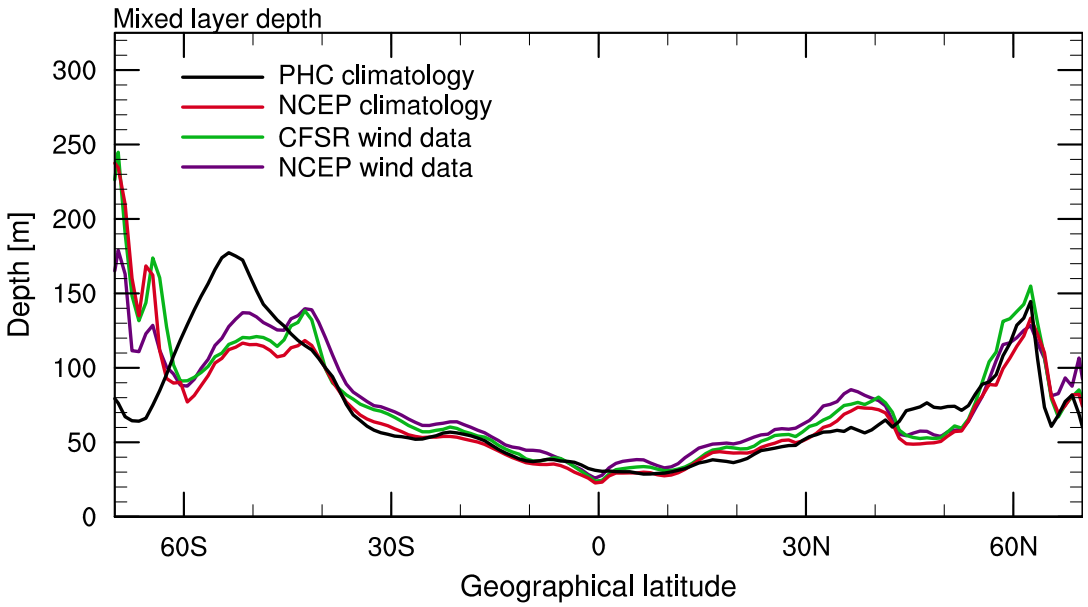

Figure 2.1: Zonal mean Mixed Layer Depth (MLD) calculated using sigma-t density criterion (Levitus, 1982). MLD is defined as the depth at which a change from the surface density of 0.125 kg/m^3 has occurred. Color lines represent different data used to calculate the MLD. For this calculation we use two model simulations and two climatological data. Purple and green lines represent the results from model simulations performed using NCEP and CFSR wind stress data, respectively. Red and black lines represent the results from NCEP and PHC climatological data.

T63 grid (approximately 1.875° horizontal resolution; Kalnay et al., 1996). Data is available for period between 1948 to the present day.

2. CFSR wind stress: 1-hourly wind stress forcing taken from the CFSR reanalysis on T383 grid (approximately 0.35° horizontal resolution; Saha et al., 2010). Data is available for period between 1979 to 2010 but we concentrate only on the year 2005.

So far we have mentioned that NCEP and CFSR wind stress data differ only in their temporal and spatial resolutions. In additional analysis, we want to see whether the data are comparable in some basic features or they show significant differences (and therefore cannot be used in parallel to investigate near-inertial motions). To compare NCEP and CFSR wind stress data we show the spatial distributions of the time mean value and the variance. We also use a frequency spectrum to show a frequency distribution of the used wind data.

Figure 2.2 displays the global distribution of mean value of the zonal component for NCEP (Figure 2.2a) and CFSR (Figure 2.2b) wind stress data, and their respective zonal means (Figure 2.2c and 2.2d). The wind stress is taken as a mean value of the year 2005. The result is dominated by positive values (eastward wind stress) in the Southern Ocean and in the Kuroshio and Gulf Stream extension regions. The tropics are regions of negative values (westward wind stress) by the mean wind. In Figure 2.3 we show the global distribution of the meridional component for NCEP and CFSR wind stress data (Figure 2.3a and 2.3b, respectively), and their respective zonal means (Figure 2.3c and 2.3d) calculated for the year 2005. Meridional components are weaker than the zonal components. Large positive values are seen along west coast of Africa, Australia and South America (mostly in the Southern Hemisphere between 10° and 30°). Small positive values can be seen in the sub-polar gyre regions of the North Pacific and the North Atlantic.

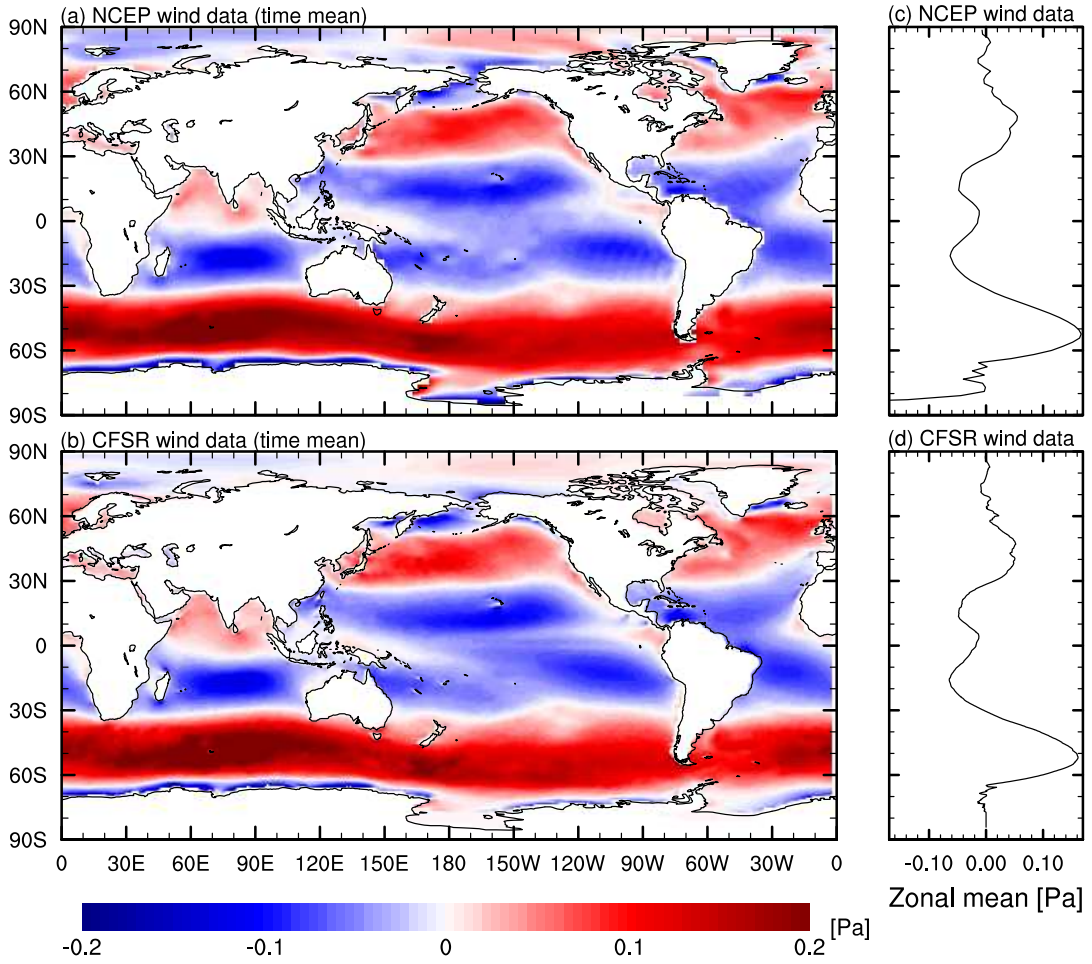

Figure 2.2: Yearly mean value calculated for a zonal component of (a) NCEP and (b) CFSR wind stress data. Zonal mean calculated from a yearly mean value of the zonal component of (c) NCEP and (d) CFSR wind stress data. The calculation is done for the year 2005.

Negative values occur in the Kuroshio and Gulf Stream regions and along the west coast of North America. Both figures do not show a big difference between two wind stress data.

Figure 2.4 represents the global distribution of variance calculated for the zonal component of NCEP (Figure 2.4a) and CFSR (Figure 2.4b) wind stress data, and their respective zonal means (Figure 2.4c and 2.4d). The global distributions of variance are calculated for the year 2005. We show only the result for zonal component of wind stress because there is no clear difference in variance between zonal and meridional component. It can be seen that the highest variability occurs in the storm track regions, between 30° and 60° geographical latitudes. Also, there is a high variability in the North Atlantic sub-polar gyre region, around the southern tip of Greenland. The tropics are regions of very low variability. The variance averaged globally is about 15% higher when calculated for CFSR than when calculated for NCEP wind stress data ($0.0171\,\mathrm{Pa}^2$ from CFSR compared to $0.0146\,\mathrm{Pa}^2$ from NCEP wind stress data). Zonal mean also reveals that the variance of CFSR wind stress data is higher than the variance of NCEP wind data on both hemispheres. Possible reason for this difference is in temporal and spatial sampling of the used data.

In Figure 2.5 we give spectral estimates of zonal (blue) and meridional (red) components of NCEP (dashed line) and CFSR (solid line) wind stress data. The calculation is done for the year

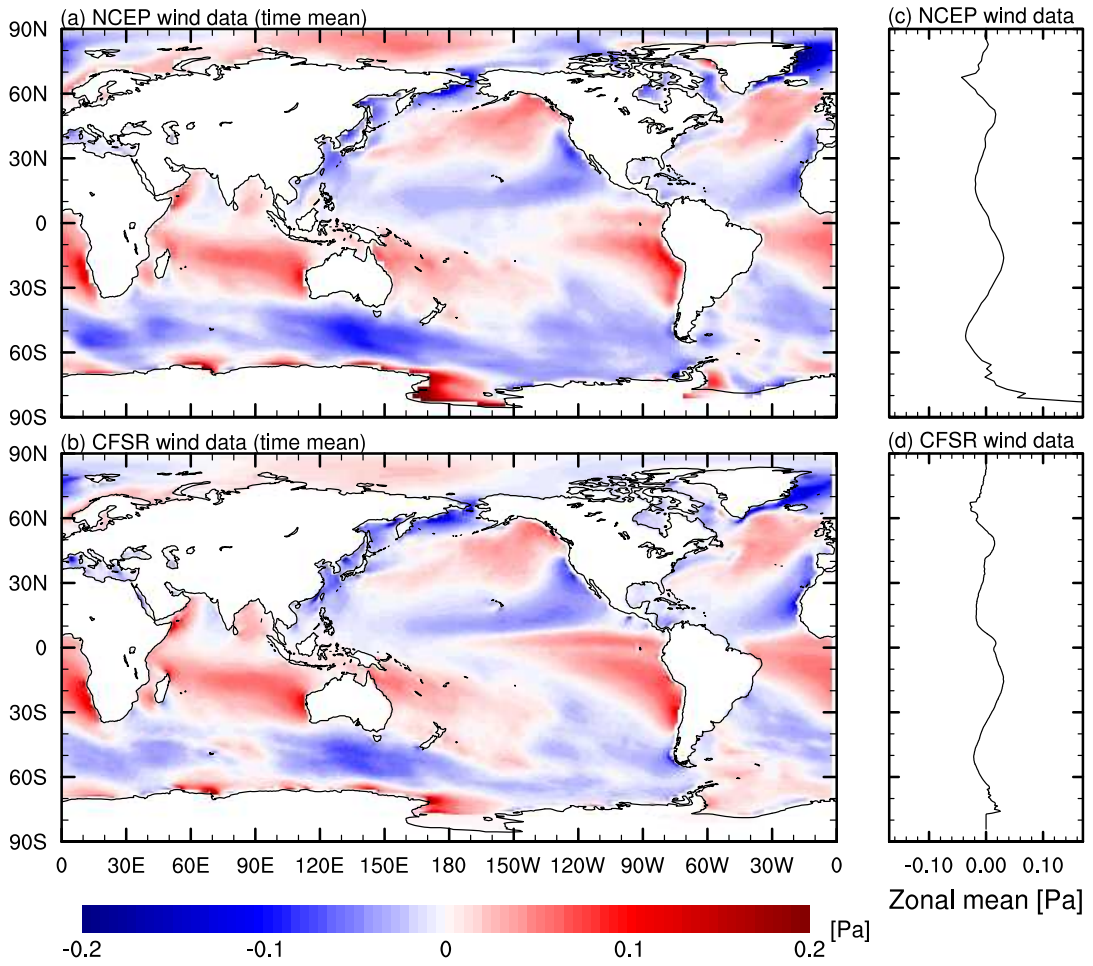

Figure 2.3: Yearly mean value calculated for a meridional component of (a) NCEP and (b) CFSR wind stress data. Zonal mean calculated from a yearly mean value of the meridional component of (c) NCEP and (d) CFSR wind stress data. The calculation is done for the year 2005.

2005. The energy spectra are calculated along 41° N in the Pacific region. NCEP wind stress data are sampled as 6-hourly and their Nyquist frequency is at $0.083\,\mathrm{h}^{-1}$. It can be seen that the spectra of NCEP and CFSR wind data are very similar for both components. One difference can be seen though due to different temporal sampling of NCEP and CFSR wind stress data. The energy spectrum of CFSR wind stress data shows variability at frequencies higher than $0.083\,\mathrm{h}^{-1}$ while the energy spectrum of NCEP wind stress data doesn't. The absence of high frequency values from NCEP wind stress data might influence the difference in wind variance seen in Figure 2.4.

The basic statics of NCEP and CFSR wind stress data are comparable, except that CFSR wind stress data has larger variance. In the zonal mean the increase in variance from NCEP to CFSR wind stress data is only moderate (about 15%). This difference can happen due to different temporal sampling of the used data and the absence of energy at high frequencies seen in the energy spectrum of the NCEP wind stress data.

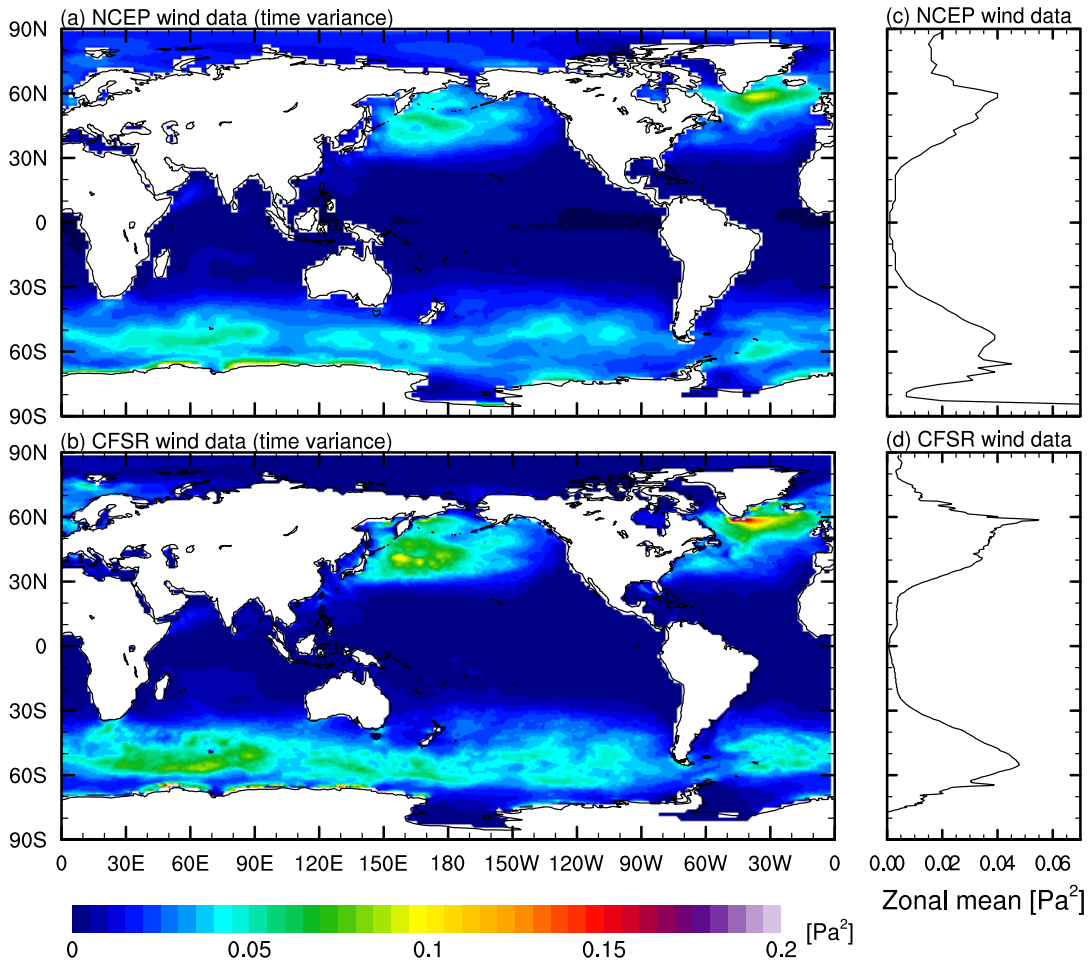

Figure 2.4: Yearly variance calculated for a zonal component of (a) NCEP and (b) CFSR wind stress data. Zonal mean of yearly variance calculated for the zonal component of (c) NCEP and (d) CFSR wind stress data. The calculation is done for the year 2005.

2.3 Comparison of model velocity and near-inertial energy with observations

In order to get an objective insight in the validity of our simulations, we compare the simulated velocity and the near-inertial kinetic energy with observations. We chose these variables, velocity and near-inertial kinetic energy, because velocity can be easily measured at various regions while the near-inertial kinetic energy can be calculated from the velocity. We compare the simulated zonal and meridional velocity at 6 m depth with observations from Plueddemann and Farrar (2006), at the locations where the observations are available (e.g., at 10° N, 125.4° W). The amplitude of velocity, simulated in the experiment with CFSR wind stress data for the Pacific region, is up to 0.3 m/s in zonal and 0.16 m/s in meridional direction. This is consistent with the mentioned observations where the mixed layer currents of 0.2-0.5 m/s are common. Additional comparison is made for the four observational points in the North Atlantic where the zonal component of the observed and velocity simulated using a slab ocean model for the years 1982, 1986, 1991 and 1992 are analyzed. Even though we only analyze year 2005 and cannot make a direct comparison with these observations, we can argue that the basic statistics of zonal velocity in the experiment with CFSR wind stress data are comparable to the observations.

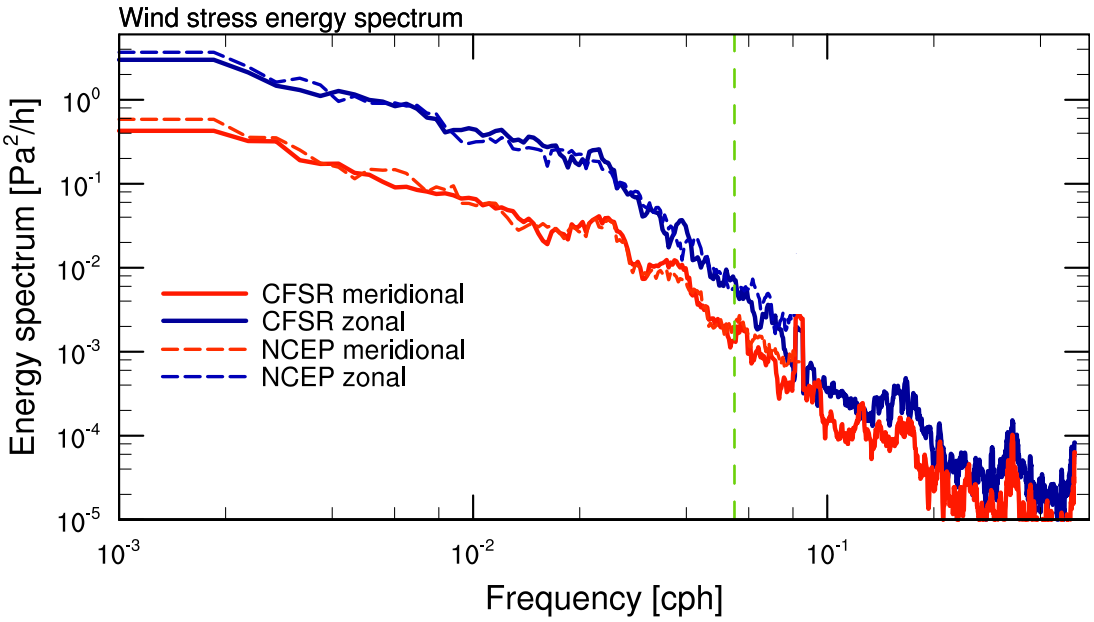

Figure 2.5: Energy spectra of zonal (blue) and meridional (red) component of NCEP (dashed line) and CFSR (solid line) wind stress data. Spectra are calculated along 41° N, in the Pacific sector. Green line represents the local inertial frequency at 0.0547 h^{-1}.

We calculate a rotary spectrum (Figure 2.6, more details on rotary spectrum are given in Appendix A.1) of the velocity simulated using CFSR wind stress data. The spectrum is calculated using several grid points centered at 10° N, 125.4° W to be consistent with Plueddemann and Farrar (2006). It can be seen that the spectrum is dominated by clockwise rotation at a local inertial frequency f, indicating that anticyclonic near-inertial motions are the dominant motions in the Northern Hemisphere. The variance in the simulated rotary spectrum is almost equal to the one in the rotary spectrum obtained from observations. For the comparison, in Figure 2.7 we show the rotary spectrum from Plueddemann and Farrar (2006). The spectrum is dominated by near-inertial motions at a local inertial frequency of 0.0145 h^{-1}. The spectrum shows an isolated, clockwise rotating peak between $0.9f$ and $1.1f$, with variance five to ten times larger than surrounding peaks.

The globally averaged near-inertial near surface velocity obtained in the experiment with CFSR wind stress data is around 9 cm/s. It is calculated as the variance of the anticyclonically rotating velocity vector sub-sampled every 3 hours at 17 m depth, and integrated over a near-inertial frequency range defined as in Chaigneau et al. (2008). This result is comparable to the observations by Chaigneau et al. (2008) who obtained a globally averaged near-inertial velocity of about 10 cm/s.

Additionally, we calculate the near-inertial variance for different ocean basins (Figure 2.8), and compare our simulations with the observations by Elipot and Lumpkin (2008). Figure 2.8 shows zonally averaged near-inertial variance of the anticyclonically rotating velocity vector for the experiment with CFSR (Figure 2.8a) and the experiment with NCEP (Figure 2.8b) wind stress data. The globe is divided into latitudinal bands of 2.5°. The variance is calculated for each latitudinal band by integrating the spectra between 0.9 times the minimum inertial frequency in this band and 1.1 times the maximum inertial frequency. We present the result for Pacific (green), Atlantic (blue) and Indian (black) Ocean. Both experiments show similarities with the

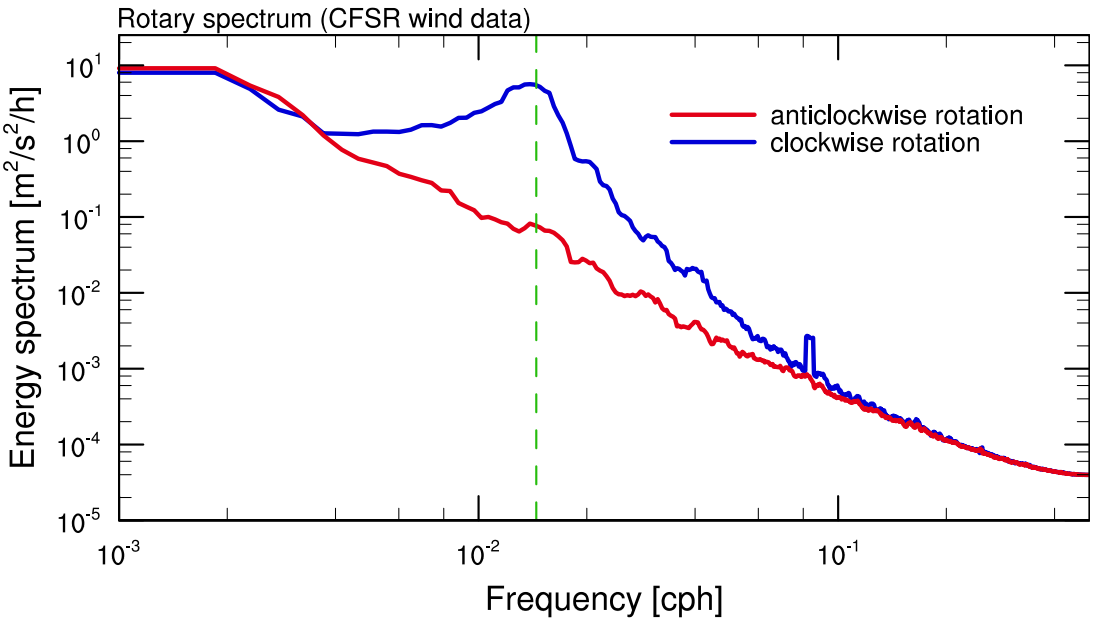

Figure 2.6: Rotary spectrum of the velocity vector calculated for the experiment with CFSR wind stress data. We calculate the rotary spectrum as a mean of all four seasons during the year 2005 for clockwise (blue) and anticlockwise (red) rotation separately. The green line represents an inertial (Coriolis) frequency calculated for 10° N, which also represents one of the observational sites from the study by Plueddemann and Farrar (2006).

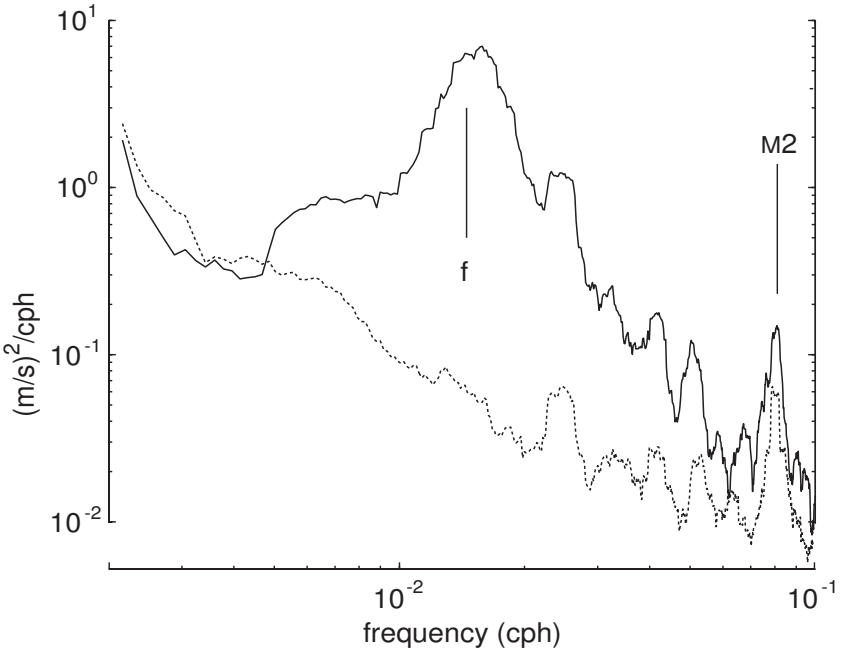

Figure 2.7: Rotary spectrum of mixed layer currents estimated for clockwise (solid) and anti-clockwise (dashed) components for the observational site at 10° N, 125.4° W. The semidiurnal tide M_2 and the local inertial frequency are noted by vertical lines. Figure is taken from the study by Plueddemann and Farrar (2006).

observations from Elipot and Lumpkin (2008). For the comparison, we show the Figure 2.9 taken from Elipot and Lumpkin (2008). Figure 2.8 and 2.9 show that there is a maximum of the near-inertial variance between 20° and 45° in all ocean basins and at both hemispheres. The near-inertial variance is higher in the North Pacific than in the North Atlantic between 30° and 40° N (this is not seen in the Southern Hemisphere). The magnitude of the near-inertial variance in the experiment with CFSR wind stress data is comparable to the observations, while in the experiment with NCEP wind stress data, the magnitude of the near-inertial variance is lower due to a low sampling frequency of the used wind stress data.

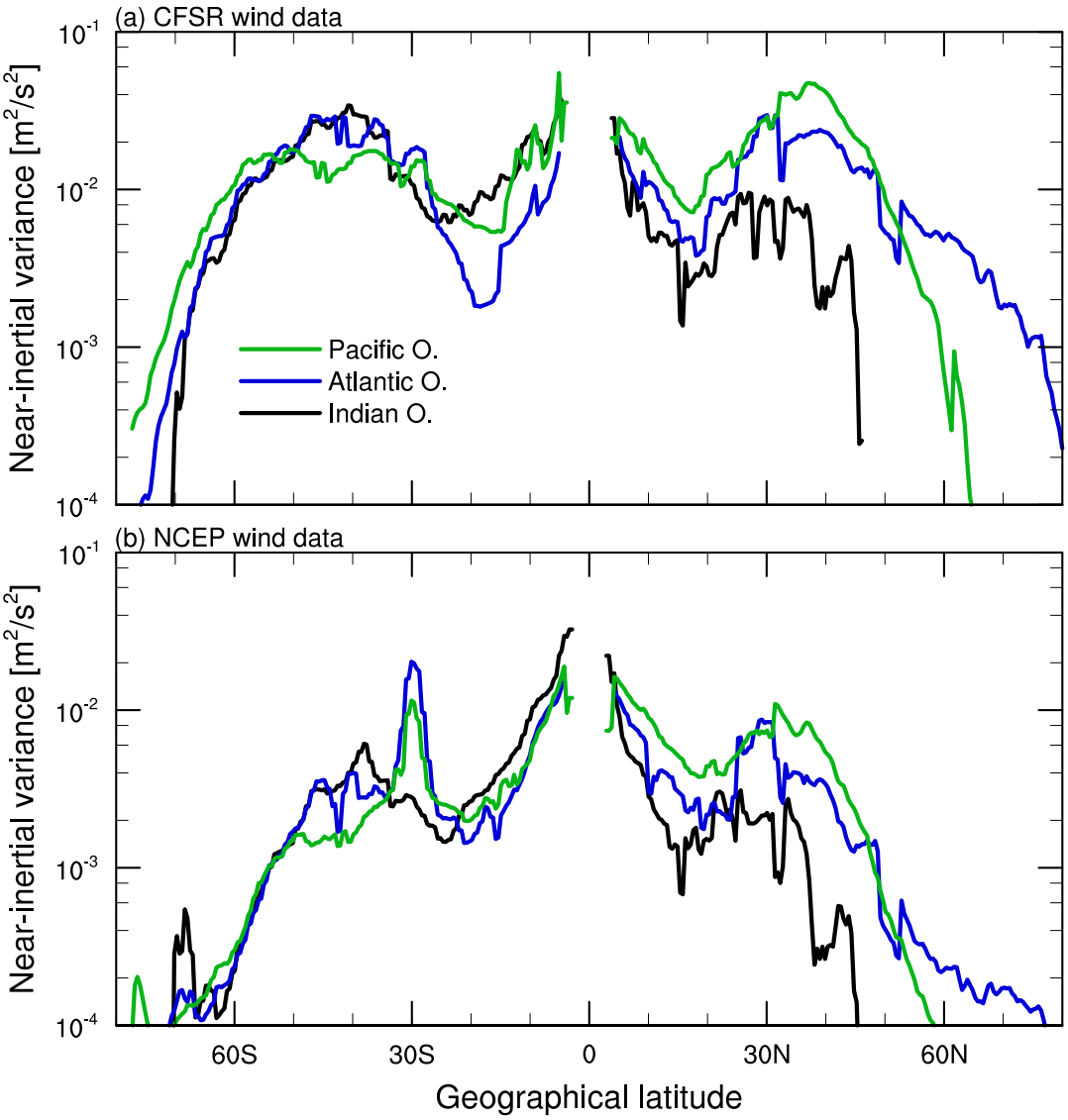

Figure 2.8: Zonally averaged near-inertial variance calculated from bandpass filtered model velocities at 17m in the near-inertial frequency band. Since the globe is divided into latitudinal bands of 2.5°, the near-inertial variance is integrated over an interval of 0.9 times the minimum inertial frequency in this band and 1.1 times the maximum inertial frequency. Velocities are taken from the experiments with (a) CFSR and (b) NCEP wind stress data. Calculation is done for the Pacific (green), Atlantic (blue) and Indian (black) Ocean.

Velocity measured at various regions from the study by Plueddemann and Farrar (2006) and Chaigneau et al. (2008) is comparable to the one obtained in our simulations performed by forcing

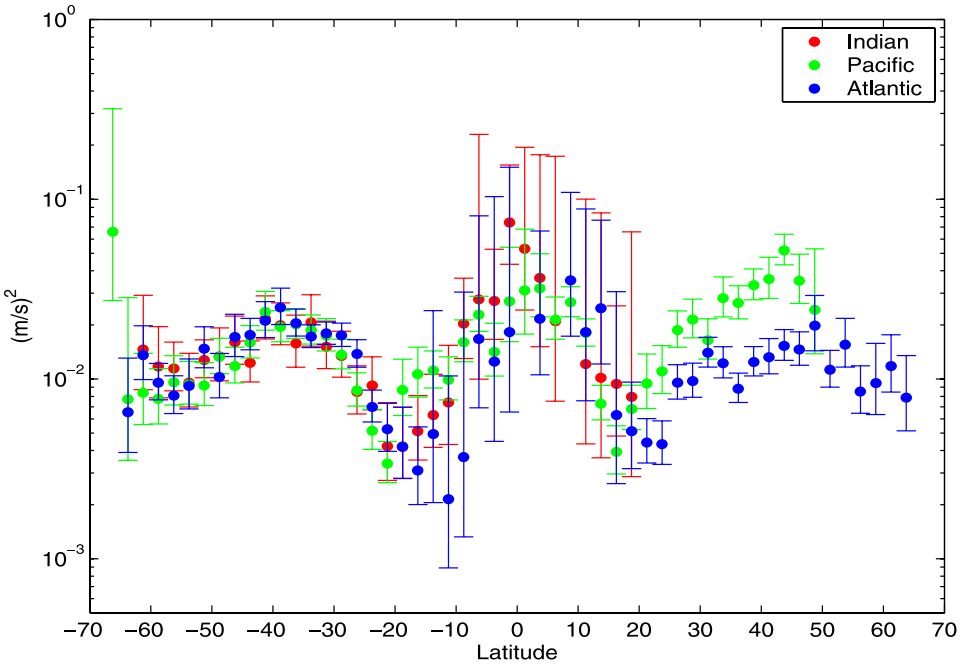

Figure 2.9: Drifter velocity variance in the near-inertial frequency band for the Indian (red), Pacific (green) and Atlantic (blue) basins. Since the globe is divided into latitudinal bands of 2.5°, the near-inertial variance is integrated over an interval of 0.9 times the minimum inertial frequency in this band and 1.1 times the maximum inertial frequency. Error bars are derived from the 95% confidence intervals of the rotary spectrum estimates. The figure is taken form Elipot and Lumpkin (2008).

MPIOM with CFSR wind stress data. Rotary spectrum calculated for one observational site at 10° N in the Pacific Ocean is similar to the rotary spectrum from the experiments with CFSR wind stress data. Near-inertial variance calculated for all ocean basins and for experiments with both NCEP and CFSR wind stress data shows similar zonal distribution to the near-inertial variance calculated from observed velocities by Elipot and Lumpkin (2008). One difference is evident though. The near-inertial variance from the experiment with NCEP wind stress data is lower due to low temporal sampling of the used wind stress data.

2.4 The experiments designed to identify the relative role of temporal and spatial resolution of the wind forcing

To assess the effects of the resolution of the wind forcing, a series of experiments are performed by driving MPIOM with the same surface fluxes of heat and fresh water but different wind stress forcing (Table 2.1). The heat and fresh water (precipitation minus evaporation) fluxes are derived from the 6-hourly NCEP reanalysis on T63 grid (1.875° resolution; Kalnay et al., 1996). The fresh water flux is supplemented by daily river discharges on T106 grid (1.125° resolution). Experiment NCEP is forced by 6-hourly wind stress on T63 grid (Kalnay et al., 1996). Experiment CFSR is forced by 1-hourly wind stress on T383 grid (0.35° resolution; Saha et al., 2010). The remaining experiments are divided into two sets. The first set (experiment TFX: TF04, TF06, TF12 and TF24) uses the CFSR wind stress field at its original spatial resolution but temporally filtered by sampling the CFSR wind stress every 4, 6, 12 and 24 hours, respectively. The second set

(experiment SFX: SF0.7, SF1.1, SF1.8 and SF2.8) uses the CFSR wind stress field at its original temporal resolution, but spatially filtered to a coarser grid using nearest neighbor interpolation. The resulting wind stress fields have resolutions of about 0.7°, 1.125°, 1.875° and 2.8°, respectively. These filters (sub-sampling and nearest neighbor) essentially preserve the total variance of the CFSR winds (appendix in von Storch et al., 2007), allowing for a better comparison of the experiments SFX with the experiments TFX. The different forcing fields are linearly interpolated in space using weighted averages of the four nearest grid points to the model grid and in time from the reanalysis to the model time step of 1-hour.

Table 2.1: Experiment name, temporal and spatial resolution of the wind stress data used to force the ocean model MPIOM. In experiments TFX we use temporally filtered CFSR wind stress data and in experiments SFX we use spatially filtered CFSR wind stress data.

	Experiment name	Temporal resolution	Spatial resolution
	NCEP	6-hourly	T63 grid
	CFSR	1-hourly	T383 grid
TFX:	TF04	4-hourly	T383 grid
	TF06	6-hourly	T383 grid
	TF12	12-hourly	T383 grid
	TF24	daily	T383 grid
SFX:	SF0.7	1-hourly	0.7°grid
	SF1.1	1-hourly	1.125°grid
	SF1.8	1-hourly	1.875°grid
	SF2.8	1-hourly	2.8°grid

The reduction of wind stress variance in experiments TFX and SFX, relative to experiment CFSR, are shown in Figure 2.10a and 2.10b. In all experiments, variance changes due to the differently filtered winds are moderate and mostly below 30%. Two features are evident. First, the variance changes in wind stress field are larger in experiments TFX than in experiments SFX. Second, for experiments TFX, the variance changes are larger at the mid- and high-latitudes than in the tropical and subtropical regions.

Although we make a separation in spatial and temporal variations of the wind field, it is possible that some small-scale features, after being advected by the mean wind, appear as temporal variability. Our filtering method cannot separate such different sources of variability. By filtering out the spatial or the temporal variations in the wind forcing and allowing the ocean to freely respond to this, we are only able to assess the relative importance of temporal and spatial variations of winds in generating near-inertial motions in the ocean, regardless of their generation mechanism. The experiments are carried out for the period of 2004 to 2005. Hourly output is stored. For the analysis we use the last year (2005) and a first model level (at 6 m).

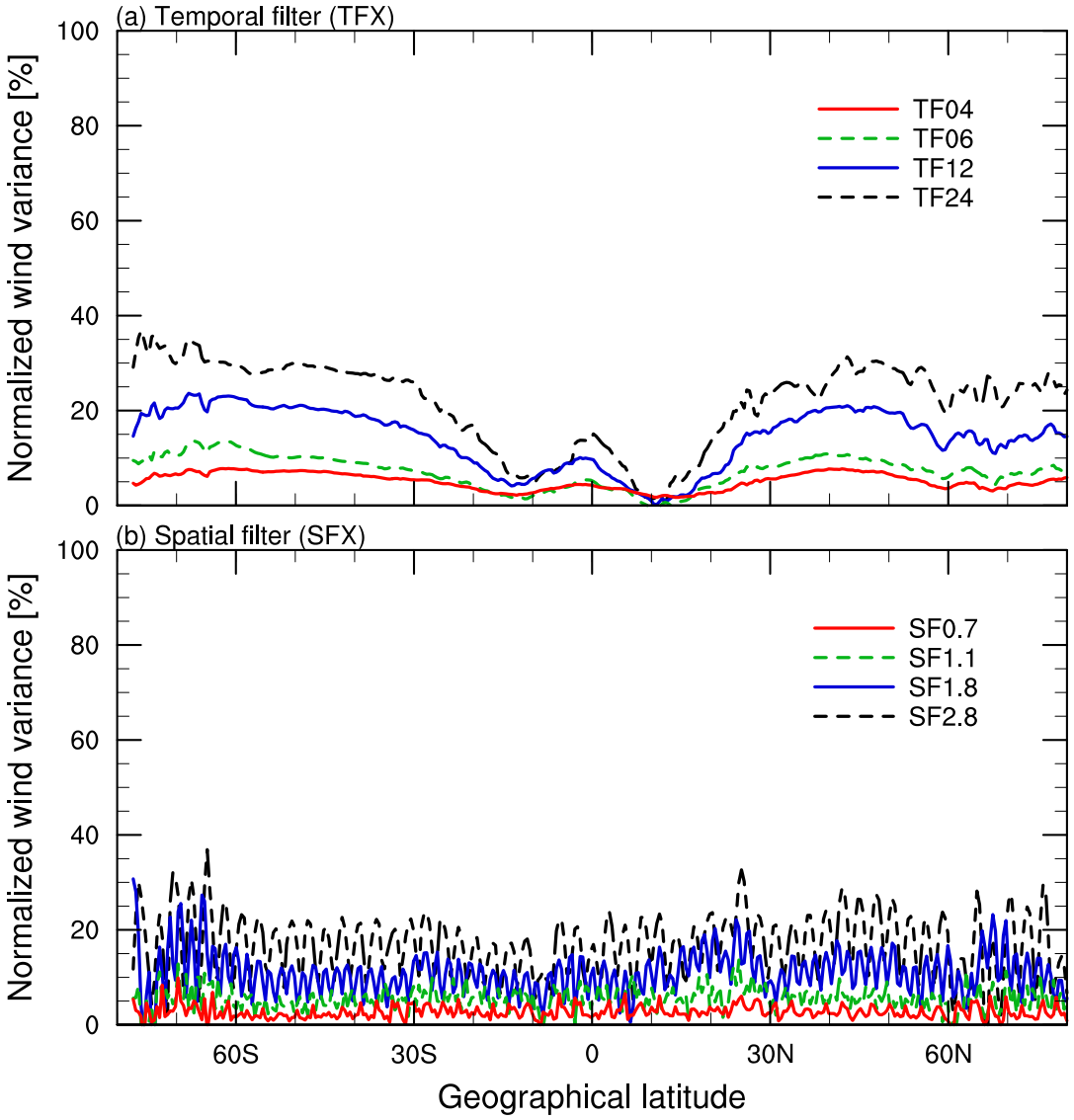

Figure 2.10: Zonal mean difference in wind stress variance between experiment CFSR and experiments (a) TFX and (b) SFX, normalized by the respective wind stress variance in experiment CFSR. On y-axis, 0% means that the variance has not changed while 100% means that the variance of the filtered data is 100% smaller than the variance of the CFSR wind stress data. Colors represent different temporal or spatial resolutions of the wind stress data used for calculation of the normalized wind stress variance.

2.5 Results

2.5.1 Near-inertial kinetic energy calculated using NCEP and CFSR wind stress data

The kinetic energy of near-inertial motions is estimated as the variance of the anticyclonically rotating velocity vector at frequencies ω, defined as: $0.7f < \omega < 1.3f$, where f denotes the local inertial frequency. We choose this frequency range to be consistent with the study of Furuichi et al. (2008). We concentrate on anticyclonically rotating variance, because it is a key feature of near-inertial motions. The calculation is done for each three-month season of 2005, and the seasonal average is presented in Figure 2.11.

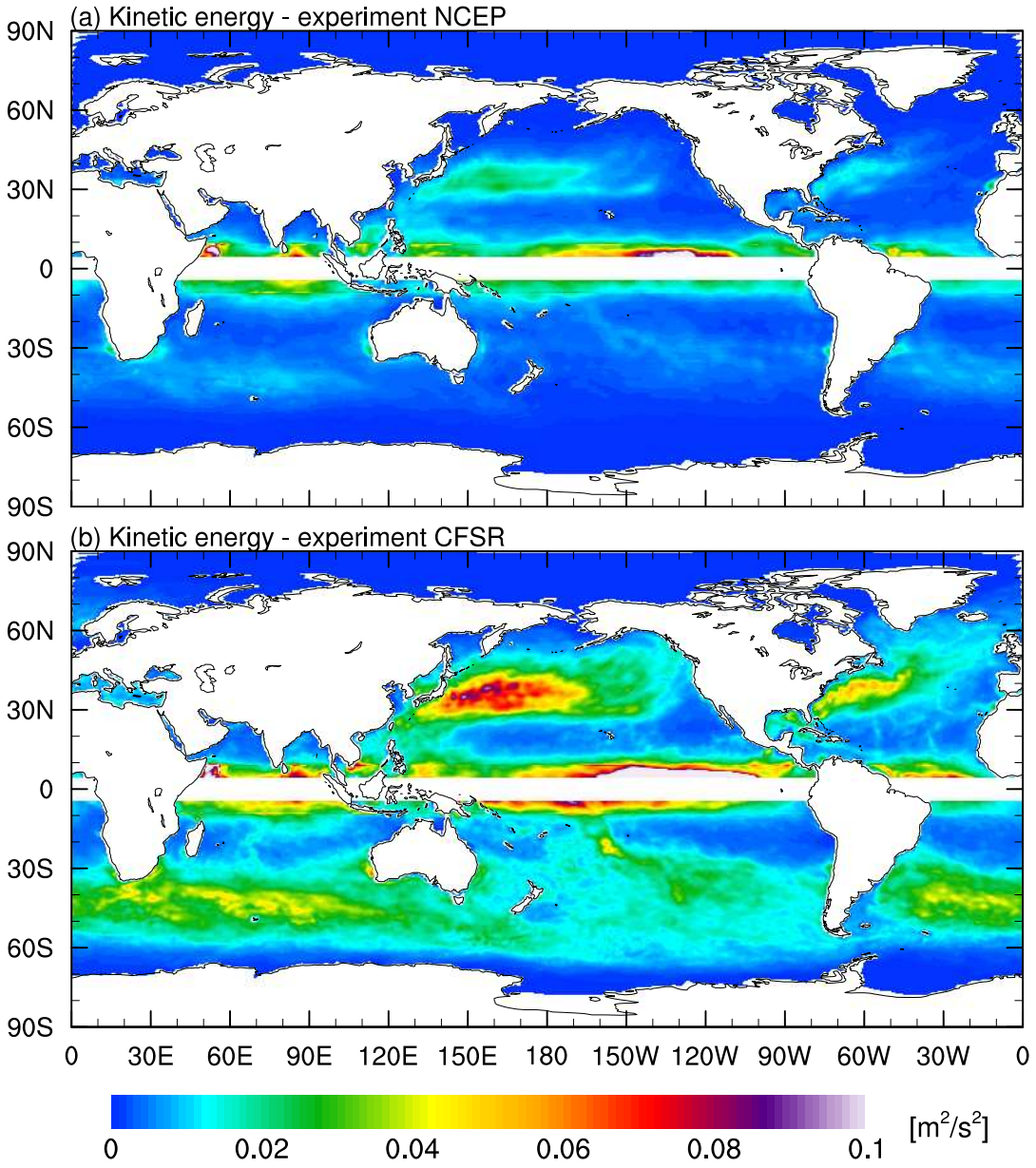

Figure 2.11: Spatial distribution of the near-inertial kinetic energy, calculated from the bandpass filtered model velocities taken from experiments (a) NCEP and (b) CFSR in [m^2/s^2].

In experiments NCEP and CFSR, the near-inertial kinetic energy (Figure 2.11) shows a pronounced maximum around 35°-50° in the mid-latitude storm tracks, consistent with Alford (2001), Watanabe and Hibiya (2002), Alford (2003a), Furuichi et al. (2008), Simmons and Alford (2012) and Jochum et al. (2013). The maximum seen around continents along 30° is a result of a strong daily cycle in the buoyancy forcing.

Forcing the ocean model with high-resolution wind stresses causes the near-inertial kinetic energy to increase (Figure 2.11b vs. 2.11a). The globally averaged value increases from 0.006 m^2/s^2 in experiment NCEP to 0.02 m^2/s^2 in experiment CFSR. The increased values are comparable to the local observational estimates at the five positions found by Plueddemann and Farrar (2006). Furthermore, the magnitude of the near-inertial kinetic energy and the global mean near-inertial velocity is comparable to that derived form observations by Chaigneau et al. (2008) and Elipot and Lumpkin (2008). Detailed comparison with the observations is given in Section 2.3.

2.5.2 The relative role of temporal and spatial resolution of the wind forcing

We analyze experiments TFX and SFX to understand the cause of the differences in near-inertial energy levels between experiments CFSR and NCEP. Relative to experiment CFSR, the reduction in near-inertial kinetic energy increases under increasingly strong filtering in time and space of the wind stress field (Figure 2.12a and 2.12b). When normalized by the near-inertial energy in experiment CFSR, wind stress forcing sampled every 4 hours (experiment TF04, red line in Figure 2.12a) generates 40% less kinetic energy at high latitudes than hourly wind stress forcing does. Using a very coarse temporal filter (experiment TF24, black line in Figure 2.12a) the near-inertial kinetic energy decreases from 0% near the equator up to about 100% poleward of 30°, meaning that near-inertial motions are entirely filtered out there. The reduction in near-inertial kinetic

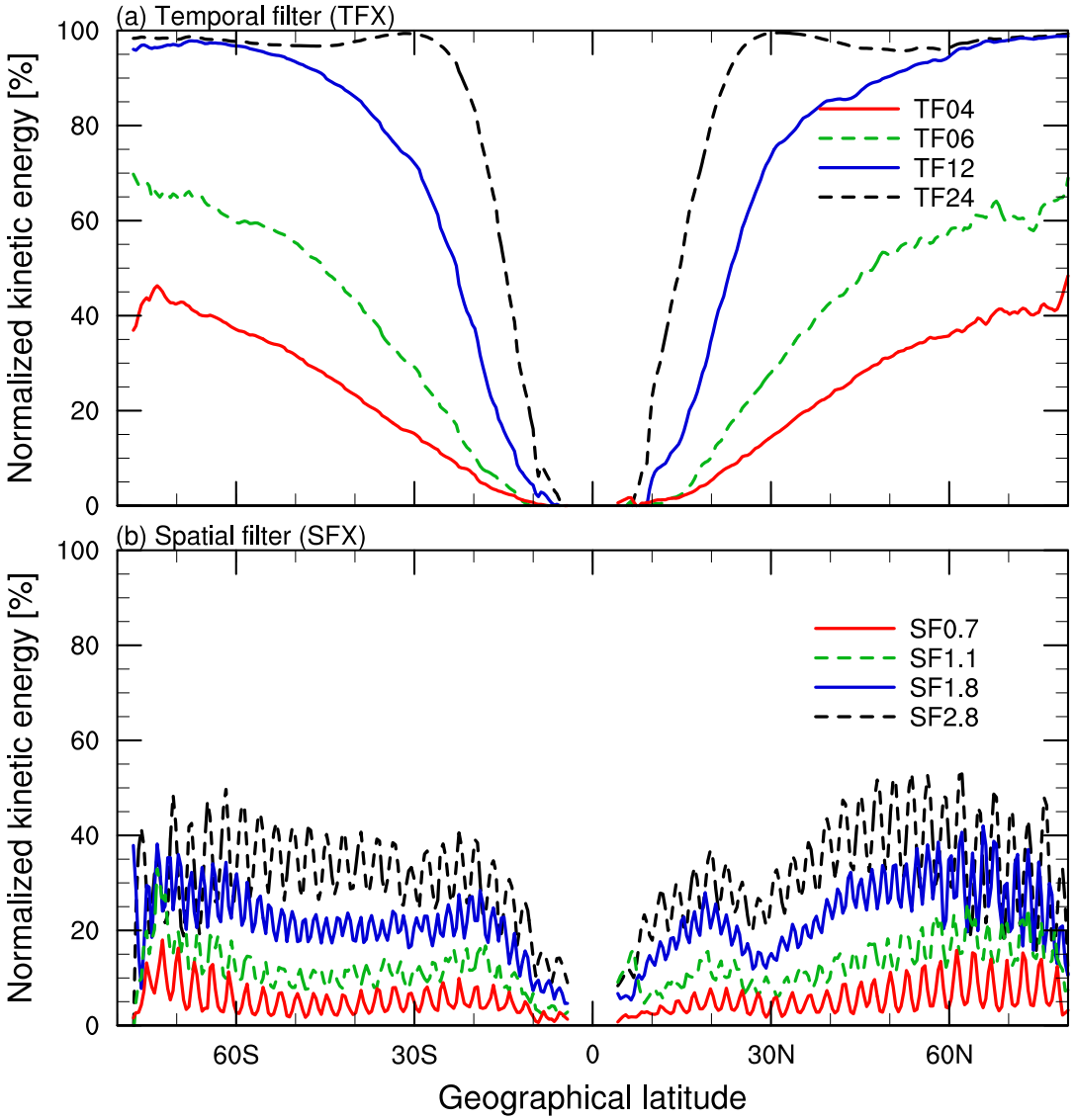

Figure 2.12: Zonal mean difference in the near-inertial kinetic energy between experiment CFSR and experiments (c) TFX and (d) SFX, normalized by the near-inertial kinetic energy from experiment CFSR. On y-axis, 0% means that the near-inertial kinetic energy has not changed while 100% means that the near-inertial kinetic energy of the filtered data is 100% smaller than the near-inertial kinetic energy of the CFSR wind stress data. Colors represent different experiments defined in Section 2.4.

energy induced by spatially filtered wind stress fields is much more moderate. Wind stress forcing generates about 40% less kinetic energy poleward of 20° when we use very coarse spatial filter in experiment SF2.8 (black line in Figure 2.12b). When normalized by the near-inertial kinetic energy in experiment CFSR, wind stress forcing sampled every 0.7° (experiment SF0.7, red line in Figure 2.12b) generates 10% less kinetic energy poleward of 20° than CFSR wind forcing at 0.35° resolution does. Our results indicate that temporal scales of the wind stress play a more important role in generating near-inertial motions than spatial scales.

The dominance of temporal scales over spatial scales results from the fact that the *time* rate of change of near-inertial motions is forced by the winds so that the spectrum of the velocity $\Gamma_{vel}(\omega)$ and that of wind stress $\Gamma_{\tau}(\omega)$ in the absence of friction satisfy:

$$\Gamma_{vel}(\omega) \sim \frac{\Gamma_{\tau}(\omega)}{(\omega + f)^2}, \tag{2.1}$$

with a resonance at the inertial frequency, $\omega = -f$. In experiment TF24, wind stress variations on time scales shorter than 24 hours are strongly suppressed. Consequently, $\Gamma_{\tau}(\omega)$ essentially vanishes for $|\omega| > 1/24$ cycles per hour and no significant inertial kinetic energy is excited poleward of 30° latitudes. In experiments TF12, TF06 and TF04, the amplitude of $\Gamma_{\tau}(\omega)$ at $|\omega| > 1/24$ cycles per hour increases noticeably poleward of 30° latitudes. The resonance response, which results in finite inertial kinetic energy in the presence of friction, becomes increasingly evident. Similar resonance behavior cannot be identified for wavenumber spectra.

2.5.3 Wind power input to near-inertial motions

Finally, we calculate the wind-power input to near-inertial motions using the cross-spectrum between velocity and wind stress integrated over the near-inertial frequency range ($0.7f < \omega < 1.3f$). More details on the used technique is given in Appendix A.2. The spatial distribution of the wind-power input to near-inertial motions (Figure 2.13) reaches maximum of about 0.02 W/m^2 in the storm track regions in experiment CFSR. Integrated globally, this value amounts to 1.1 TW (Table 2.2). The latter value is more than three times higher than in experiment NCEP (0.3 TW). The power input in the experiments TFX and SFX decreases with coarser resolution, but the decrease is more pronounced in experiments TFX.

Table 2.2: Experiment name and globally integrated wind generated power input to near-inertial motions.

	Experiment name	Wind-power input [TW]
	NCEP	0.3
	CFSR	1.1
TFX:	TF04	0.9
	TF06	0.7
	TF12	0.4
	TF24	0.2
SFX:	SF0.7	1.0
	SF1.1	1.0
	SF1.8	0.9
	SF2.8	0.7

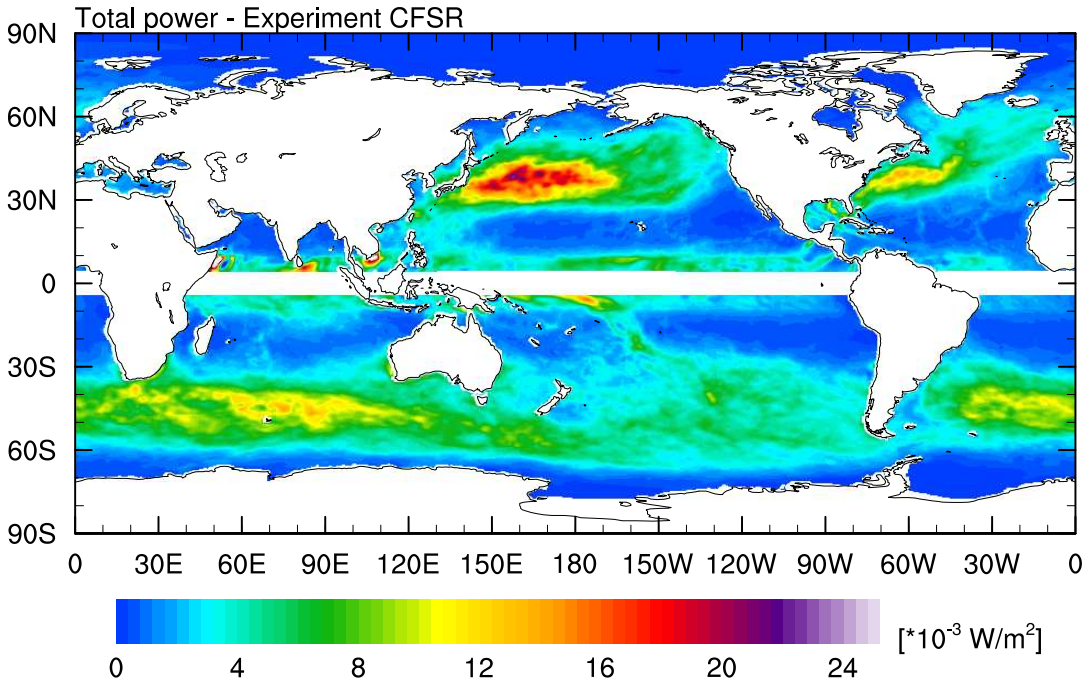

Figure 2.13: Spatial distribution of the wind-power input to near-inertial motions calculated as the cross-spectrum between current velocities and wind stress, and integrated over the near-inertial frequency range in [10^{-3} W/m^2]. A Daniell estimator is used to estimate the cross-spectrum (von Storch and Zwiers, 1999). Note that the method based on the integrated cross-spectrum (defined by a raw cross-periodogram) is identical to the method based on data filtered in respect to the same frequency range, as shown in Appendix A.2.*

2.6 Discussion and conclusions

In this chapter, we address the influence of the resolution of the wind stress forcing on the generation of near-inertial motions in the ocean by driving a global eddy-permitting OGCM with the same surface fluxes of heat and fresh water but with wind stress of different spatial and temporal resolutions. The near-inertial kinetic energy increases with increasing resolution in wind stress forcing (Figure 2.11). Its area-averaged value is three times higher (up to a factor four in the storm track regions) in experiment CFSR (forced by high-resolution wind stress: 1-hourly wind stress on T383 grid) than in experiment NCEP (forced by low-resolution wind stress: 6-hourly wind stress on T63 grid). The wind-power input to near-inertial motions is 1.1 TW in experiment CFSR, which is three times higher than in experiment NCEP (Table 2.2). Time filtering of the CSFR data affects the near-inertial kinetic energy stronger than space filtering of the same data (Figure 2.12). This suggests that high-frequency temporal variations in the wind stress field are more efficient in generating near-inertial wave energy than small-scale spatial variations in the wind stress field.

The impact of the resolution of the wind forcing has been studied using a slab ocean model by Klein et al. (2004a) who attributed their findings to better temporal resolution of the wind stress field, while Jiang et al. (2005) stressed the importance of horizontal resolution. Here, we analyze the role of spatial resolution relative to temporal resolution using an OGCM, and attribute the increased wind-power input to the better temporal resolution of the CFSR winds compared to the NCEP winds. To conclude, there is a strong sensitivity of the wind-power input to near-inertial

motions to the resolution of the wind stress forcing. This points to a possible underestimation of the energy available for the deep-ocean mixing and a need for improved estimates using more sophisticated ocean models and wind stress fields at higher spatial and temporal resolutions.

3

General properties of near-inertial waves simulated using a 1/10° ocean model

In this chapter, the general properties of near-inertial waves are addressed using a global 1/10° ocean general circulation model. Vertical profile of the zonal mean of near-inertial kinetic energy shows that the energy is drained into the deep ocean. High levels of the near-inertial kinetic energy at the ocean surface, and the strong vertical energy propagation are seen in the mid-latitudes for both January and July 2005. Equatorial regions show strong near-inertial kinetic energy throughout the water column. Spatial averages of near-inertial kinetic energy over areas with distinctly different mixed layer depth show energy enhancement at the base of the mixed layer. Energy enhancement suggests additional excitation of near-inertial waves at the base of the mixed layer.

The fraction of the total wind-induced near-inertial energy flux leaving the mixed layer is estimated using a global 1/10° ocean general circulation model with a temporally and spatially varying mixed layer. Of 0.34 TW of the mean wind-power input to surface near-inertial motions, the mean near-inertial energy flux leaving the mixed layer amounts to 0.037 TW, resulting in a mean fraction of 10.8%. The fraction tends to decrease with increasing mixed layer depth and with increasing strength of wind stress variability, indicating the strong control of the turbulent dissipation inside the mixed layer on the fraction. Our results suggest a possible overestimation of the wind-power input to near-inertial waves and point towards the need for other energy sources for deep mixing. The content of this subchapter has been submitted to Journal of Physical Oceanography as Rimac et al.

Characteristic scales of near-inertial waves are addressed on a global domain and at several oceanic levels using vertical velocity simulated by the 1/10° ocean general circulation model. Wavenumber and frequency spectra, coherence and phase are used to analyze the variability, and horizontal and vertical propagation of near-inertial waves. Spectra of two-dimensional wavenumbers do not show a clearly defined wavelength. Integrating the two-dimensional wavenumber spectra over all zonal wavenumbers we find the horizontal length scale of about

The content of this chapter has been submitted to Journal of Physical Oceanography as Rimac et al.

200 to 500 km. Frequency spectra show strong maximum near the local inertial frequency f and a lower maximum around the double inertial frequency 2f. Spectra show that the highest energy does not occur at f or at 2f but at higher frequencies. This frequency shift is less prominent when the calculation is done at 100 m than at 500 m, and for the areas further from the equator than for the areas closer to the equator. Frequency spectra do not show universal spectral shape near the local inertial frequency. The estimated horizontal coherence scale at f is about 20 to 240 km while the vertical coherence scale is about 50 m and more. Phase suggests that near-inertial waves propagate horizontally towards the equator and vertically from the deep ocean towards its surface.

3.1 Background

In this section we give a brief overview of subjects that will be in detail studied in each of the three subchapters. First, we explain a vertical structure of near-inertial kinetic energy. Second, we study fraction of the total wind-induced near-inertial energy flux that leaves the mixed layer and finally, we introduce characteristics of near-inertial waves. All three points are studied using 2-month of 1-hourly output of a simulation performed with a high-resolution 1/10° ocean general circulation model described in Section 3.2.

Strong near-inertial waves are present in all realistic ocean general circulation models based on primitive equations and forced by high-frequency wind stress forcing. These waves possess the energy in the frequency band close to the Coriolis frequency f. Near-inertial waves are generated by the atmospheric storms that are the strongest in winter due to stronger temperature gradients and stronger pressure differences. Near-inertial waves excited by the passing storms can propagate horizontally as well as vertically (e.g., Fu, 1981, Simmons and Alford, 2012). Alford et al. (2012) and Silverthorne and Toole (2009) used observational data from the North Pacific and the North Atlantic respectively, to examine the seasonal variability of near-inertial kinetic energy as well as the vertical structure of the near-inertial kinetic energy. Zhai et al. (2005, 2007) used a numerical ocean model to asses the vertical propagation of storm-induced near-inertial energy. In spite of these previous works, many aspects of near-inertial waves have still not been systematically studied. Here we will focus on three of these aspects.

In the subchapter 3.3 we focus on the vertical profile of the near-inertial kinetic energy, its propagation into the deep ocean and its vertical structure, using a simulation obtained from a 1/10° ocean model. Such vertical profile suggests how deep near-inertial waves generated at the sea surface can penetrate into the ocean interior and whether there are processes inside ocean which can modify the strength of near-inertial waves.

In the second subchapter 3.4 we study the energy generated by winds at the ocean surface and the fraction of the inputted power that leaves the mixed layer. One way for surface winds to provide power for the deep mixing is via near-inertial waves that are excited at the ocean surface. Near-inertial waves that escape the turbulent mixed layer can propagate more freely into the stratified deep ocean. When breaking in the oceanic interior, they can contribute to deep-ocean mixing. The vertical energy flux leaving the mixed layer is of critical importance, because, if the waves completely dissipate in the upper ocean, no energy is left for mixing in the deep ocean. Up to our knowledge, the near-inertial energy flux has been studied using global and regional ocean models but with leveled upper ocean of constant depth (Furuichi et al., 2008, Zhai et al., 2009) but the near-inertial energy flux out of the mixed layer is dynamically more relevant and it has not

been assessed yet.

Characteristic scales of near-inertial waves, the focus of subchapter 3.5, have so far mostly been studied based on observations at limited sites (e.g., Fu, 1981, Alford, 2010, Alford et al., 2012) and ocean models configured for a limited area (e.g., Danioux et al., 2008, Danioux and Klein, 2008, Danioux et al., 2011). It has been shown that strong variability of the velocity field is present throughout the water column with two distinct maxima, one in the lower thermocline between 100 m and 500 m and one in the deep ocean between 1700 m (Danioux et al., 2008) and 2500 m (Danioux et al., 2011). Frequency spectra show changing shape in the internal wave field. The shape depends on the area and depth for which the estimate is made; therefore, so far there was no reported universal shape of the frequency spectrum. In the frequency spectrum (Danioux et al., 2008, Danioux and Klein, 2008) a distinct maximum could be seen at the local inertial inertial frequency f, and at double inertial frequency $2f$. This maximum is mostly not centered at f but slightly above f (Fu, 1981). In the study by Fu (1981), horizontal coherence has a scale of about 60 km, while vertical coherence has the scale of about 200 m in the upper thermocline, and about 1000 m in the deep ocean. Vertical phase difference suggests downward energy propagation in the lower thermocline and the existence of standing waves in the deep ocean (Fu, 1981). The importance of this subchapter is to clarify on a global domain characteristic length and temporal scales of near-inertial waves as well as their propagation in horizontal and vertical direction.

Evaluating the structure of near-inertial waves, their horizontal and vertical propagation, their energy propagation and the fraction of the energy that is available for deep ocean mixing requires three-dimensional fields of velocity, temperature and salinity. These fields are not directly available from observations. Therefore, this study makes use of spatial variables (e.g., vertical and horizontal velocity, and pressure) simulated with a global Ocean General Circulation Model (OGCM), i.e., the Max Planck Institute Ocean Model (MPIOM) at a 1/10° horizontal resolution. A model at this resolution is believed to provide a more complete representation of the long waves described by the primitive equations than observational estimates do. We use the global OGCM because we are interested in characteristics of near-inertial waves at a global scale and not just in a specific region (e.g., North Atlantic region as in Zhai et al. (2007)) or at one mooring site.

3.2 Numerical model set-up

The model used in this study, MPIOM, is the same as the one used in the previous chapter, but at a higher horizontal and vertical resolution of 1/10° and 80 levels, respectively. The model is formulated on a tripolar grid with a grid size of about 10 km near the equator which decreases to 2.4 km towards the South Pole. The vertical level thickness increases from 10 m in the surface layers to about 280 m at the bottom. The model simulates mesoscale eddy characteristics in agreement with observations (von Storch et al., 2012). MPIOM uses a Richardson number-dependent mixing scheme (Pacanowski and Philander, 1981), which is augmented by additional parametrization for wind induced stirring. The near surface wind mixing is a function of local 10 m wind speed, it decays exponentially with depth and depends on the local static stability. The surface wind mixing is also reduced in proportion to the fractional sea-ice cover.

Mixed layer depth is an important quantity for this chapter. It is diagnosed from temperature and salinity fields and defined as the depth at which the density changes from the surface value by $0.125\,\mathrm{kg/m^3}$ has occurred. The depth of the simulated global mean mixed layer is about 47 m in

January, and about 120 m in July. The simulated mean mixed layer depth (Figure 3.1, red line) is in broad agreement with that derived from Polar science center Hydrographic Climatology (Figure 3.1, black line; Steele et al., 2001). Some difference between observations (PHC climatology) and simulated mean mixed layer depth appear around 50° S in both January and July and around 50°-60° N in January because of strong temperature and salinity biases there (Jungclaus et al., 2013).

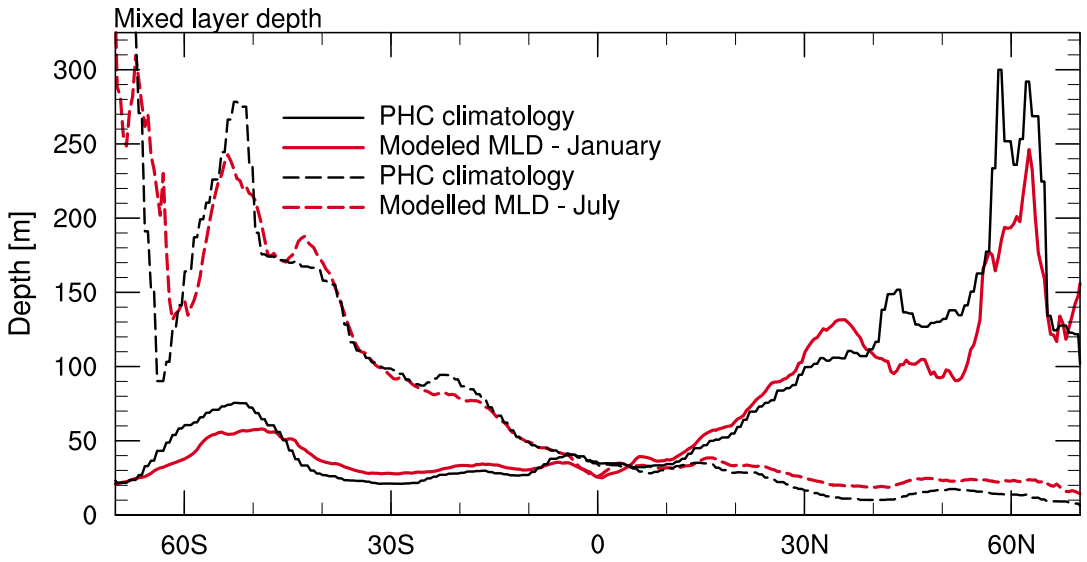

Figure 3.1: Zonal mean mixed layer depth calculated for January (solid line) and July (dashed line) separately. Mixed layer depth is calculated using monthly mean values of temperature and salinity fields of years 1948 to 2000 from PHC climatological data (black line, Steele et al., 2001) and using model results of monthly mean temperature and salinity of the year 2005 (red line). It is calculated using sigma-t density criterion (Levitus, 1982). Mixed layer depth is defined as the depth at which a change from the surface density of 0.125 kg/m^3 has occurred.

The model is spun-up for 25 years with climatological forcing, and run for another 60 years using surface fluxes of heat and momentum derived from the 6-hourly National Centers for Environmental Prediction (NCEP) reanalysis at approximately 1.875° resolution (Kalnay et al., 1996). The fresh water flux from evaporation and precipitation is supplemented by daily river discharges at approximately 1.125° resolution. For the analysis considered in this chapter, we use the three-dimensional hourly model output for January and July 2005.

3.3 Vertical structure of near-inertial kinetic energy

3.3.1 Introduction

Near-inertial waves are a commonplace feature of the ocean. The kinetic energy spectrum of horizontal and vertical velocity obtained from observations as well as model studies tends to display an energetic maximum associated with near-inertial waves (e.g., Plueddemann and Farrar, 2006, Ferrari and Wunsch, 2009). The predominant generation mechanism for these waves are winter storms, e.g., cold fronts and small low pressure systems acting at the ocean surface (D'Asaro, 1985). Accordingly, there is a maximum in winter (January-March in the Northern Hemisphere and July-September in the Southern Hemisphere) in the wind energy input because of prevalence of the storms in that season (Alford, 2001, Watanabe and Hibiya, 2002, Alford, 2003a, Furuichi et al., 2008). Once generated, near-inertial waves can propagate horizontally from their generation region towards the equator, and vertically from the ocean surface into deeper layers of the ocean (Alford, 2003b). Vertical profiles of the ocean velocity show the presence of energetic depth- and time-dependent current fluctuations (Leaman and Sanford, 1975, Silverthorne and Toole, 2009). However, the exact global vertical near-inertial kinetic energy distribution remains unclear.

Change of the near-inertial kinetic energy in the vertical direction has so far been studied using observations and OGCMs. Based on a series of moorings fitted with McLane Moored Profiles (MMP) located at approximately 39° N in the western Atlantic, Silverthorne and Toole (2009) investigated seasonality of near-inertial internal waves and examined a localized kinetic energy budget for these motions, focusing specifically on the wind energy input. They showed that near-inertial kinetic energy exibits a strong seasonal cycle with a winter-time maximum which was dominated by downward energy propagation. Observations of the mixed layer depth demonstrated that the maximum of the near-inertial kinetic energy is constantly extended well below the mixed layer depth (around 100-200 m) and it shows enhancement in the upper portion of the water column (around 400 m). Silverthorne and Toole (2009) showed that in summer, the near-inertial kinetic energy profile is nearly uniform with depth. In a similar analysis, Alford et al. (2012) used the data from two Acoustic Doppler Current Profilers (ADCP) deployed at 50 textdegree N in the eastern Pacific. They found that substantial fraction of the energy input into the mixed layer passes 800 m suggesting that this energy reaches the deep ocean. However, they reported important differences between two winters in their study, from which they concluded that the lateral structure of the storms plays an important role for the vertical energy distribution.

Using an idealized ocean channel model at 1/3° horizontal resolution for the Southern Ocean, Zhai et al. (2005) studied the interaction between near-inertial waves generated by a storm in a mesoscale eddy field. They showed that the leakage of near-inertial kinetic energy out of the surface layers is strongly enhanced in the presence of mesoscale eddies. In a latter study, Zhai et al. (2007) used a primitive equation 1/12° ocean model of the North Atlantic forced with daily varying wind stress from the forecasts of the operational weather forecast model from the European Center for Medium Weather Forecast (ECMWF). They found that the near-inertial kinetic energy is strongly influenced by the mesoscale eddy field and appears to be locally drained to the deep ocean, largely by a chimney effect associated with anticyclonic eddies.

The previous studies based on numerical models and observations thus indicate that there is a substantial near-inertial kinetic energy in the ocean. At the same time, observational studies showed a seasonal variability of the near-inertial kinetic energy throughout the water column.

However, the vertical distribution of global mean near-inertial kinetic energy over one month period and a possible connection between the vertical distribution of the near-inertial kinetic energy and a realistic spatial structure of the mixed layer depth have not been assessed yet. Therefore, we use MPIOM, which is a global ocean general circulation model, at 1/10° resolution and with 80 vertical levels. We address the following questions: How does the vertical structure of the zonally averaged near-inertial kinetic energy look like? Is there a connection between the mixed layer depth and the vertical structure of near-inertial kinetic energy in the ocean?

3.3.2 Results

First, we look at the vertical structure of near-inertial kinetic energy. The kinetic energy of near-inertial waves is calculated as the variance of the anticyclonically rotating velocity vector integrated over frequencies ω with: $0.7f < \omega < 1.3f$, where f denotes the local inertial frequency. Here, the calculation is done for the first 1100 m for January and July 2005 separately. The result is presented in Figure 3.2 as a vertical distribution of the zonal mean near-inertial kinetic energy.

Figure 3.2 shows that the near-inertial kinetic energy has, apart from the maximum close to the equator, a pronounced maximum in the mid-latitude storm track regions (around 20°-50°). This maximum is stronger in the winter season of a given month, i.e., in the Northern Hemisphere in January and in the Southern Hemisphere in July. The maximum around the equator is the strongest, probably because of the interaction of the locally generated waves and the near-inertial waves propagating from higher latitudes. The globally averaged value of near-inertial kinetic energy for both months reaches $0.006\,m^2/s^2$ at the ocean surface. The global average reduces similarly for both months down up to 100 m. Below 100 m the reduction in the global average of near-inertial kinetic energy is stronger in July than in January. This suggests that stronger wind variability from January leads to more of the near-inertial kinetic energy propagating to deeper layers.

From the vertical distribution of the zonal mean near-inertial kinetic energy we could see that in general energy decreases with depth, but at the same time there are high levels of near-inertial kinetic energy in the first 50-200 m in the ocean. To further address the question of how the near-inertial kinetic energy changes with depth, we look at the specific regions in the ocean defined by distinctly different mixed layer depth. Figure 3.3a and 3.4a illustrate the spatial structure of the mixed layer depth obtained for January and July separately. In January, mixed layer depth shows deepening down to about 200 m in the Northern Hemisphere storm track regions, e.g., around 30°-50° N compared to the mean value of 47 m. Also, deep mixed layer depth in January is seen in the region of the North Atlantic sub-polar gyre (around Greenland). Deepening of the mixed layer in storm track regions indicates that winds have an influence on the mixed layer depth. In July, deep mixed layer depth is seen in the Southern Hemisphere (up to 900 m, around 30°-60° S). These spatial structures are consistent with the observational estimates (Figure 3.1) and also with the study by Jungclaus et al. (2013) who used the same numerical model (MPIOM) but at a lower horizontal resolution.

Figures 3.3b and 3.3c (and Figures 3.4b and 3.4c) illustrate the vertical profiles of near-inertial kinetic energy averaged over the areas highlighted in Figure 3.3a for January (and in Figure 3.4a for July). We use areas with distinctly different mixed layer depth. For example, in Figure 3.3a, in area 1 the mean mixed layer depth is 120 m and in its neighboring area 2 the mean mixed layer

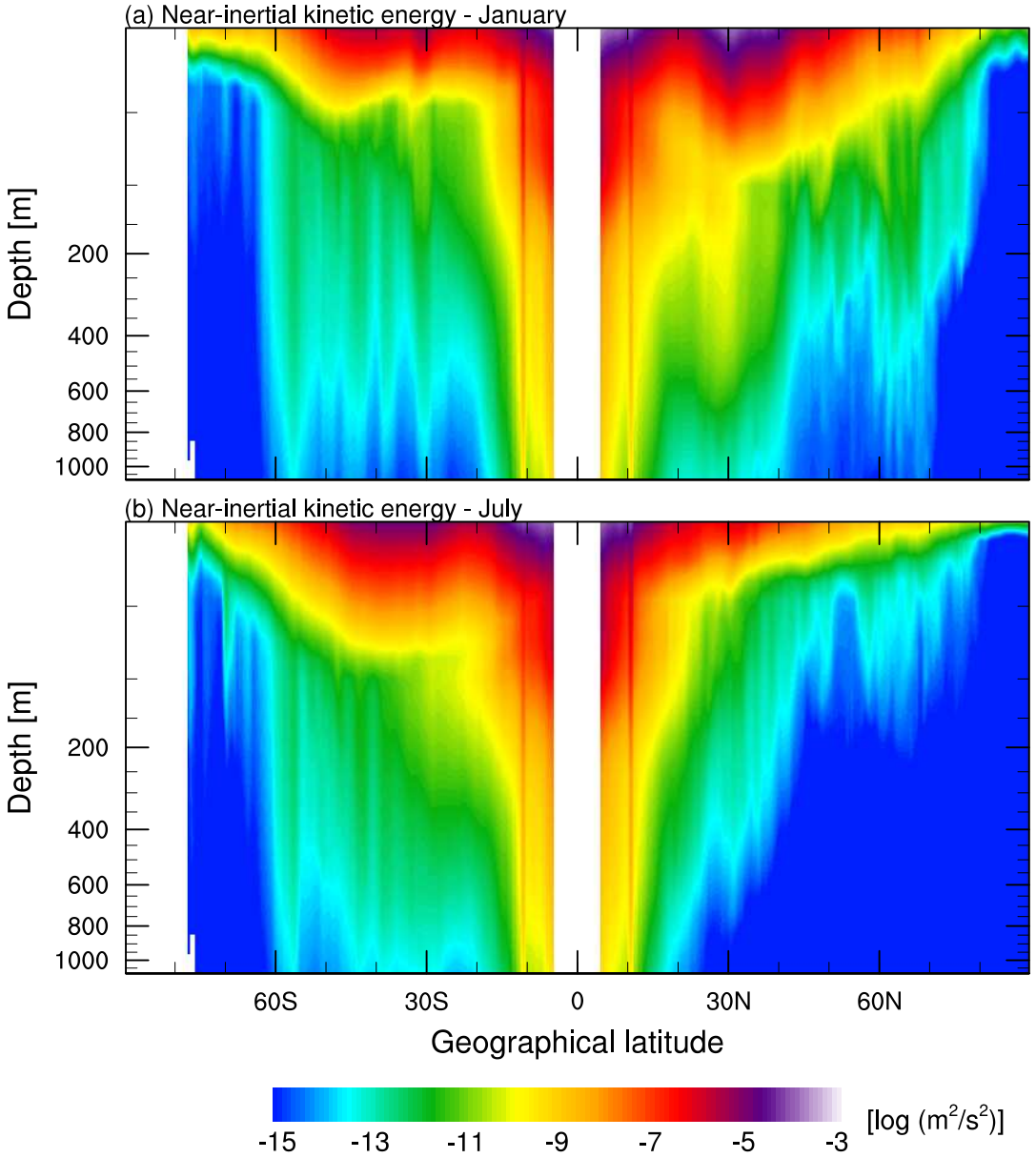

Figure 3.2: Vertical distribution of the zonal mean near-inertial kinetic energy for the first 1100 m calculated from the bandpass-filtered model velocities for (a) January and (b) July. The result is presented in a logarithmic scale [log (m^2/s^2)].

depth is 85 m. We chose these areas in order to have the direct insight in whether the vertical profile of near-inertial kinetic energy changes with changing mixed layer depth. In case there is a secondary maximum of near-inertial kinetic energy in the oceanic interior, this maximum is marked by a black dot. Horizontal lines represent the mean depth of the mixed layer, i.e., the base of the mixed layer, for each area separately. The respective mean depth for each area is given in Table 3.1. It can be seen that there is a strong variability in the mean mixed layer depth between the areas, especially when the calculation is done for the winter season of each month. On the other hand, the mean mixed layer depth is almost constant (around 20-30 m) in the summer season. The vertical profiles reveal that the near-inertial kinetic energy reduces from the surface towards the deep ocean. In all profiles the energy reduces up to 1000 times throughout the depth of 1000 m. The results obtained from the Northern Hemisphere show that in July the near-inertial

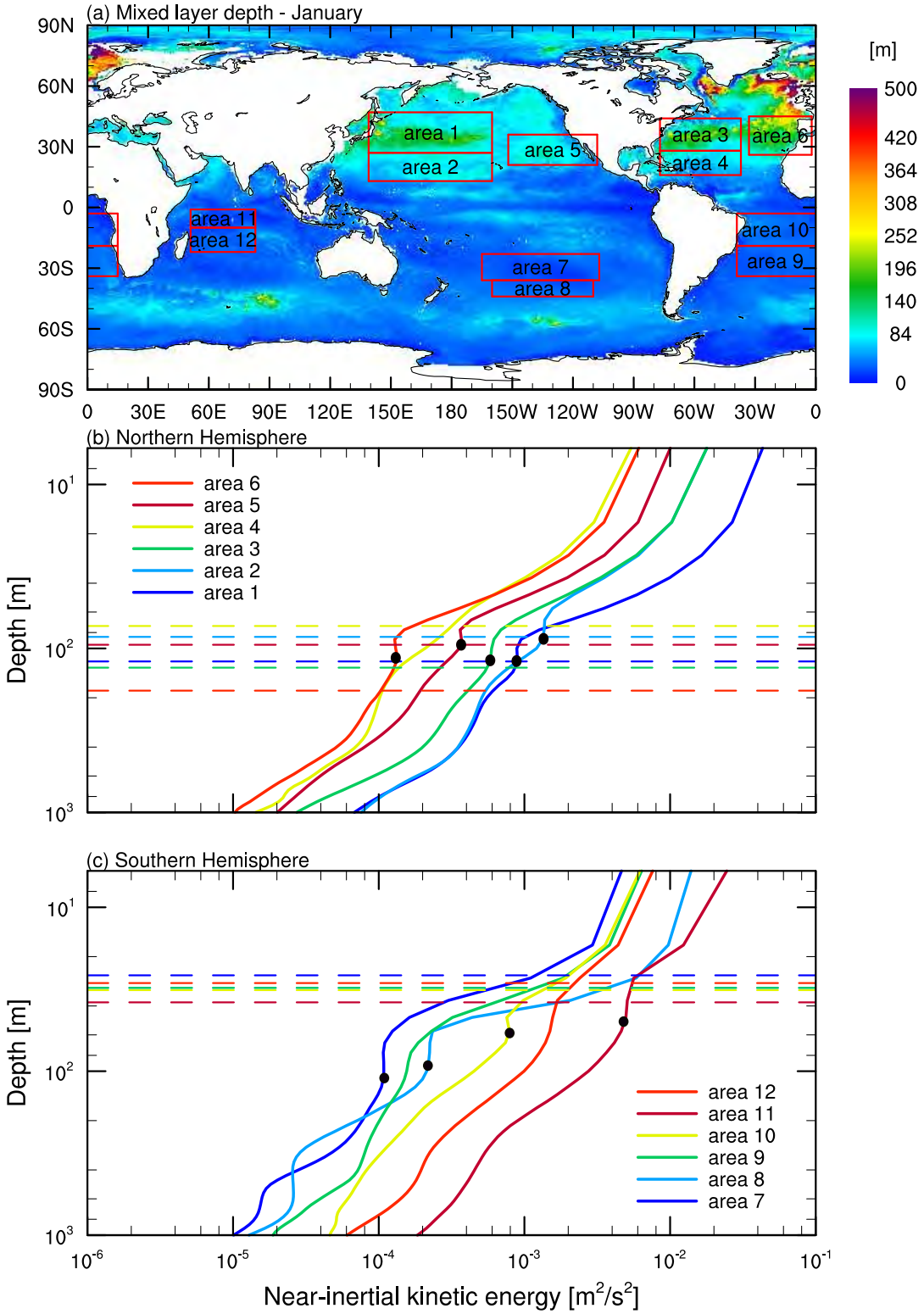

Figure 3.3: (a) Spatial distribution of the mixed layer depth calculated for January 2005. Vertical profiles of near-inertial kinetic energy averaged over the areas highlighted in (a). Energy is calculated from the bandpass-filtered model velocities for the areas in (b) the Northern Hemisphere and in (c) the Southern Hemisphere. Horizontal lines represent the mean mixed layer depth for each area. Black dots represent the points where the near-inertial kinetic energy is increased compared to its neighboring points (secondary maximum).

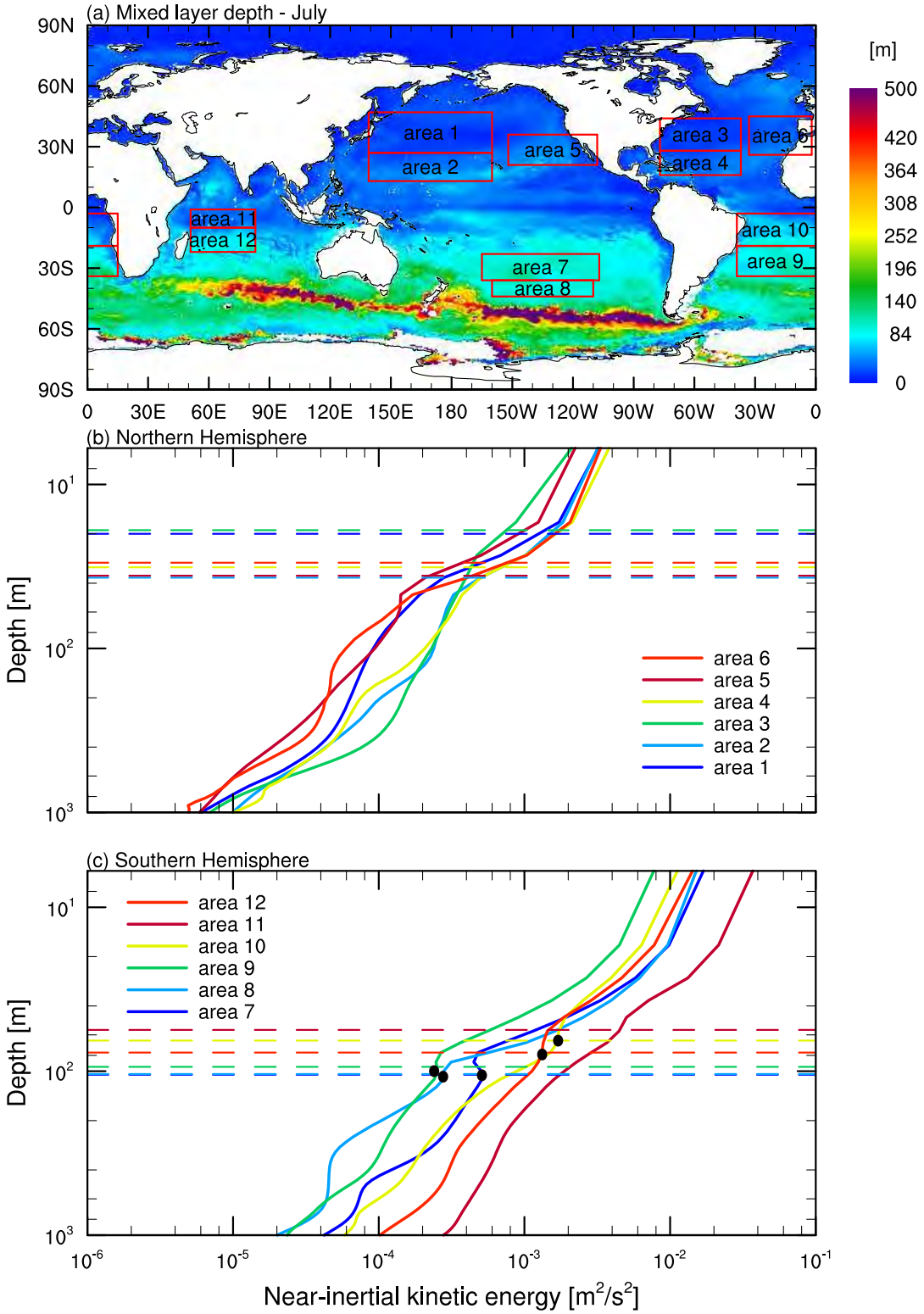

Figure 3.4: (a) Spatial distribution of the mixed layer depth calculated for July 2005. Vertical profiles of near-inertial kinetic energy averaged over the areas highlighted in (a). Energy is calculated from the bandpass-filtered model velocities for the areas in (b) the Northern Hemisphere and in (c) the Southern Hemisphere. Horizontal lines represent the mean of mixed layer depth for each area. Black dots represent the points where the near-inertial kinetic energy is increased compared to its neighboring points (secondary maximum).

kinetic energy decrease with depth is comparable for different areas and the vertical profiles are about the same for all areas. This is not seen in the Southern Hemisphere in January where the vertical profiles are disparate for all areas. For some areas in the Northern Hemisphere in January (Figure 3.3b) and in the Southern Hemisphere in July (Figure 3.4c), a small secondary maximum is seen in the ocean interior, at about the base of the mixed layer. This secondary maximum is also seen in the Southern Hemisphere in January but well below the base of the mixed layer. At the same time, the secondary maximum or its correspondence to the mixed layer depth is not seen in the Northern Hemisphere in July. Figure 3.3b and 3.4c show that the secondary maximum is stronger when the mean near-inertial kinetic energy is calculated for the areas closer to the Equator (e.g., the maximum is the strongest for area 2, centered around 20° N in January and for area 10 and area 12, centered around 5°-10° S in January and July).

Table 3.1: Mean values of the mixed layer depth for the areas depicted in Figure 3.3 for January and Figure 3.4 for July. The mean values for the areas are given in [m]

	Area name	January (winter)	July (summer)
Northern Hemisphere:	area 1	120	20
	area 2	85	37
	area 3	131	19
	area 4	73	32
	area 5	91	36
	area 6	151	30
		January (summer)	July (winter)
Southern Hemisphere:	area 7	26	105
	area 8	31	104
	area 9	31	94
	area 10	32	65
	area 11	38	56
	area 12	29	77

In an idealized study, Zhai et al. (2005) emphasized the important role of anticyclonic eddies which drain the near-inertial energy to the deep ocean. Similarly, Zhai et al. (2007) showed the association between high levels of near-inertial energy and anticyclonic relative vorticity. Following their example, in Figure 3.5 we show a probability distribution function of number of grid points sorted according to near-inertial kinetic energy and relative vorticity. We use the model grid points from the storm track region of North Pacific (around 30°-50° N) in January and we use the model grid points from the storm track region of South Pacific (around 20°-40° S) in July. Both months offer a very clear example that the maximum of the relative likelihood of the near-inertial kinetic energy is confined within an anticyclonic mesoscale eddy field. In July the dependence of the near-inertial kinetic energy on anticyclonic vorticity is not so obvious because of the weaker near-inertial kinetic energy.

To evaluate our results obtained in January against the previous study by Zhai et al. (2007) we look at a spatial structure and a vertical cross-section of near-inertial kinetic energy for the North Atlantic region (Figure 3.6). The spatial structure of the near-inertial kinetic energy at the surface and around 500 m are similar to Zhai et al. (2007), with the maximum over Grand Banks of Newfoundland. At 500 m small structures that reflect the mesoscale eddy field can be

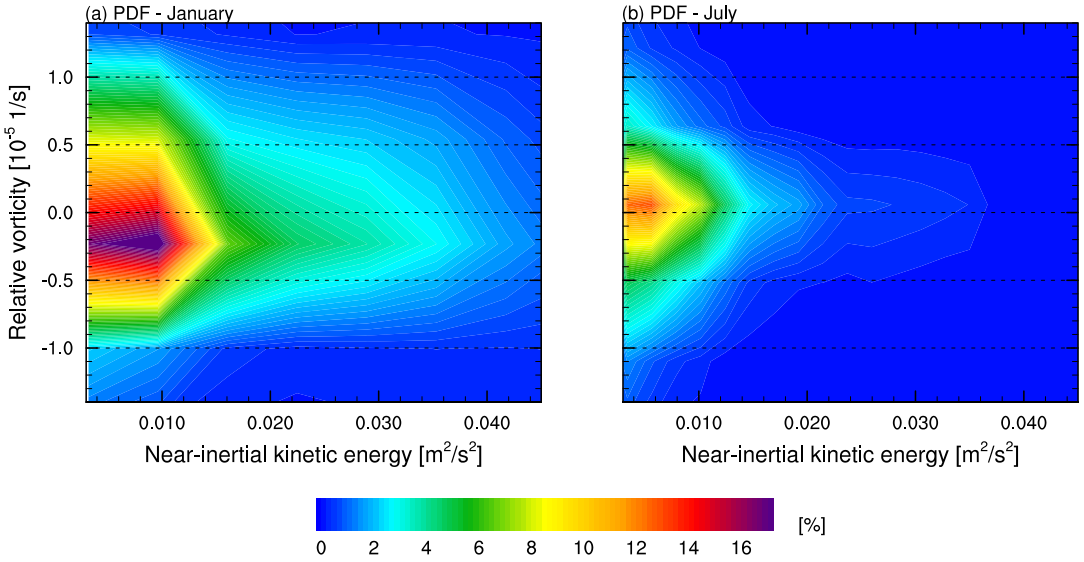

Figure 3.5: Probability distribution function of number of grid points as a function of relative vorticity and near-inertial kinetic energy calculated from the bandpass-filtered model velocities at 6 m for (a) January using model grid points from the North Pacific, and for (b) July using model grid points from the South Pacific. Note that anticyclonic relative vorticity is negative when the calculation is done for the Northern Hemisphere and positive when the calculation is done for the Southern Hemisphere. Contours given in % represent relative amount of points in each segment of the graph.

found. Also, at 500 m (Figure 3.6b) large near-inertial kinetic energy levels are confined in the region of the western boundary current. The maximum values of 0.088 m^2/s^2 at the surface and 0.0017 m^2/s^2 at 500 m are somewhat smaller than the ones obtained by Zhai et al. (2007) (up to 2 m^2/s^2 at the surface) probably because of a different near-inertial frequency band used in their study (highpass filter with cutoff frequency at 1.3 cpd, against bandpass filter used here) and a different month of consideration (March, against January used here). Vertical cross-sections of the near-inertial kinetic energy calculated along 59° W in Figure 3.6c and 45° W in Figure 3.6d reveal a similar picture, with relatively high levels of near-inertial kinetic energy in "chimneys" which are confined in the neighborhood of the Gulf stream. This energy propagates up to 1000 m depth with strength of about 0.001 m^2/s^2.

3.3.3 Discussion and conclusions

In this subchapter, we study the vertical structure of near-inertial kinetic energy in the ocean simulated with an OGCM at high horizontal and vertical resolution, i.e., 1/10° horizontal resolution and 80 vertical levels, respectively. The vertical structure of near-inertial kinetic energy shows a stronger surface intensification in the winter hemisphere than in the summer hemisphere (Figure 3.2). This indicates that the near-inertial kinetic energy has a seasonal cycle with a maximum in winter that is mostly pronounced in the upper 200 m. The surface intensification in the mid-latitudes endorses the hypothesis that near-inertial waves in those regions are primarily surface forced by the passage of winter storms. In the equatorial regions the intensification of the near-inertial kinetic energy is seen throughout the water column, indicating that next to locally generated waves there is an additional source of energy, probably arising from near-inertial

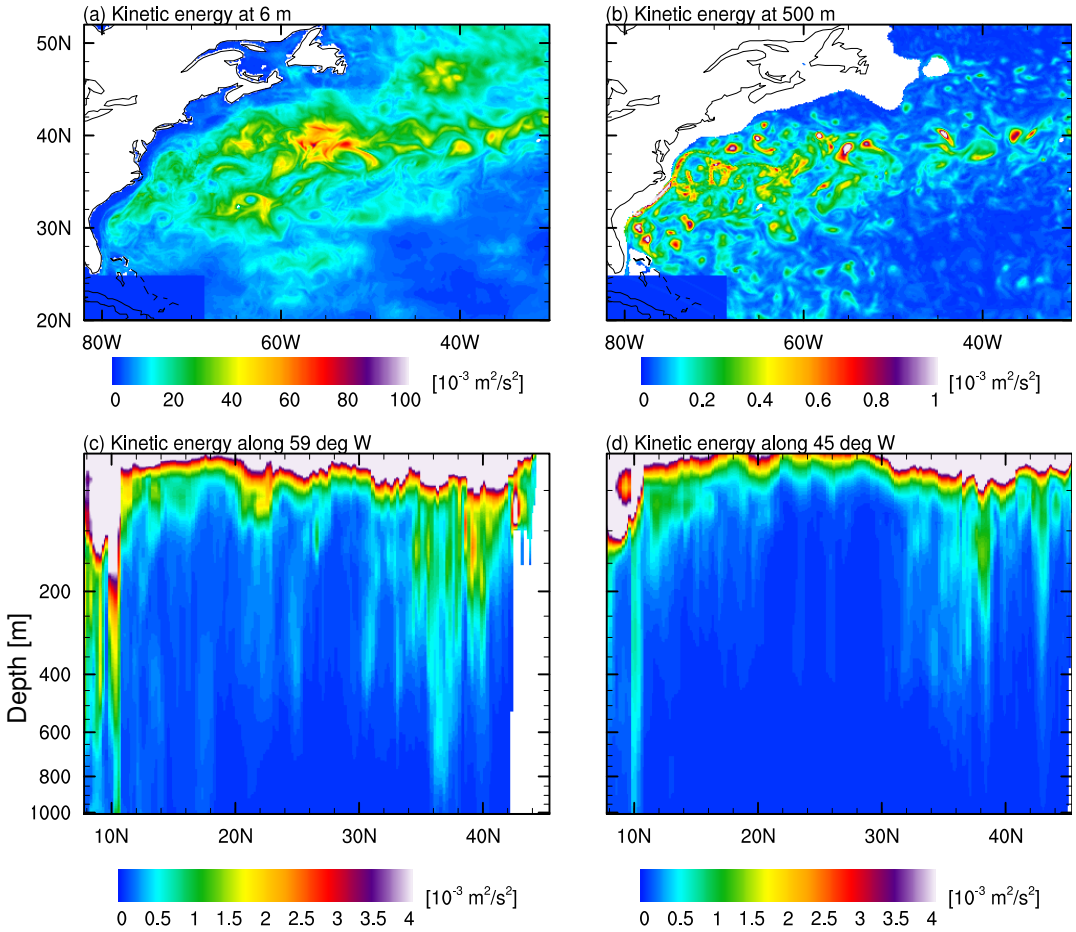

Figure 3.6: Spatial distribution of near-inertial kinetic energy calculated from bandpass filtered model velocities at (a) 6 m and (b) 500 m depth. Vertical cross-section of the near-inertial kinetic energy along (c) 59° W and (d) 45° W. Calculations are done for January 2005.

waves propagating from higher latitudes or other mechanisms such as tropical instability waves. The area mean of near-inertial kinetic energy shows that the energy in general decreases with depth. In the winter hemisphere there is a small maximum seen at the base of the mixed layer (Figure 3.3b and 3.4c). This maximum is also seen in the summer hemisphere in January but well below the mean mixed layer. Also, it is noted that the secondary maximum is higher when the area mean near-inertial kinetic energy is calculated for the areas closer to the equator.

Our results show the enhancement of near-inertial kinetic energy at the mixed layer depth which leads to the conclusion that apart from the energy generation at the ocean surface, some of the near-inertial energy is generated near the base of the mixed layer. This generation can be related to Ekman pumping. Wind stress acting at the surface of the ocean will drive a relatively shallow upper ocean flow and transport water to the right in the Northern Hemisphere (or to the left in the Southern Hemisphere). Horizontal variations in the wind stress thus result in changes in convergence and divergence of the surface Ekman transport. This forces vertical water motion within the mixed layer that is convergent in anticyclonic flow and divergent in cyclonic flow. The convergent flow drives downward vertical motion (Ekman pumping) while the divergent flow drives upward vertical motion (Ekman suction). Variations in Ekman pumping can excite near-inertial waves and induce the energy enhancement at the base of the mixed layer seen in the winter hemisphere (Figure 3.3b and 3.4c).

3.4 Near-inertial energy flux leaving ocean's mixed layer

This subchapter is written in a paper form and it has been submitted to Journal of Physical Oceanography.

3.4.1 Introduction

The power needed for mixing to sustain the global general circulation in the deep ocean is believed to be mainly supplied by winds and tides (e.g., Munk and Wunsch, 1998) but other processes like dissipation of mesoscale eddies can also contribute (Tandon and Garrett, 1994). One way for surface winds to provide power for the deep mixing is via near-inertial waves that are excited at the ocean surface. Near-inertial waves that escape the turbulent mixed layer can propagate freely into the stratified deep ocean. When breaking in the oceanic interior, they can contribute to deep mixing. In this respect, the fraction of the total wind-induced near-inertial energy flux leaving the mixed layer (hereafter referred to as FRACTION) is a quantity important for understanding the global general circulation and the energetics of the ocean.

The wind-power input to near-inertial motions has been studied using both slab ocean models and Ocean General Circulation Models (OGCM) but with different wind stress products. The spread of the estimates ranges from 0.3-0.7 TW using slab ocean models (e.g., Alford, 2001, Watanabe and Hibiya, 2002) to 0.3-1.1 TW using OGCMs (e.g., Furuichi et al., 2008, Simmons and Alford, 2012, Jochum et al., 2013, Rimac et al., 2013). Here, we repeat the analysis concerning wind-power input to near-inertial motions from the study by (Rimac et al., 2013, see Chapter 2) using a global OGCM at much higher horizontal and vertical resolution (1/10°, 80 levels) and with wind stress data from 6-hourly National Centers for Environmental Prediction/National Centers for Atmospheric Research (NCEP/NCAR) reanalysis. The aim is to trace the fate of this energy input escaping the mixed layer.

The question of how much of the wind-induced power is dissipated in the surface layer and hence is lost for the deep ocean has been studied by several authors (e.g., Large and Crawford, 1995). Furuichi et al. (2008) used a global model setup at 1/7° horizontal resolution, with a vertical mixing scheme by Mellor and Blumberg (2004). They estimated that in total 75-85% of the global annual mean wind-power input to surface near-inertial motions is dissipated in the surface 150 m depending on the region under consideration. Zhai et al. (2005, 2009) pointed out that in the presence of mesoscale eddies, vertical propagation of near-inertial waves can be amplified. Zhai et al. (2009) used a regional ocean model of the North Atlantic at 1/12° horizontal resolution and with the vertical mixing scheme by Gaspar et al. (1990). They found that nearly 70% of the wind-induced near-inertial energy at the sea surface is dissipated within the top 230 m by vertical friction, 8% is lost due to biharmonic dissipation and 10% is lost by lateral fluxes. In their analysis, they showed that only 10% of the vertical near-inertial energy flux propagates into the deep ocean below 230 m.

The previous studies thus indicate that a large portion of wind-induced power is dissipated in the surface layer of the ocean. However, the energy flux out of the mixed layer, rather than the energy flux through a fixed level as it was considered by Furuichi et al. (2008) and Zhai et al. (2009), is dynamically more relevant. Here we will quantify this flux globally, using the Max Planck Institute Ocean Model (MPIOM) at 1/10° horizontal resolution that simulates a realistic temporally and spatially varying mixed layer depth with a realistic mixed layer closure

similar to Furuichi et al. (2008) and Zhai et al. (2009). We address the following questions: What is the magnitude of the wind-power input to near-inertial motions simulated with our high-resolution ocean model? How large is the fraction of the total wind-induced near-inertial energy flux that propagates out of the mixed layer (FRACTION)? What are the factors that control this FRACTION?

3.4.2 Wind-power input to near-inertial waves simulated with 1/10° and 0.4° resolution ocean model, but forced by the NCEP/NCAR reanalysis

First, we estimate the wind-power input to near-inertial motions (for short INPUT) from the 1/10° simulation and compare the result with that obtained by Rimac et al. (2013) to assess the role of model resolution. INPUT at the surface is calculated by integrating the cross-spectrum between surface lateral velocities and wind stress over the near-inertial frequency range defined by: $0.7f < \omega < 1.3f$, where f denotes the local inertial frequency. We use a Daniell estimator (von Storch and Zwiers, 1999) to estimate the cross-spectrum. For comparison we also calculate INPUT for the same two months using the same 6-hourly NCEP forcing but with MPIOM at 0.4° resolution (Rimac et al., 2013). The INPUT in the 1/10° model is 0.34 TW, which is slightly lower than 0.37 TW in the 0.4° NCEP experiment. This result indicates that the higher resolution of the ocean model does not significantly change the result. On the other hand, Rimac et al. (2013) showed that higher temporal resolution of wind stress, e.g., 1-hourly would increase INPUT up to 1.1 TW. We hence expect the INPUT to be around 1 TW when the model is forced by hourly wind stress data. As in Rimac et al. (2013) the INPUT (Figure 3.7) has a pronounced maximum around 30°-50° as a response to the intermittent passage of the mid-latitude storms. The maximum in the Northern Hemisphere in January is about 25% stronger than in the Southern Hemisphere in July (0.041 W/m^2 compared to 0.031 W/m^2) indicating that the wind variability related to winter storms is stronger in the Northern Hemisphere.

3.4.3 Total near-inertial energy flux propagating out of the mixed layer

The horizontal and vertical near-inertial energy flux at the mixed layer depth h are estimated as the cross-covariance obtained by integrating the cross-spectrum between the velocity $\mathbf{u}' = (u'(x,y,h), v'(x,y,h), w'(x,y,h))$, and the pressure $p'(x,y,h)$ (u' and p' denote a deviation from the monthly mean velocity and pressure), over frequencies ω: $0.7f < \omega < 1.3f$. An expansion or reduction of the frequency band, to e.g. $0.8f < \omega < 1.2f$, increases or decreases the result by less than 1%. The results are thus insensitive to small variations of near-inertial frequency band. The pressure is obtained by integrating the hydrostatic relation and adding the contribution from the sea surface elevation. We calculate the total near-inertial energy flux leaving the mixed layer (hereafter referred to as FLUX) as the flux of near-inertial energy across the bottom of the mixed layer at depth $z = -h$,

$$\overline{p'\mathbf{u}'} \cdot \mathbf{n} = \overline{p'u'}\frac{\partial h}{\partial x} + \overline{p'v'}\frac{\partial h}{\partial y} + \overline{p'w'}. \tag{3.1}$$

In the equation, $\overline{()}$ denotes the cross-covariance detailed above, $\overline{p'w'}$ represents the mean vertical energy flux of near-inertial waves, $\overline{p'u'}\frac{\partial h}{\partial x} + \overline{p'v'}\frac{\partial h}{\partial y}$ is the projection of the horizontal near-inertial energy flux on the slope of the bottom of the mixed layer, and $\mathbf{n}$ is the unit vector normal to

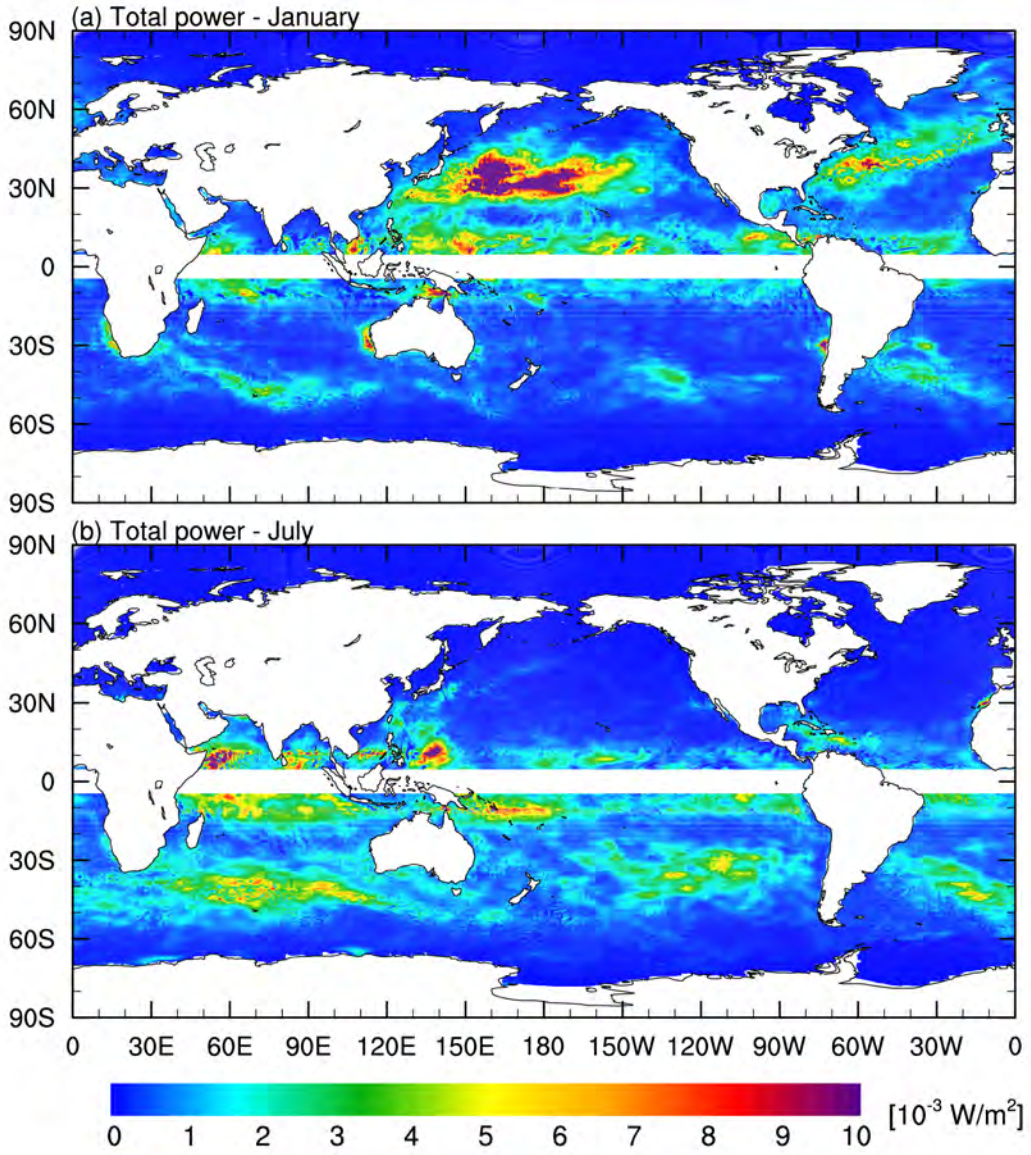

Figure 3.7: Spatial distribution of the wind-power input to near-inertial motions calculated as the cross-spectrum between current velocities and wind stress, and integrated over the near-inertial frequency range in [10^{-3} W/m^2], is presented for (a) January and (b) July. A Daniell estimator is used to estimate the cross-spectrum (von Storch and Zwiers, 1999). Note that the method based on the integrated cross-spectrum (defined by a raw cross-periodogram) is identical to the method based on data filtered in respect to the same frequency range, as shown in Appendix A.2.*

the bottom of the mixed layer which varies geographically. The projection terms contribute to the total fraction of the near-inertial energy leaving the mixed layer by less than 1% in all the calculations (Table 3.2) and are about 10% of the vertical flux. Therefore, these terms can be neglected and the knowledge of the vertical near-inertial energy flux leaving the mixed layer appears sufficient for a rough estimation of the energy available for deep-ocean mixing. However, in the following analyses FLUX is calculated using Equation (1).

The spatial distribution of FLUX is shown in Figure 3.8. FLUX is mostly negative, i.e., downward, but positive values show up at places. Large negative values of FLUX are found in the mid-latitude winter storm track regions around 20°-60° N in January (Figure 3.8a) and around

20°-50° S in July (Figure 3.8b). Negative values of FLUX are also found in January in the Southern Hemisphere around 30°-60°. Positive FLUX near the equator might arise from near-inertial waves propagating in the interior from higher latitudes upward into the mixed layer again. Some of the positive flux also appears around the continents (e.g., Gulf of Mexico, eastern coast of the South America, Bay of Bengal and Gulf of Aden), possibly due to flow topography interactions (Zhai and Marshall, 2013).

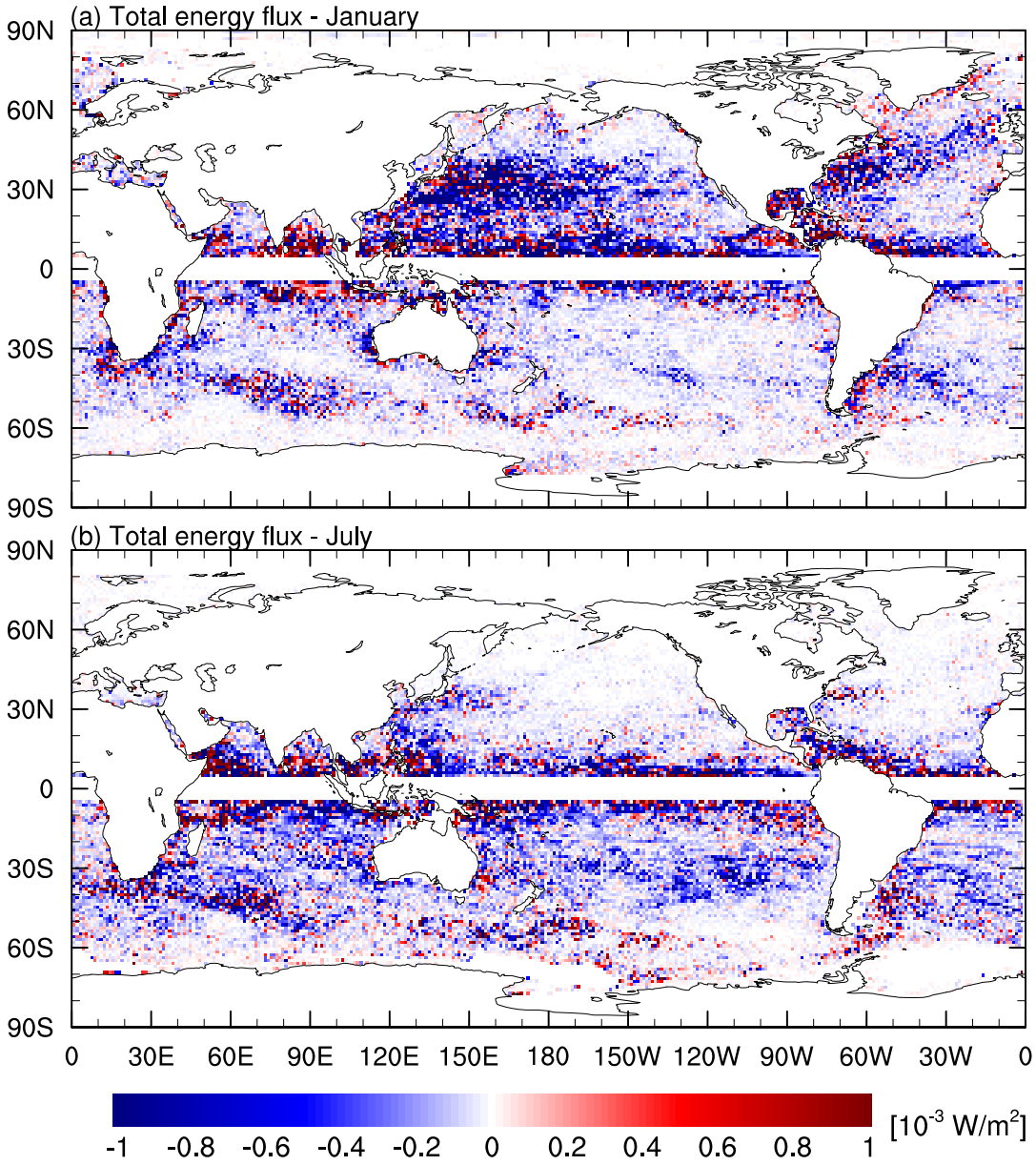

Figure 3.8: Spatial distribution of the total near-inertial energy flux leaving the mixed layer for (a) January and (c) July. Note that negative values indicate downward energy propagation. The field is interpolated to a grid of 1.1° horizontal resolution.

Further, we calculate the globally and hemispherically integrated FLUX and their ratios to the respective globally and hemispherically integrated INPUT at the sea surface (FRACTION; Table 3.2). The mean values (averages of January and July) of global FLUX and FRACTION are 0.034 TW and 10.8% respectively. In general, the values of FLUX and FRACTION depend strongly on the month and the area that are used for the calculation. For instance, the global

Table 3.2: Globally integrated wind-power input to near-inertial motions (INPUT), total near-inertial energy flux leaving the mixed layer (FLUX), near-inertial energy flux leaving the mixed layer from a projection term ($FLUX_p$), and the ratio of the integrated fluxes to the wind-power input to near-inertial motions (FRACTION) for January and July, and as the mean of the two months. Total flux and wind power input to near-inertial motions calculated separately for the Northern (NH) and the Southern Hemisphere (SH) for January, July and as the mean of the two months.

		January	July	Mean value
global:	INPUT [TW]	0.36	0.33	0.34
	FLUX [TW]	0.046	0.027	0.037
	FRACTION [%]	12.7	8.1	10.8
	$FLUX_p$ [TW]	0.001	0.004	0.003
	$FRACTION_p$ [%]	0.2	1.2	0.8
NH:	INPUT [TW]	0.24	0.08	0.16
	FLUX [TW]	0.031	0.006	0.019
	FRACTION [%]	12.9	7.5	11.9
SH:	INPUT [TW]	0.11	0.25	0.18
	FLUX [TW]	0.015	0.021	0.02
	FRACTION [%]	13.6	8.4	11.1

FLUX is almost two times smaller in July (0.027 TW) than in January (0.046 TW). The global value of FRACTION is reduced from 12.7% in January to 8.1% in July.

3.4.4 Factors that control the fraction

In Figure 3.9 we show the dependence of FRACTION on (a) mixed layer depth and (b) the strength of the wind stress variability as characterized by standard deviation of wind stress. The dependency reflects the influence of various factors that can affect the magnitude of FRACTION. One factor might be the wind stress variability. Obviously, stronger wind stress variability leads to a larger wind power input to near-inertial motions. However, stronger wind stress variability also implies stronger mixing of momentum and thus stronger dissipation of wind-induced near-inertial waves within the mixed layer. In MPIOM, the vertical momentum mixing can be changed by wind stress variability via the dependence of the mixing strength upon the cube of 10 m wind speed and via the wind-induced changes in the vertical shear and with that the Richardson number. For both processes, stronger wind stress variability will lead to stronger dissipation inside the mixed layer and will produce smaller values of FRACTION. Thus, wind stress variability might have two roles, a productive role through increasing INPUT and a dissipative role through stronger dissipation.

Another factor capable of affecting the magnitude of FRACTION is the mixed layer depth. A deeper mixed layer implies that the wind-induced near-inertial waves have to pass a thicker surface layer with strong dissipation before leaving the mixed layer. As a consequence, the magnitude of FRACTION should decrease with increasing mixed layer depth. On the other hand, the mixed layer depth is not independent of the wind stress variability, which might decrease FRACTION due to wind-induced dissipation inside the mixed layer as discussed above.

The effects of mixed layer depth and wind-stress variability on FRACTION cannot be quantified locally due to the noisy structure of grid point values of FLUX (Figure 3.8). Instead, they are

assessed using large areas defined by certain ranges of mixed layer depth or wind stress variability (Figure 3.9). We find that apart from the area with extremely thin mixed layer (i.e., 10 m $\leq$ mixed layer depth $\leq$ 40 m), the value of FRACTION decreases, by and large, with increasing mixed layer depth in both months. Furthermore, there is a noticeable tendency of decreasing FRACTION with increasing strength of wind stress variability. Our result confirms the link between mixed layer depth and the dissipation of near-inertial waves inside the mixed layer and indicates that the dissipative role outweighs the productive role of the wind forcing.

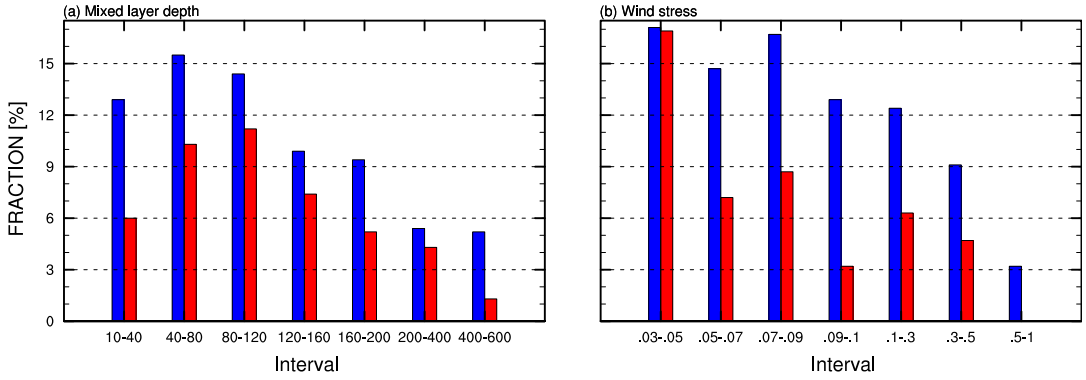

Figure 3.9: Bar plot representing FRACTION in dependence of changing (a) mixed layer depth and (b) standard deviation of wind stress. Blue bars represent results for January while red bars for July. x-axes show intervals that are used to define the domain including all grid points over which the mean values of FRACTION are calculated. For example, 10-40 in (a) means that FRACTION is calculated at grid points where mixed layer depth is between 10 and 40 m deep. We calculate FRACTION in (b) at grid points where wind stress standard deviation is e.g., 0.5-1 of the maximum value.

3.4.5 Horizontal near-inertial energy flux

Figures 3.10 and 3.11 illustrate the horizontal near-inertial energy flux integrated throurough the water column from the surface to 1000 m depth for January and July, respectively. The general distribution of the horizontal energy flux, especially its zonal component, resembles the observed near-inertial kinetic energy at the ocean surface, as we could see in Section 2.5.1 (Figure 2.11). For the meridional near-inertial energy flux, we observe strong equatorward (negative in the Northern Hemisphere and positive in the Southern Hemisphere) energy propagation away from the regions of large wind energy input, especially between 20°-60° N in January and 20°-50° S in July. If we exclude equatorial regions, the maximum near-inertial energy flux is found around 30° N in January, and around 30° S in July. The zonal near-inertial energy flux has a similar magnitude as the meridional energy flux for both months and is directed mostly towards the east (positive values). The strongest zonal flow is observed in the storm track regions, between 20°-50° latitudes. The maximum appears around 28°-35° N in January, and 30°-40° S in July. It is interesting to note that horizontal near-inertial energy fluxes in the Pacific Ocean are larger than the fluxes in the other oceans for both months. Also, the winter enhancement of the fluxes are more significant in the Northern Hemisphere than in the Southern Hemisphere. These features are in general agreement with the estimates from historical mooring records as it was shown by Alford (2003b) and to the model estimates by Furuichi et al. (2008), Zhai et al. (2009) and Simmons and Alford (2012).

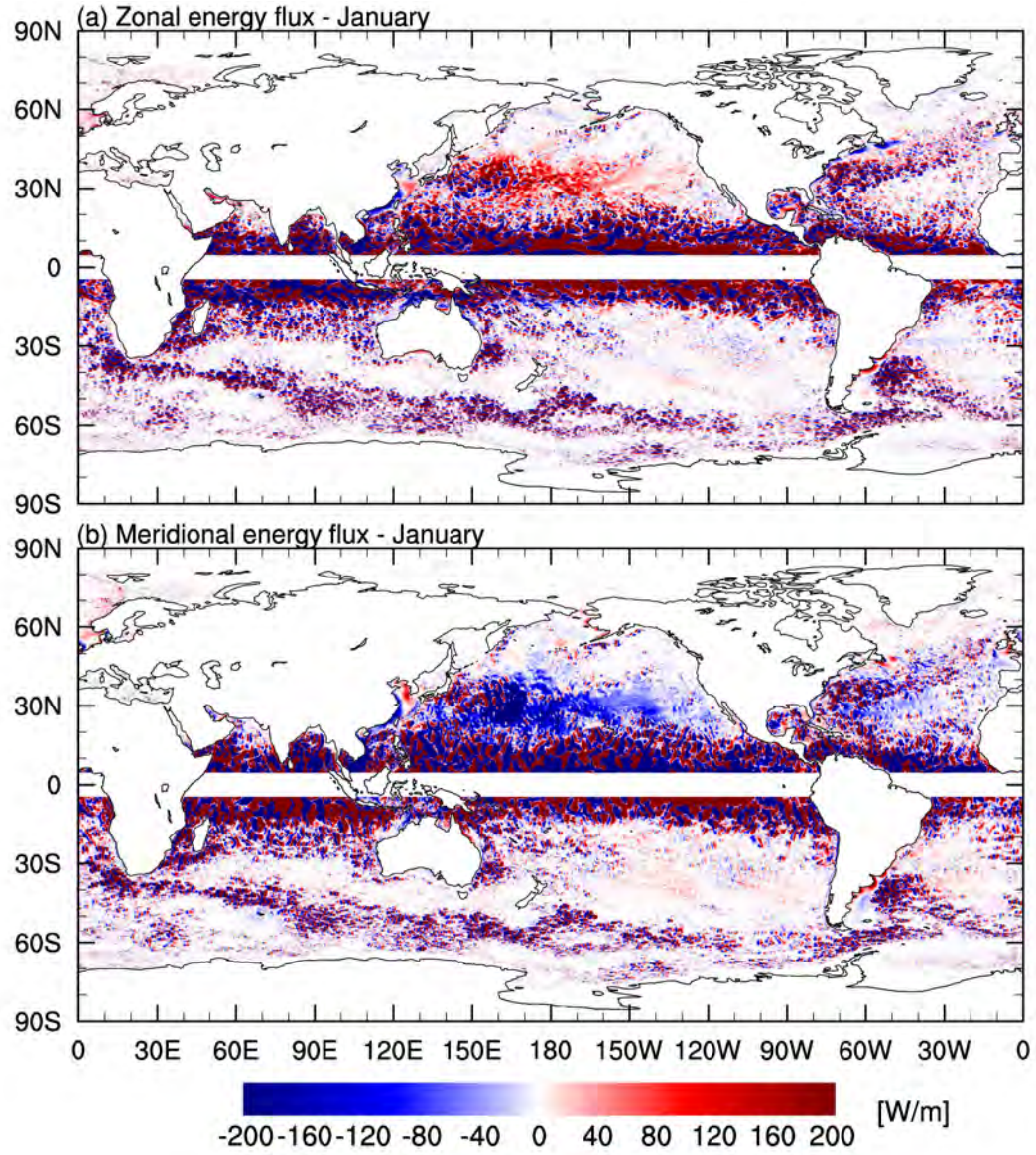

Figure 3.10: Spatial distribution of the (a) zonal $\overline{u'p'}$ and the (b) meridional $\overline{v'p'}$ near-inertial energy flux integrated from the mixed layer depth to the ocean bottom. The fluxes are calculated for January 2005. Positive values for the zonal flux indicate eastward energy propagation. Positive values for the meridional flux that dominate in the Southern Hemisphere and negative values in the Northern Hemisphere indicate equatorward energy propagation. The result is given in [W/m].

3.4.6 Discussion and conclusions

In this study, we address the fraction of the total near-inertial energy flux leaving the mixed layer (FRACTION) by using a global 1/10° OGCM with a realistic spatially varying structure of the mixed layer depth. In our study, the total near-inertial energy flux leaving the mixed layer (FLUX) shows a pronounced maximum in the mid-latitude winter storm track regions. From the wind-induced flux of 0.34 TW at the surface only about 10.8% leaves the mixed layer. The remainder of the energy is dissipated in the mixed layer. Deeper mixed layer implies stronger dissipation of near-inertial waves inside mixed layer and hence smaller values of FRACTION. Wind stress forcing generates near-inertial waves, but also damps these waves via enhanced turbulent

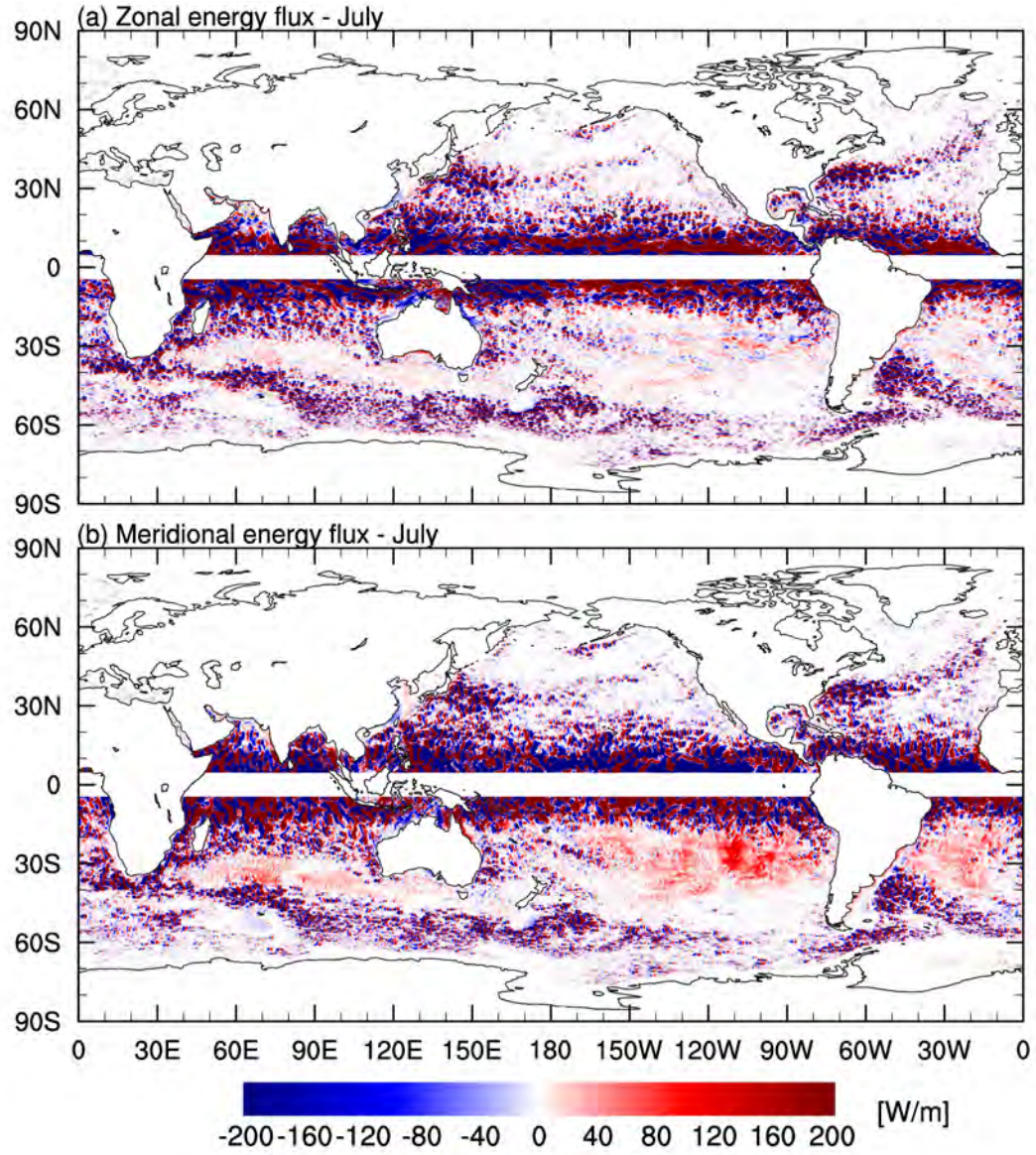

Figure 3.11: Spatial distribution of the (a) zonal $\overline{u'p'}$ and the (b) meridional $\overline{v'p'}$ near-inertial energy flux integrated from the mixed layer depth to the ocean bottom. The fluxes are calculated for July 2005. Positive values for the zonal flux indicate eastward energy flux propagation. Positive values for the meridional flux that dominate in the Southern Hemisphere and negative values in the Northern Hemisphere indicate equatorward energy propagation. The result is given in [W/m].

mixing inside the mixed layer. The dissipative role outweighs the productive role of the wind forcing. Horizontal, meridional and zonal energy flux indicate equatorward and eastward energy propagation, respectively.

It has been noted that wind stress influences the power input to near-inertial motions at the ocean surface (Rimac et al., 2013, see Chapter 2). Here, we address the strength of wind stress and its influence on FRACTION because wind stress directly influences mixing of momentum and therefore the dissipation of near-inertial waves within the mixed layer. At the same time, the mixed layer depth signifies the depth that wind-induced near-inertial waves have to pass before being able to freely propagate into the deep ocean. Therefore the realistic spatial structure of mixed layer depth is dynamically important in studying the FRACTION of near-inertial energy

available for deep-ocean mixing. The influence of these two factors, mixed layer depth and wind stress, on FRACTION has not been assessed yet. FRACTION also depends on the turbulent mixing in the ocean interior. We believe that using more sophisticated mixing scheme than the one from Pacanowski and Philander (1981) which is implemented in MPIOM would possibly give a different result. We thus suggest to perform similar analysis with different model using different mixed layer closures.

To conclude, if the mean value of the FRACTION of the total FLUX of 11% is applied, only about 0.04 TW of the wind-induced power to near-inertial motions at the surface is available for deep-ocean mixing when using the present setup of the MPIOM. Taking the whole range of uncertainty of 0.3-1.1 TW for the wind-power input to near-inertial motions into account, the present study suggests that the total wind-induced near-inertial energy available for deep-ocean mixing is small (smaller than 0.1 TW). This suggests the existence/importance of other energy sources or other energy pathways of wind-induced power (e.g., that via interaction of mesoscale eddies with the bottom topography (Nikurashin and Ferrari, 2011)).

3.5 Characteristics of near-inertial waves

3.5.1 Introduction and motivation

One of the striking aspects of deep ocean velocity profiles is the presence of depth- and time-dependent velocity fluctuations with high energy in the near-inertial frequency band (Leaman and Sanford, 1975). Although these fluctuations are commonly stronger in the oceanic mixed layer, they are present throughout the water column (Leaman and Sanford, 1975, Silverthorne and Toole, 2009, Alford et al., 2012). Kinetic energy of oceanic waves is mainly studied using a frequency spectrum. In frequency space, near-inertial waves are represented by relatively broad and prominent spectral peak with a maximum near the local inertial frequency f (Fu, 1981, Ferrari and Wunsch, 2009). Comparatively, a change of the spectral shape of the near-inertial peak (e.g., its maximum and broadness) in a frequency spectrum has long been discussed (e.g., Fu, 1981). Near-inertial waves make up about half of internal wave energy (Figure 1.1), and the power provided by the wind at the ocean surface is a substantial fraction of the power needed to sustain the global general circulation in the ocean (Rimac et al., 2013, references therein, see also Chapter 2). Therefore, a more complete estimate of their spatial and temporal characteristics than the one provided by observational studies from some localized regions, mainly in the North Atlantic and the North Pacific, is needed.

Velocity fluctuations were studied using observational data and realistic basin scale ocean models. Fu (1981) used various Polymode arrays located at the Western North Atlantic. He studied characteristics of the inertial peak (i.e., its energy level and spectral shape) but also spatial coherence and coherence scales of near-inertial waves. He showed that at most observational sites, there is a prominent inertial peak in frequency spectrum slightly above the local inertial frequency f. However, the peak maximum and its width varied when the spectrum was estimated for different depths, and they depended on geographical environment in which the Polymode had been deployed. Near f, the horizontal coherence scale was estimated to be about O(60 km) at depths from 200 to 600 m, and the vertical coherence scale was about O(200 m) in the lower part of the main thermocline and about O(1000 m) in the deep water. In the study by Fu (1981), the phase spectrum suggested a downward energy propagation in the lower thermocline and standing waves in the deep water. On the other hand, Danioux et al. (2011) used a basin scale ocean model forced by uniform wind stress data. They showed the presence of energetic near-inertial waves with a mean amplitude of vertical velocity of 25 m/day in the deep ocean (around 2500 m), a dominant peak at $2f$ frequency, and a characteristic length scale of these waves as small as 30 km. They pointed out on the relative importance of the duration of the wind forcing and of the model resolution on generation of near-inertial waves.

The previous studies thus indicate the existence of energetic near-inertial waves in the ocean but their spatial and temporal scales are poorly assessed because the analysis were based on sparse amount of observational sites, mostly located in the North Atlantic and Pacific regions while the Southern basins due to low amount of available data were not covered. We however, can study the whole range of spatial and temporal scales using hourly output of a simulation performed with a global Ocean General Circulation Model (OGCM), the Max Planck Institute Ocean Model (MPIOM), at 1/10° horizontal resolution and 80 vertical levels. We examine characteristic scales of near-inertial waves and their propagation in horizontal and vertical direction on a global domain. We address the following questions: What is the spatial length scale of near-inertial waves? Are

near-inertial waves dominant motions in the ocean energy spectrum? Are simulated motions waves or simply oscillations? How do wind-induced near-inertial waves propagate horizontally and vertically?

Throughout this subchapter, the analyses of characteristic scales of near-inertial waves are based on vertical velocity. Vertical velocity is an important variable in the ocean on a vast range of scales. It can be used not only to quantify the upwelling and downwelling related to the global overturning circulation but it can also describe small-scale processes such as internal waves that are crucial for deep ocean circulation (von Storch, 2010). Internal waves can significantly contribute to the variability of the vertical velocity. We use vertical velocity from the global model not only because of the sparseness of the observational sites but also because of the difficulty in directly measuring vertical velocity that is a few orders of magnitude smaller than horizontal velocity. At the same time, vertical velocity is not so strongly "contaminated" by the quasi-geostrophic eddy field, as it is the case for horizontal velocity. Hence, near-inertial waves can be studied using raw vertical velocity without applying any filter beforehand.

So far we could see that for a more complete description of near-inertial waves, than it is provided by observational studies, we need a global OGCM at high horizontal and vertical resolution. Also, we argued that we can analyze characteristics of near-inertial waves based on vertical velocity since it is not so strongly "contaminated" by the quasi-geostrophic eddy field. In Figure 3.12a and 3.13a, a snap shot of vertical velocity at 500 m is shown for January and July, respectively. In these figures we find strong mostly zonally oriented stripes with a mean vertical velocity of $12{\cdot}10^{-8}$ m/s. The observed stripes recall wave crests and troughs and they can be found in all ocean basins. The stripes are less prominent and with more randomly changing sign in the North Hemisphere around eastern borders of Asian and North American continent, and in the Southern Ocean (mainly in the Indian and Atlantic Ocean) poleward of 40° S. The question that arises is which areas to choose to study characteristic scales of near-inertial waves. In our analyses, we decide for the areas where vertical velocity is strong, where it shows wave structures and it is outside regions with strong mesoscale eddies. The highlighted areas in Figure 3.12a and 3.13a correspond very well to our criterion. To envisage our choice of areas used for detailed analysis, in Figure 3.14 we give a closer look of all chosen areas. Our analyses are done for two oceanic levels, i.e., mainly around 100 and 500 m for January and July 2005 separately. We choose these depths because at 100 m near-inertial waves are not under the direct influence of the atmospheric forcing and at 500 m vertical velocity is the strongest in our simulations.

3.5.2 Wavenumber spectra of the vertical velocity

In this section, for the purpose of analyzing spatial structure of near-inertial waves in the ocean and examining their horizontal length scale in detail, we calculate a wavenumber spectrum of vertical velocity. We study horizontal length scale of near-inertial waves using a two-dimensional Fourier decomposition that is described in Appendix A.3.

Figures 3.12b and 3.13b represent a horizontal wavenumber spectra for January and July, respectively. The spectra are obtained for the areas highlighted in Figure 3.12a (for a closer look of the highlighted areas we refer the reader to Figure 3.14). They are calculated for couple of time steps in January and July, and then represented as their mean value. The wavenumber spectra are shown for 100 m (solid lines) and 500 m (dashed lines). It can be seen that in January the

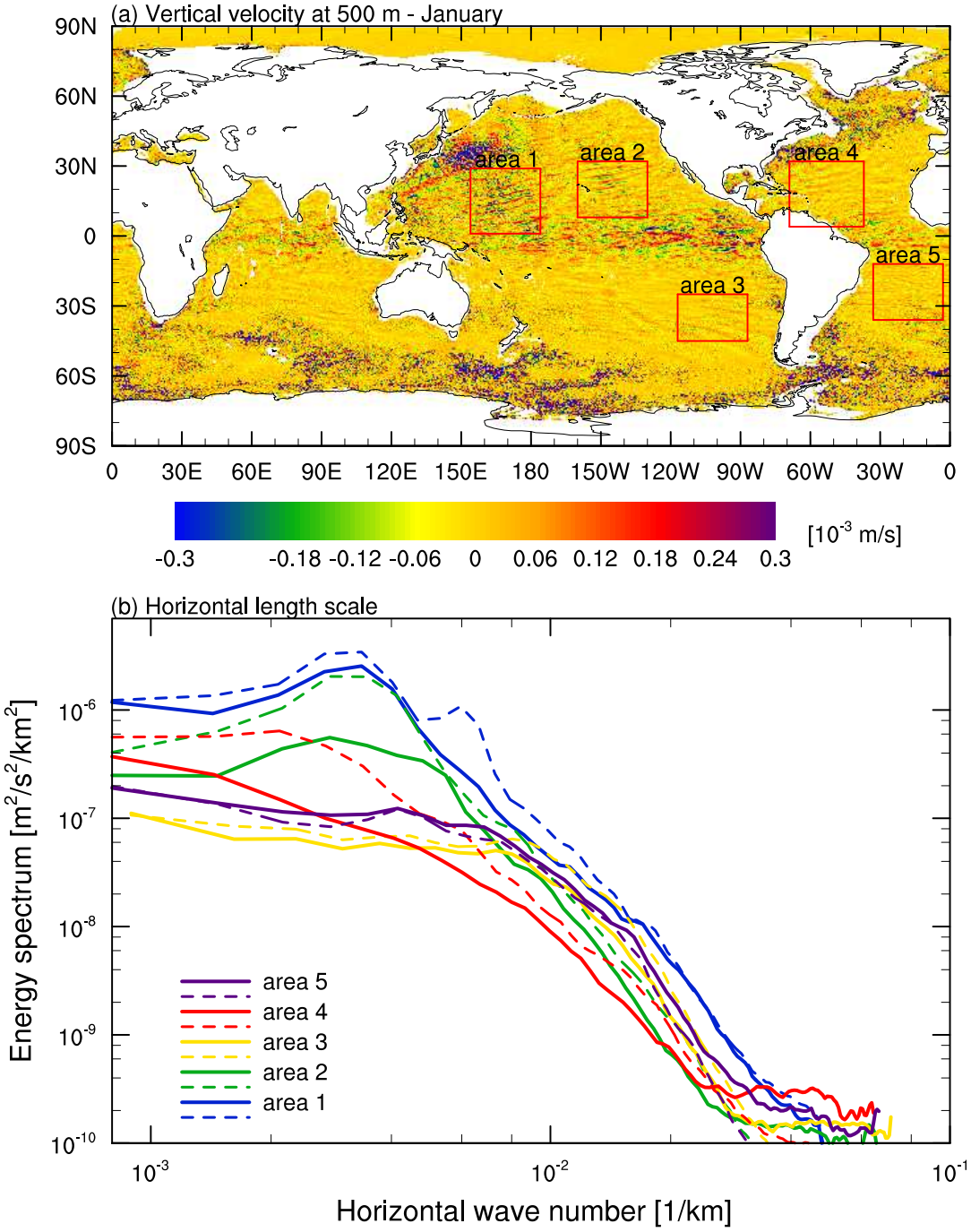

Figure 3.12: (a) Spatial distribution of the vertical velocity at 500 m. (b) Horizontal wavenumber spectra calculated for depths of 100 m (solid lines) and 500 m (dashed lines) for January. Spectra are calculated using vertical velocity from the areas highlighted in red color.

wavenumber spectra at two different levels show broad peaks. Maximum of the peaks is only evident for area 1 and area 2 (for both levels) and for area 4 at 500 m. For other areas, energy either decreases from the lowest to the highest resolved wavenumber (area 4 at 100 m), or it shows almost flat spectral shape up to wavelength of about 170 km (area 5) or 100 km (area 3) after which the energy decreases. For area 1, area 3 and area 5 spectral shapes are very similar at both depths (with an exception of evident secondary maximum at wavelength of 168 km for area 1 at 500 m), which indicates that the wavelength of near-inertial waves does not change

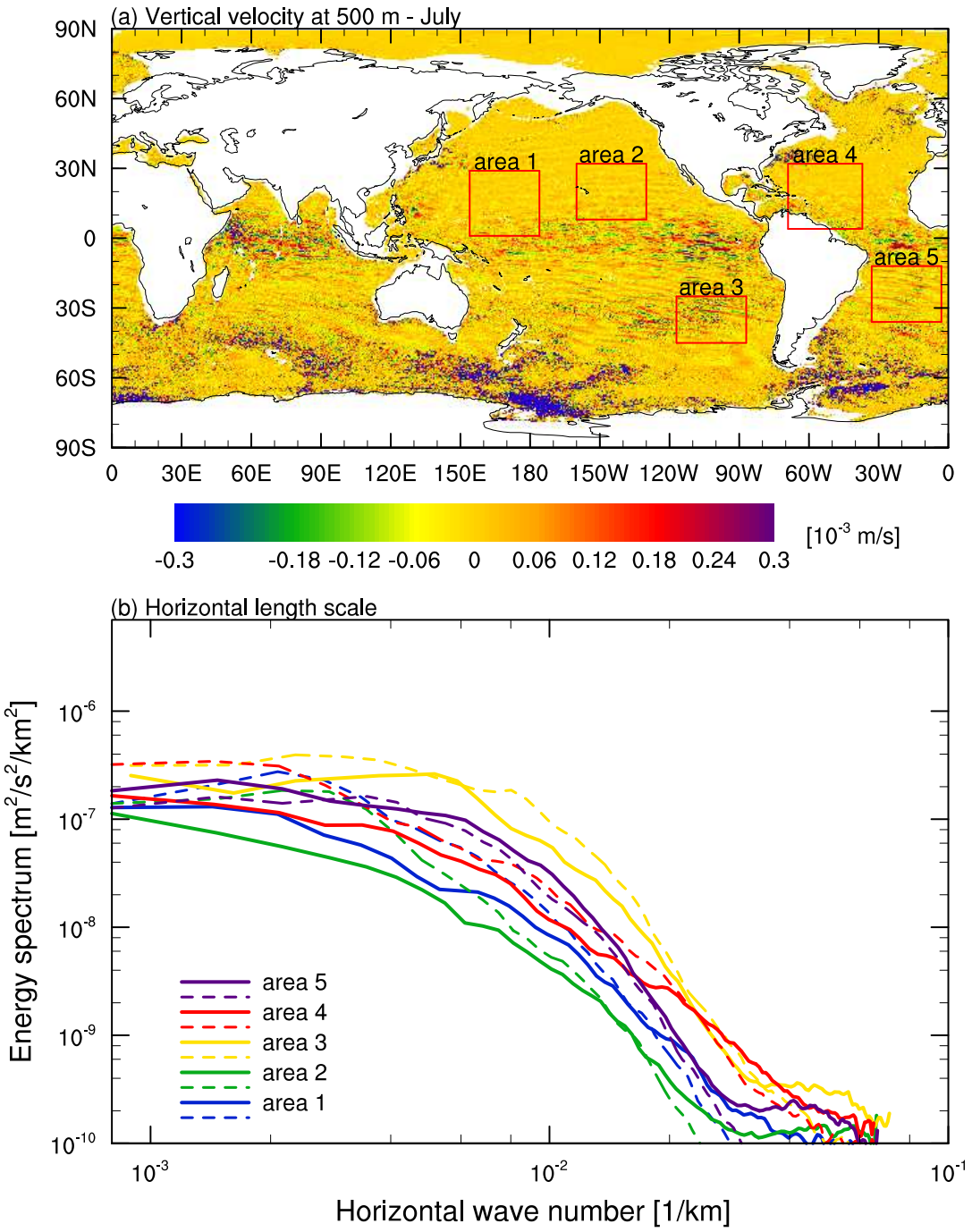

Figure 3.13: (a) Spatial distribution of the vertical velocity at 500 m. (b) Horizontal wavenumber spectra calculated for depths of 100 m (solid lines) and 500 m (dashed lines) for July. Spectra are calculated using vertical velocity from the areas highlighted in red color.

significantly throughout the water column for these areas, or at least in the first 500 m. In July, the spectra show for almost all areas energy decrease from the lowest to the highest resolved wavenumber. Exceptions are area 5 at 500 m and area 3, but the peaks are not evident and the maximum of the peaks is not apparent. Except for the spectral shape, some other differences between January and July are found. In general, in January wavenumber spectra have higher energy when calculated for areas from the Northern Hemisphere, while in July spectra calculated for areas from the Southern Hemisphere have higher energy. Also, in January spectral shapes

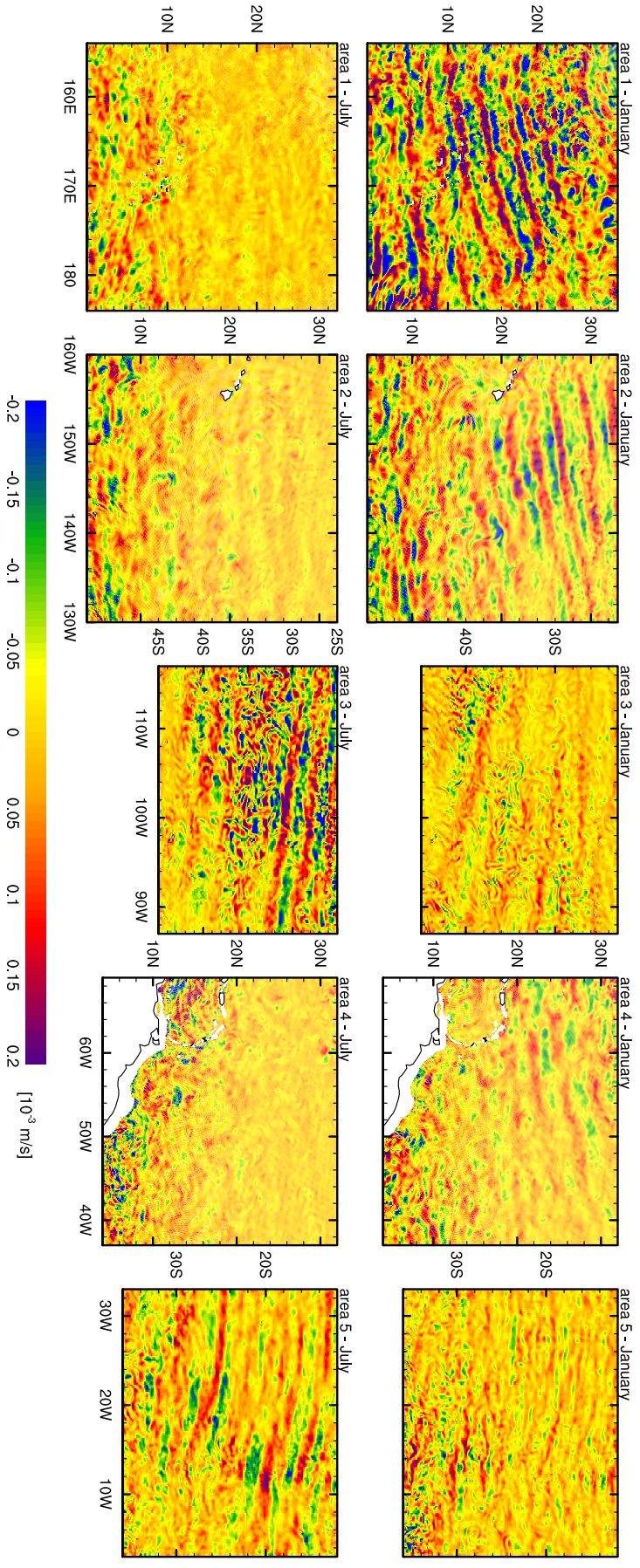

Figure 3.14: Spatial distribution of the vertical velocity at 500 m for January (top panel) and July (bottom panel). Shown areas are the same as the ones highlighted in red in Figure 3.12a.

change strongly over low wavenumbers from one area to another. This change is not seen in July.

From wavenumber spectra we can conclude that it is difficult to identify the wavelength from two-dimensional wavenumber spectra for our chosen areas. Nonetheless, in Table 3.3 we show the maximum of each spectrum to obtain a broad overview of possible wavelengths for two depths and two months. We present the wavelength for each area where the energy is the highest. For some areas, such as area 4 in January, a correct estimate could not be made, because the spectral shape decreases from the lowest to highest wavenumber and additional maximum is not evident. Numbers in parenthesis represent secondary maxima of the wavenumber spectra for the areas where they are noticed. In January wavelengths at two depths are almost identical, with wavelengths around 250-350 km. Two differences can be seen though. First, in area 1 there is a strong secondary maximum at a wavelength of 168 km at 500 m, and second, in area 4, the correct estimate cannot be made at 100 m. Although in July, spectra shown in Figure 3.13b have similar shapes at both depths with decreasing energy from the beginning of the spectrum, wavenumbers differ between two levels for all areas (except area 1), also for area 2, area 4 and area 5 at 100 m the estimate cannot be made.

Table 3.3: Area name and wavelength calculated from vertical velocity for January and July at 100 m and at 500 m. Wavelength is calculated using a two-dimensional Fourier decomposition. Numbers in parenthesis denote secondary maxima seen in wavenumber spectrum in Figure 3.12b for January and 3.13b for July. The estimate is not shown for areas where the energy decreases from the lowest to the highest wavenumber.

	Area	Wavelength for January [km]	Wavelength for July [km]
100 m deep:	area 1	297	481
	area 2	357	-
	area 3	268	195
	area 4	-	-
	area 5	241	-
500 m deep:	area 1	297 (168)	481
	area 2	357	357
	area 3	268	433 (125)
	area 4	476	476
	area 5	241	284

Finally, we are interested in whether the waves propagate mainly in zonal or in meridional direction. We integrate two-dimensional spectra calculated using the method from Appendix A.3 (Equation A.12) over all zonal or meridional wavenumbers. Left panels in Figure 3.15 for January and 3.16 for July represent the integrals over all zonal wavenumbers, while right panels represent the integrals over all meridional wavenumbers. Spectra are presented at 100 m (solid line) and at 500 m (dashed line). In January, spectral peaks in meridional direction are evident for area 1 and area 2 at both depths, and area 4 at 500 m. The peaks are not clear for area 3 and area 5 and the spectral shape is almost flat with small maximum around wavelength of 100 km. In July, the spectral peaks are evident for area 1, area 2 and area 3 at 500 m and area 3 at 100 m. In other areas and other depths, spectral shape is almost flat with small maximum at wavelength of 100 to 200 km. This analysis would indicate that waves have mainly meridional direction for all areas and both months.

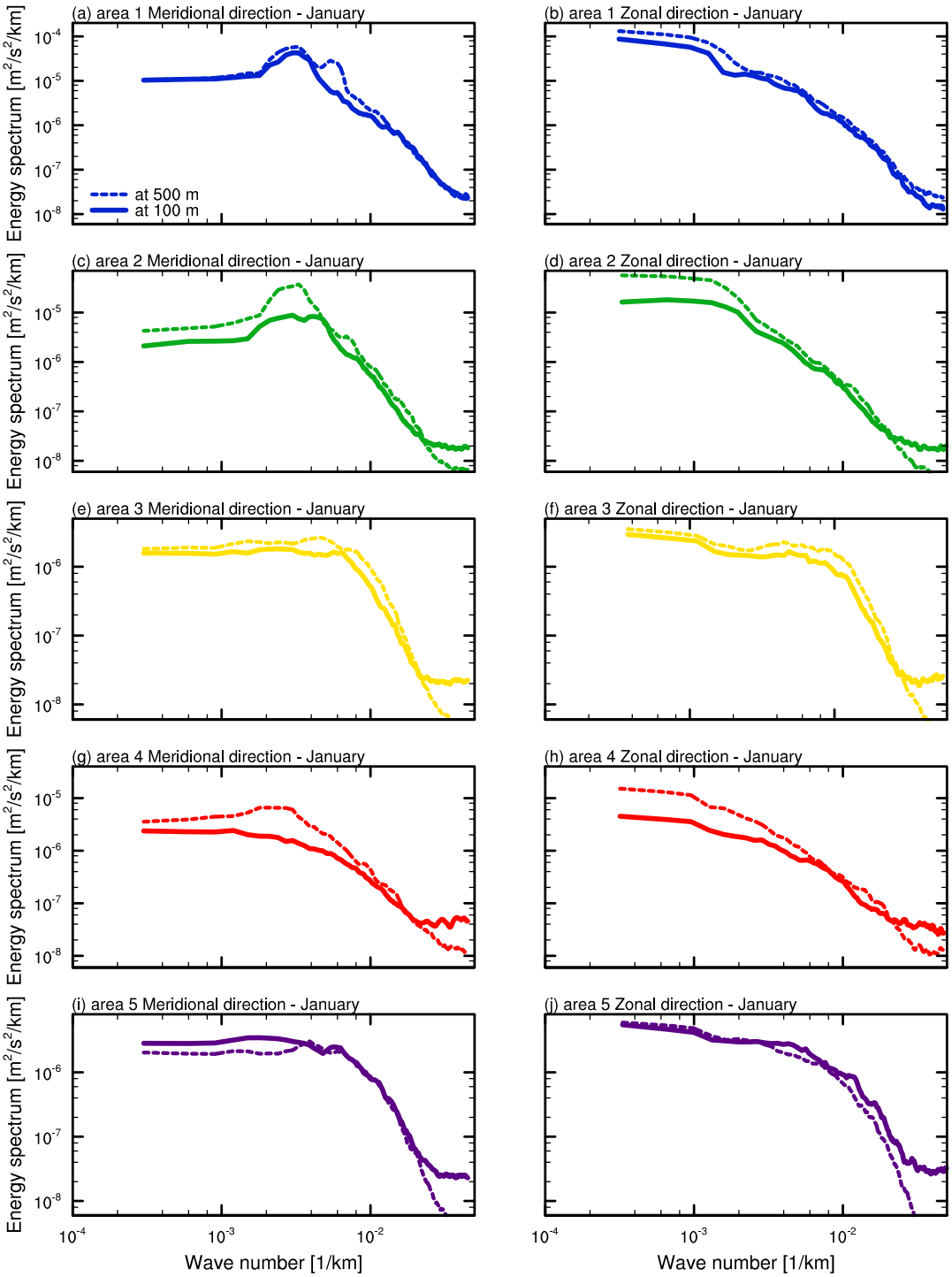

Figure 3.15: Horizontal wavenumber spectra calculated using vertical velocity from the areas depicted in Figure 3.12a at depths of 100 m (solid line) and 500 m (dashed line) for January. Spectra are calculated as an integral over all zonal (left panel) and all meridional (right panel) wavenumbers. Colors represent the estimates from different areas and they correspond to the ones from Figure 3.12b.

3.5.3 Frequency spectra of the vertical velocity

In this section, we analyze frequency spectra with the emphasis on the frequency band near the inertial frequency f. In particular, we examine the energy level, width and spectral shape of the

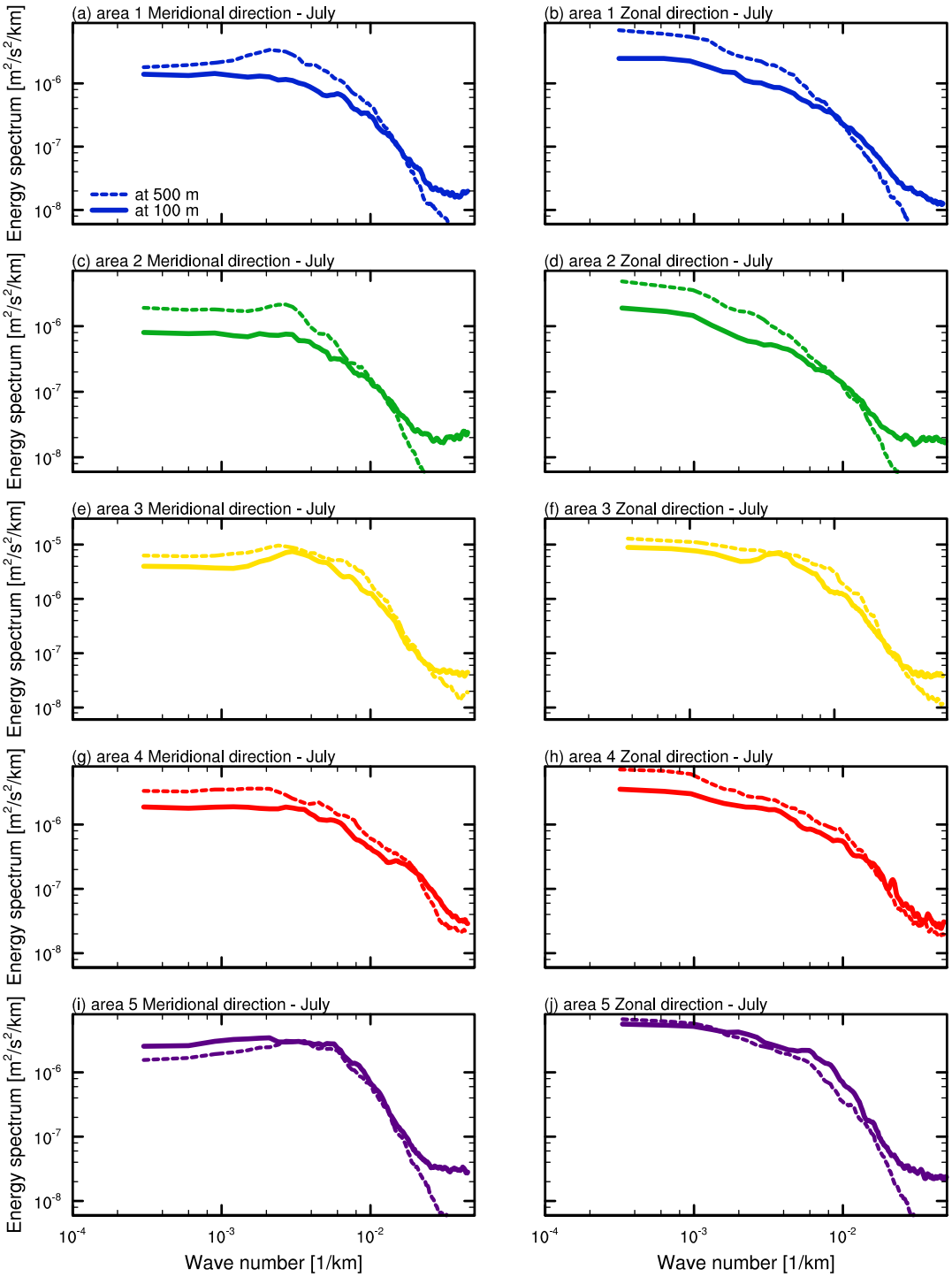

Figure 3.16: Horizontal wavenumber spectra calculated using vertical velocity from the areas depicted in Figure 3.13a at depths 100 m (solid line) and 500 m (dashed line) for July. Spectra are calculated as an integral over all zonal (left panel) and all meridional (right panel) wavenumbers. Colors represent the estimates from different areas and they correspond to the ones from Figure 3.13b.

inertial peak by computing frequency spectra of vertical velocity for different areas in the ocean introduced in Section 3.5.2, and at two different depths. Frequency spectra are computed for several neighboring grid points taken from the center of each area, and the result is presented as their mean value. The resulting spectra are shown in Figure 3.17 for January (left panel)

and July (right panel). We show the spectra calculated for 100 m (black line) and 500 m (blue line) in the ocean. Green dashed lines represent local inertial frequency f, and the double inertial frequency $2f$. All frequency spectra have similar shape outside the frequency band of near-inertial waves. Slightly below f the energy starts to increase. It is followed by the conspicuous inertial maximum in the vicinity of f. The energy then decreases in the frequency domain of internal waves (frequencies higher than f). For some areas (except for area 4 in January and area 2 at 100 m in July) the energy again starts to increase close to $2f$, and it is followed by relatively small secondary maximum.

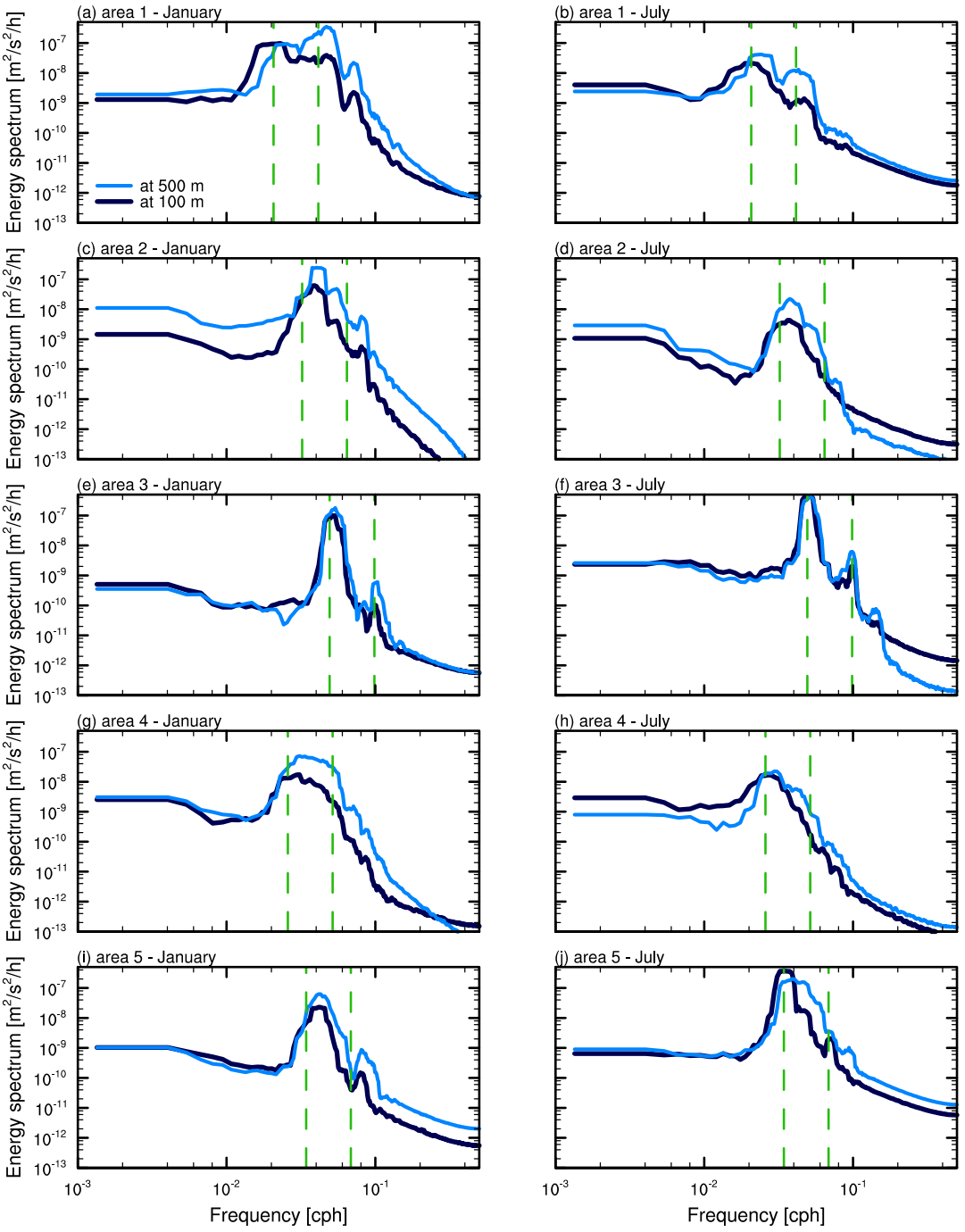

Figure 3.17: Frequency spectra calculated using vertical velocity for the areas depicted in Figure 3.12a at depths of 100 m (black) and 500 m (blue) for January (left panel) and July (right panel). Green lines represent local inertial frequency f, and the double inertial frequency 2f.

We can see that the spectral shapes defer between all areas and an universal shape in the frequency range of near-internal waves (frequencies around f and $2f$) is not evident. It is interesting to find whether there is any correlation between variability in spectral shapes and the environment from which vertical velocity was taken. Three different spectral shapes can be defined from our frequency spectra depending on the distance from the equator and the physical environment. For a closer view, in Table 3.4 we give the geographical latitude of the center of the box from where the grid point time series to calculate the spectra are taken. It can be seen that mentioned area 1 and area 4 are closest to the equator, while area 3 is furthest from the equator. In Figure 3.17, first, we can see that frequency spectra have broader inertial peak when calculated for areas closer to the equator (area 1 and area 4) than when calculated for the areas further away from the equator (e.g., area 3). Simultaneously, these peaks are also less pronounced, meaning that the height of the inertial peak is smaller in contrast to the peaks from other areas. Also, the peaks for those areas (area 1 and area 4) do not occur at the local inertial frequency f (and at double inertial frequency $2f$) but at higher frequencies. This suggests that the frequency of the locally generated inertial waves has been shifted to the higher frequency due to interaction with the waves propagating from higher latitudes. The shift of the local peak is more pronounced at 500 m than at 100 m. Second, for the areas further away from the equator (area 2 and area 5), centered around 20° latitudes, the spectral peak becomes narrower and it is higher compared to area 1 and area 4. Frequency shift is still obvious and the peak at $2f$ becomes more noticeable. Third, for area 3 centered around 36° S the inertial peak in the frequency spectrum is the highest compared to the spectral peak from other areas. Also, the peak is very narrow and it does not show almost any frequency shift for either of the two depths.

Table 3.4: Area name and the geographical latitude of the center of the box from where the grid point time series are taken to calculate frequency spectra.

Area	area 1	area 2	area 3	area 4	area 5
Latitude	14.34° N	22.65° N	36.14° S	17.98° N	24.22° S

3.5.4 Horizontal and vertical propagation of near-inertial waves

Coherence and phase of a variable at two positions can be used to describe a wave propagation in space. For instance, if a wave propagates from position 1 to position 2, the vertical velocity related to the wave at position 1 would be correlated to that at position 2 with a well defined phase shift. In this case, a high coherence can be found at the wave frequency. From the distance between the two positions and the phase difference at the wave frequency, the phase speed of the wave or at least the direction of the phase speed, can be estimated. In this section, we make use of coherence and phase to see the distance over which two waves are correlated and to study the possible wave propagation in horizontal and in vertical direction. Moreover, the phase difference indicates whether the motions are standing or propagating waves. If the obtained motions represent standing waves, the phase between vertical velocities at two separated grid points would be zero or 180°-out-of phase. On the other hand, if the motions represent propagating waves, the phase between two grid points will be generally non-zero. We give a detailed explanation of the used method in Appendix A.4.

Horizontal propagation

In this section we study coherence and phase of pairs of horizontally separated grid points. Coherence and phase are calculated between pairs of grid points located along one longitude such that one of the points x_1 is always the same or fixed, but the second point x_2 moves southward. The second point will therefore in each iteration have larger distance to the fixed point x_1. We look at waves propagating at the local inertial frequency f of point x_1 by determining the coherence and phase at the inertial frequency between the fixed point x_1 and point x_2 (for x_2 that is located increasingly further south relative to x_1). If the near-inertial waves are propagating motions, a progressive change of the phase with x_2 will occur.

We calculate the coherence and phase spectra between vertical velocities at pairs of grid points (x_1, x_2) at 500 m along a longitude in areas shown in Figure 3.14. Figure 3.18 and 3.19 show the coherence and phase at local inertial frequency of grid point x_2 as a function of the distance to grid point x_1. Horizontal green lines represent the 90% confidence level of zero coherency, which is about 0.312. We calculate coherence and phase along one longitude where the wave structures from Figure 3.14 are the strongest. This longitude changes between the areas. In Table 3.5 we give an overview of the used longitudes for each area.

Table 3.5: Area name and geographical longitude from which the grid points x_1 and x_2 are taken to calculate coherence and phase.

Area	area 1	area 2	area 3	area 4	area 5
Longitude (January)	162° E	152° W	105° W	60° W	8° W
Longitude (July)	154° E	154° W	94° W	58° W	18° W

The figures show that at local f of x_2, high coherence is present over a longer distance for area 4 and area 5 in January, and area 3 and area 5 in July. Coherence is high when grid points x_1 and x_2 are relatively close. It decreases as the grid point x_2 moves southward, and at one point it crosses the critical value defined by 90% confidence level of zero coherency. Coherence further decreases almost to zero but for some areas it starts to increase again. This increase might indicate that waves at grid points x_1 and a new point x_2 have similar structure. We use the point where the coherence first time passes the critical value to define a distance over which waves reveal coherent structures. We shell address this distance as a coherence scale. This is the scale over which waves have not been significantly affected by processes, such as the dissipation process implemented in the model. To have a better overview of a coherence scale for different areas, we summarize our results in Table 3.6. The coherence scale is usually higher, about 110 to 240 km, for areas with strong wavy structures (these wavy structures can be seen in Figure 3.14) spanning through all latitudes (e.g., area 2, area 4 and area 5 in January). Also, it is lower, about 30 km, for areas where this wavy structures are seen only in small localized regions (e.g., area 2 in July).

Phase indicates whether simulated motions are propagating or standing waves. Also, it shows a propagation direction of near-inertial waves. From right panel of Figure 3.18 and 3.19 we can conclude that our simulated near-inertial motions are propagating waves, since the phase between two previously defined grid points x_1 and x_2 changes in respect to the distance between these two grid points. To determine the direction of the wave propagation we consider the sign of the phase.

Table 3.6: Area name and horizontal distance between two grid points x_1 and x_2 for which coherence is still above critical value. The distance is calculated by multiplying number of grid points after which the coherence crosses critical value defined by 90% confidence level of zero coherency and the approximate grid distance in meridional direction of 10 km.

	Area	Distance in January [km]	Distance in July [km]
500 m deep:	area 1	50	90
	area 2	110	30
	area 3	20	240
	area 4	150	60
	area 5	220	220

Since in our calculation stationary point x_1 is always north from the moving point x_2, negative initial phase indicates that waves are propagating towards south. Contrary, positive initial phase would indicate northward wave propagation. The right columns show that in area 1, area 2, and area 4 near-inertial waves propagate towards south, while in area 3 and area 5 waves propagate towards north. Looking at the position of our defined areas on a global domain we can conclude that in all areas waves propagate towards the equator.

Vertical propagation

In this section we study coherence and phase of pairs of vertically separated grid points. We calculate coherence and phase between pairs of grid points taken from the center of each area in Figure 3.14 located along one vertical, such that one of the points x_1 is placed at 12 m in the ocean, but the second point x_2 moves downward. This second point will therefore in each calculation have larger distance from the fixed point x_1. We look at waves propagating at the local inertial frequency by determining coherence and phase between vertical velocities at these two points at the inertial frequency as a function of the distance between x_1 and x_2.

Coherence (Figure 3.20 and 3.21, left panel) is again relatively high for very close grid points. In most of the cases (except for area 3 and area 5 in January and area 5 in July) it is strongly damped after only several depths. This means that waves become uncorrelated after only several depths compared to the waves at 12 m. We use the point where the coherence first time passes the critical point to define a coherence scale in vertical direction. To have a better overview of the coherence scale for different areas, we summarize our results in Table 3.7. The results suggest that the vertical coherence scale is more than 50 m in all areas. Two exceptions can be seen though. In area 3 in January and area 5 in January and July the coherence scale is about 500 to 800 m.

Based on previously defined criterion that the phase between grid points x_1 and x_2 has to change in respect to the distance between these grid points, the phase diagrams depicted in right panel of Figure 3.20 and 3.21 show that over the defined coherence scale, our simulated near-inertial motions propagate. The direction of the wave propagation can be estimated from initial sign of the phase. In our calculation moving point x_2 is always positioned at deeper level from the stationary point x_1. Therefore, negative phase would indicate downward wave propagation and positive phase would indicate upward wave propagation. From the phase we can see that waves have upward propagation when the calculation is done for our chosen grid points.

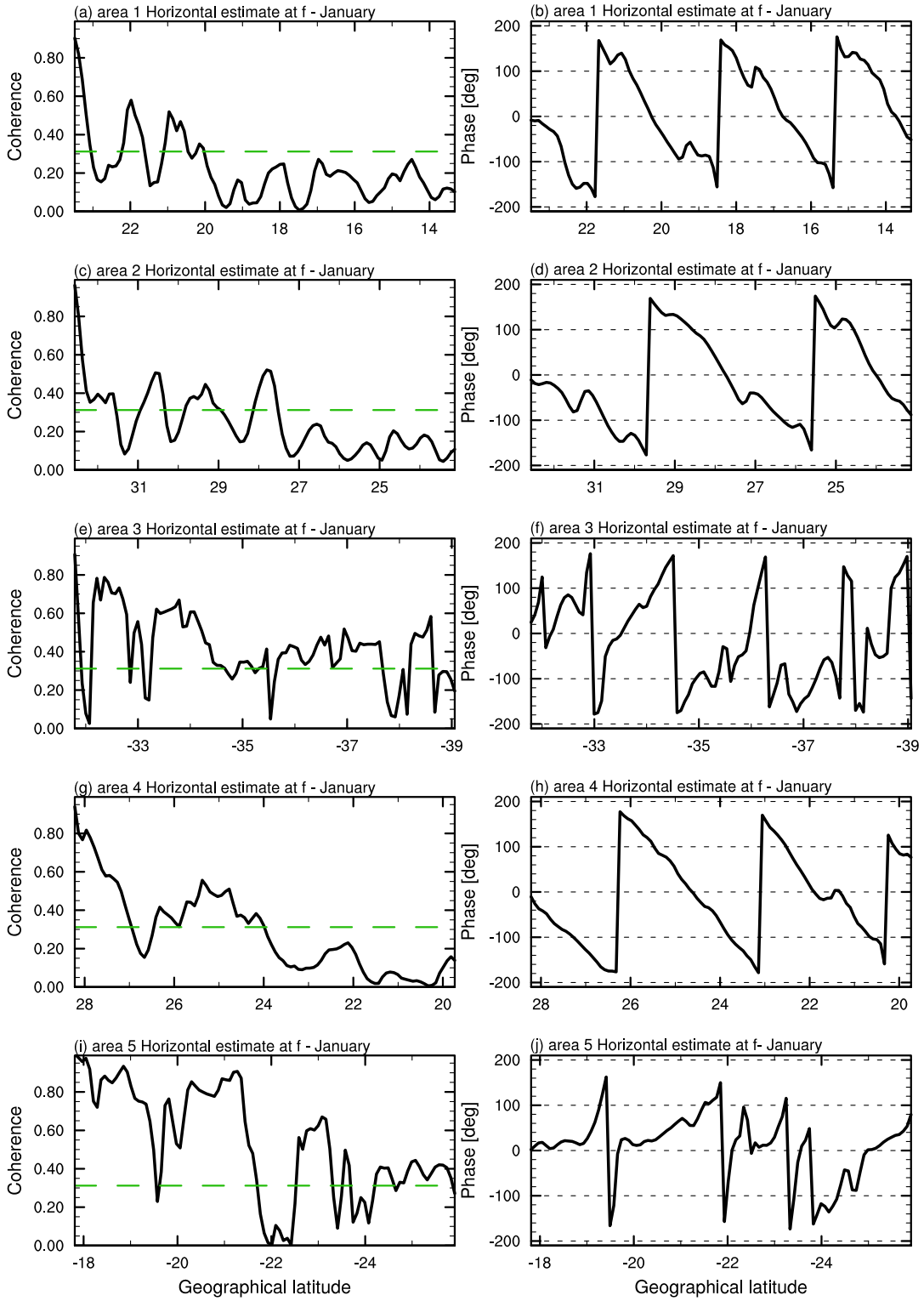

Figure 3.18: (Left panel:) Coherence between pairs of grid points (x_1 and x_2, where x_1 is always fixed point while x_2 moves southward) located along one longitude (Table 3.5) calculated using vertical velocity for each area in Figure 3.12a. Green line represents the critical value at 90% confidence level of zero coherency. (Right panel:) Phase between pairs of grid points located along one longitude calculated using vertical velocity for the same areas. Coherence and phase are estimated at local inertial frequency f of grid point x_2. Figures show the results obtained for January at 500 m.

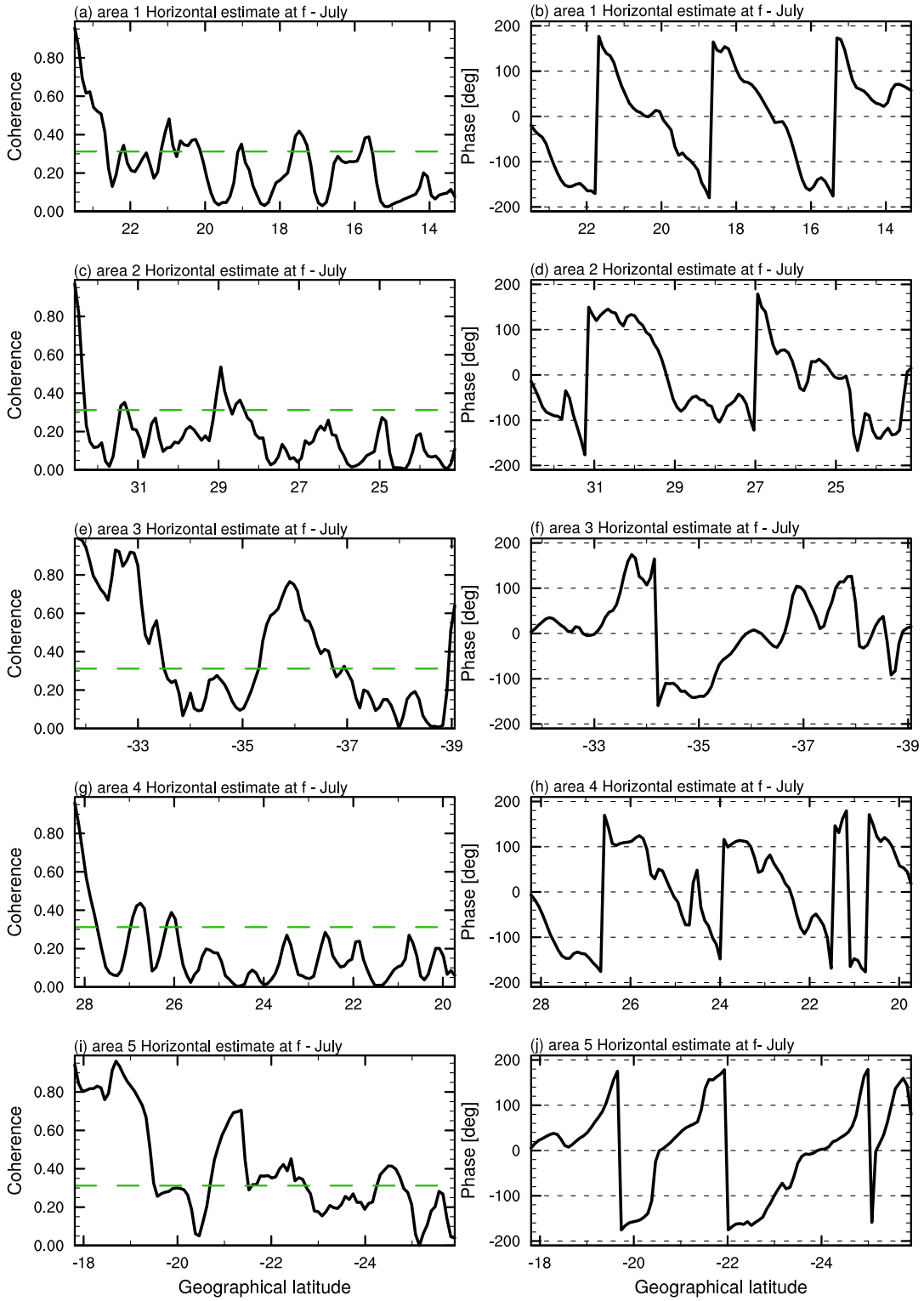

Figure 3.19: (Left panel:) Coherence between pairs of grid points (x_1 and x_2, where x_1 is always fixed point while x_2 moves southward) located along one longitude (Table 3.5) calculated using vertical velocity for each area in Figure 3.13a. Green line represents the critical value at 90% confidence level of zero coherency. (Right panel:) Phase between pairs of grid points located along one longitude calculated using vertical velocity for the same areas. Coherence and phase are estimated at local inertial frequency f of grid point x_2. Figures show the results obtained for July at 500 m.

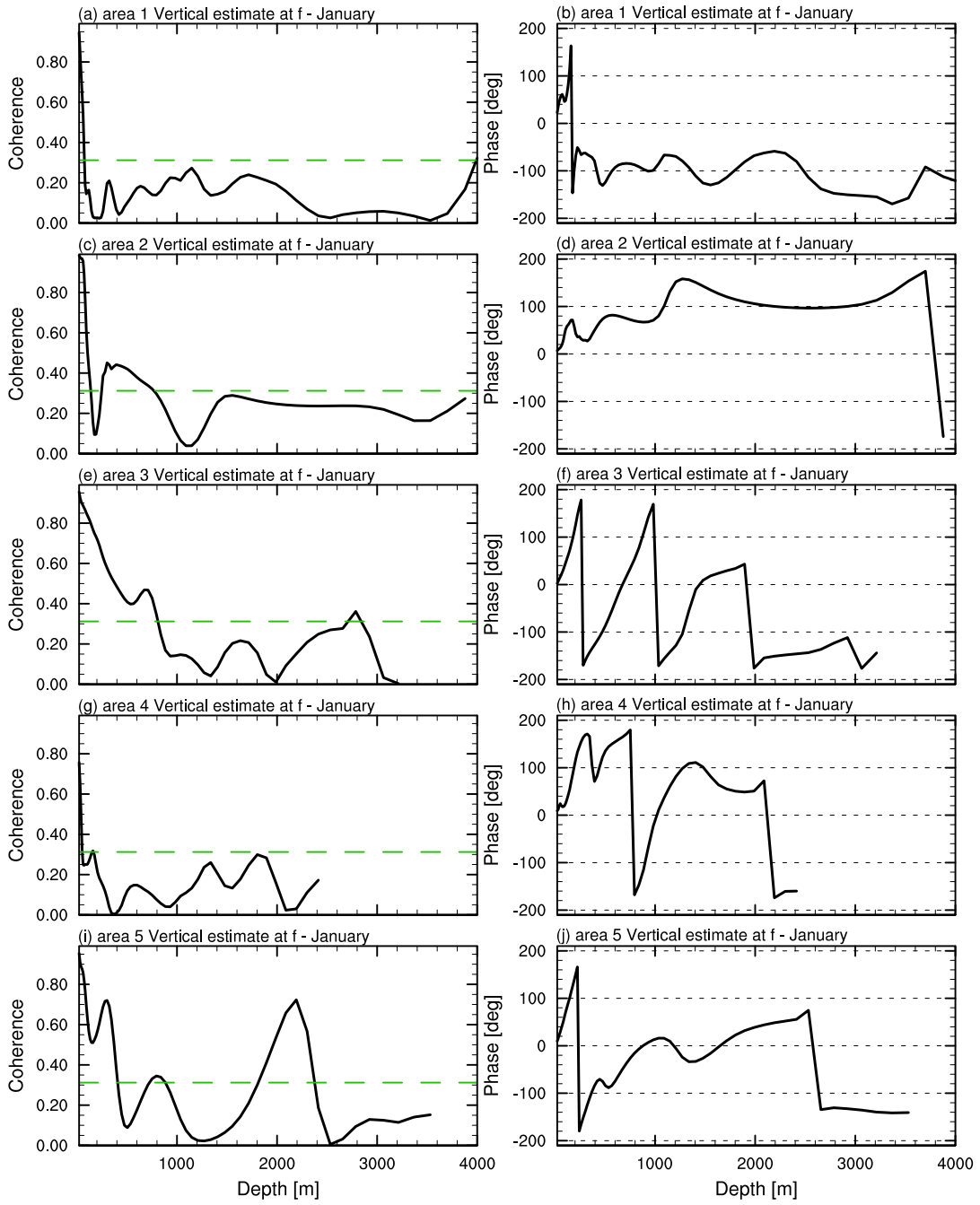

Figure 3.20: (Left panel:) Coherence between pairs of grid points (x_1 and x_2, where x_1 is always fixed point while x_2 moves downward) located at the center of each area from Figure 3.12a. Green line represents the critical value at 90% confidence level of zero coherency. (Right panel:) Phase between pairs of grid points at the center of each area. Coherence and phase are estimated at local inertial frequency f of grid point x_2. Figures show the results obtained for January.

Propagation of near-inertial waves at frequencies higher than *f*

So far we could see that the coherence calculated at the inertial frequency of the moving point x_2 as a function of x_1 yields a scale ranging from 20 to 240 km in horizontal and 50 to 826 m in vertical direction. From the phase between two grid points, which are increasingly separated from each other, we concluded that the simulated near-inertial motions are propagating waves. We also estimated the direction of wave propagation (equatorward in horizontal, and from the deep

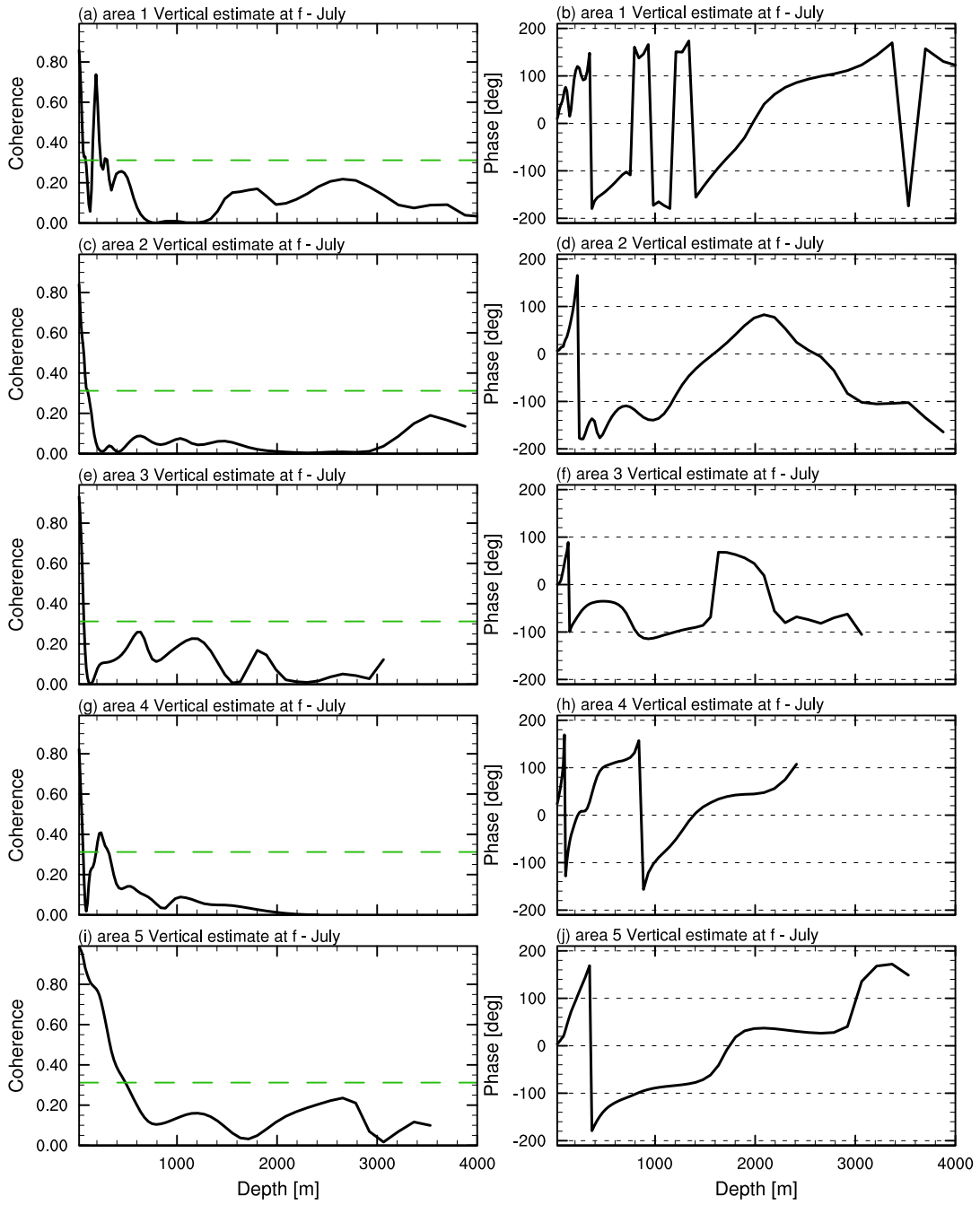

Figure 3.21: (Left panel:) Coherence between pairs of grid points (x_1 and x_2, where x_1 is always fixed point while x_2 moves downward) located at the center of each area from Figure 3.13a. Green line represents the critical value at 90% confidence level of zero coherency. (Right panel:) Phase between pairs of grid points at the center of each area. Coherence and phase are estimated at local inertial frequency f of grid point x_2. Figures show the results obtained for July.

ocean towards the ocean surface in vertical direction). Garrett (1999) defined frequency range of near-inertial waves between the local inertial frequency f and $1+\varepsilon f$, where ε is a constant for which we choose values of 0.1 and 1. We wish to repeat our calculation, but determining the coherence and phase at $1.1f$ and $2f$, with f being the local inertial frequency at x_2.

Figures 3.22 and 3.23 show the coherence (left panel) and phase (right panel) between pairs of increasingly separated grid points for January and July, respectively, calculated for pairs of grid

Table 3.7: Area name and vertical distance between two grid points x_1 and x_2 for which coherence is still above critical value. The distance is calculated by summation of all depths that correspond to grid points after which the coherence crosses critical value defined by 90% confidence level of zero coherency.

	Area	Distance in January [m]	Distance in July [m]
	area 1	82	82
	area 2	148	107
at the center:	area 3	826	60
	area 4	50	60
	area 5	408	492

points separated along one longitude as previously discussed. We use the longitudes noted in Table 3.5. Here, we look at waves propagating at near-inertial frequency by determining coherence and phase at frequency $1.1f$ of the moving point x_2 as a function of fixed point x_1. In parallel, we look at Figures 3.24 and 3.25 that show coherence (left panel) and phase (right panel) for January and July, respectively, but calculated at frequency $2f$ of the moving point x_2 as a function of fixed point x_1. Estimates obtained at $1.1f$ for both coherence and phase show similarities with the estimates obtained at f. One exception is evident though. The coherence scale (Table 3.8), defined by the point where the coherence first time passes the critical value represented by 90% confidence level of zero coherency, is higher in almost all cases except for area 5 (for January) where it becomes lower compared to the coherence scale estimated at f. Phase spectra calculated at $1.1f$ show similar behavior to one calculated at f, with the wave orientation towards the equator seen for all areas where the calculation is performed. Estimates obtained at $2f$ show differences not only in a coherence scale but also in the phase. Coherence scale, i.e., the distance at which waves are still correlated, is again higher than when the estimate is done at f (exception is area 5 where the coherence scale is lower). On the other hand, the phase show more rapid change of phase, meaning that waves at higher frequencies will have shorter wave lengths.

Figures 3.26 and 3.27 show the coherence (left panel) and phase (right panel) for January and July, respectively, calculated for pairs of grid points vertically separated along the central point of each area from Figure 3.12a, as previously discussed. We look at waves propagating at near-inertial frequency by determining coherence and phase at frequency $1.1f$ of the moving point x_2 as a function of fixed point x_1. In parallel, we look at Figures 3.28 and 3.29 that show coherence (left panel) and phase (right panel) for January and July, respectively, but calculated at frequency $2f$ of the fixed point x_1 as a function of moving point x_2. Estimates obtained at $1.1f$ for both coherence and phase show similarities with the estimates obtained at f. One exception is evident though. The coherence scale (Table 3.8) is higher in all cases. Phase calculated at $1.1f$ show similar behavior to ones calculated at f, with the wave orientation from the deep ocean towards its surface. Estimates obtained at $2f$ show differences not only in a coherence scale but also in the phase compared to calculations performed at f. Coherence scale is again higher. On the other hand, in most cases (except for area 5 in January, and area 3, area 4 and area 5 in July) the phase has initial shift up to about 200 to 400 m after which is almost constant with depth. This suggests that in the ocean interior near-inertial motions might be standing waves, but since coherence is no longer significant there, we can not make a correct estimate whether the motions are propagating or standing waves even though the phase indicates that they are standing waves.

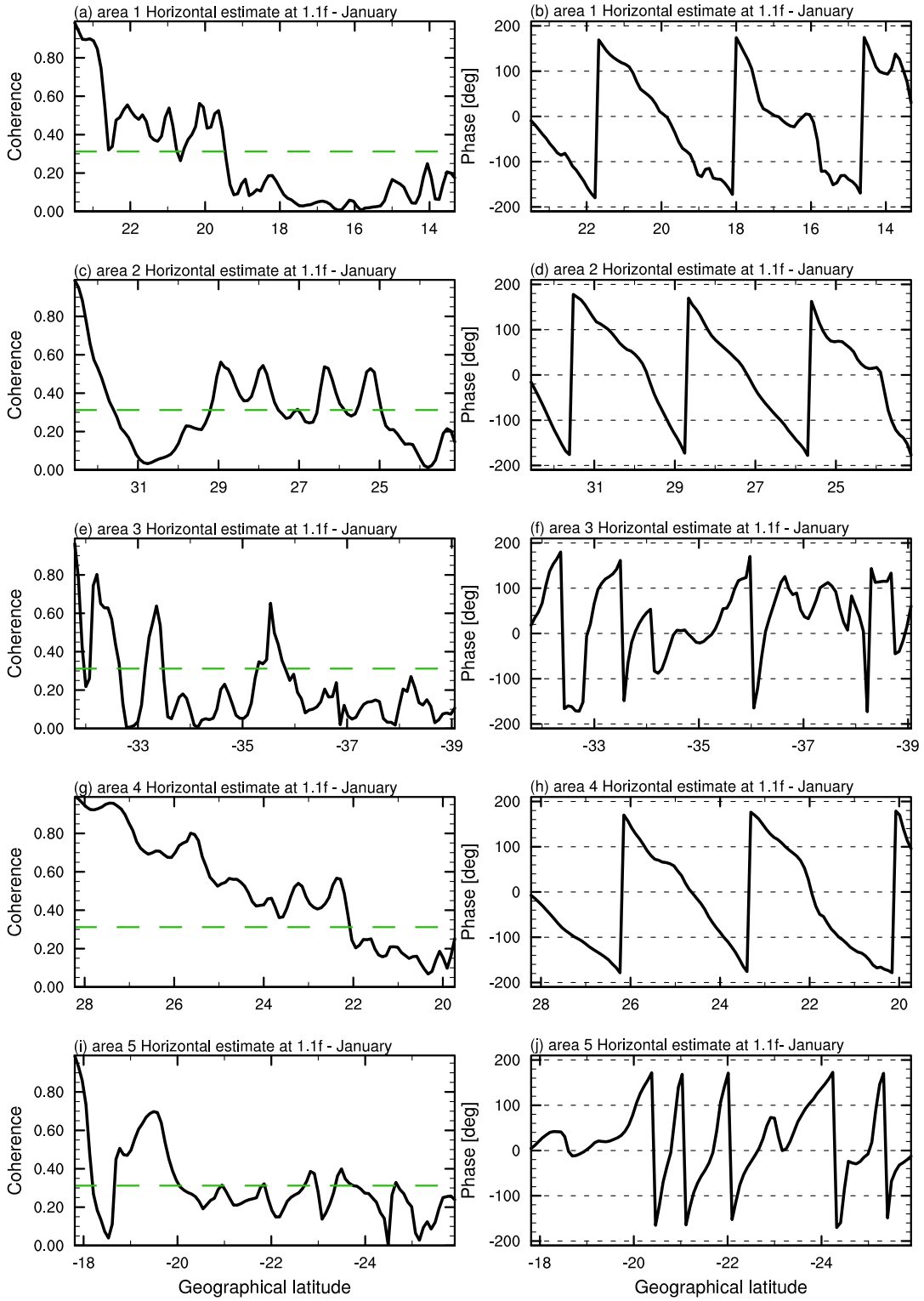

Figure 3.22: (Left panel:) Coherence between pairs of grid points (x_1 and x_2, where x_1 is always fixed point while x_2 moves southward) located along one longitude (Table 3.5) calculated using vertical velocity for each area in Figure 3.12a. Green line represents the critical value at 90% confidence level of zero coherency. (Right panel:) Phase between pairs of grid points located along one longitude calculated using vertical velocity for the same areas. Coherence and phase are estimated near the inertial frequency 1.1f of grid point x_2. Figures show the results obtained for January at 500 m.

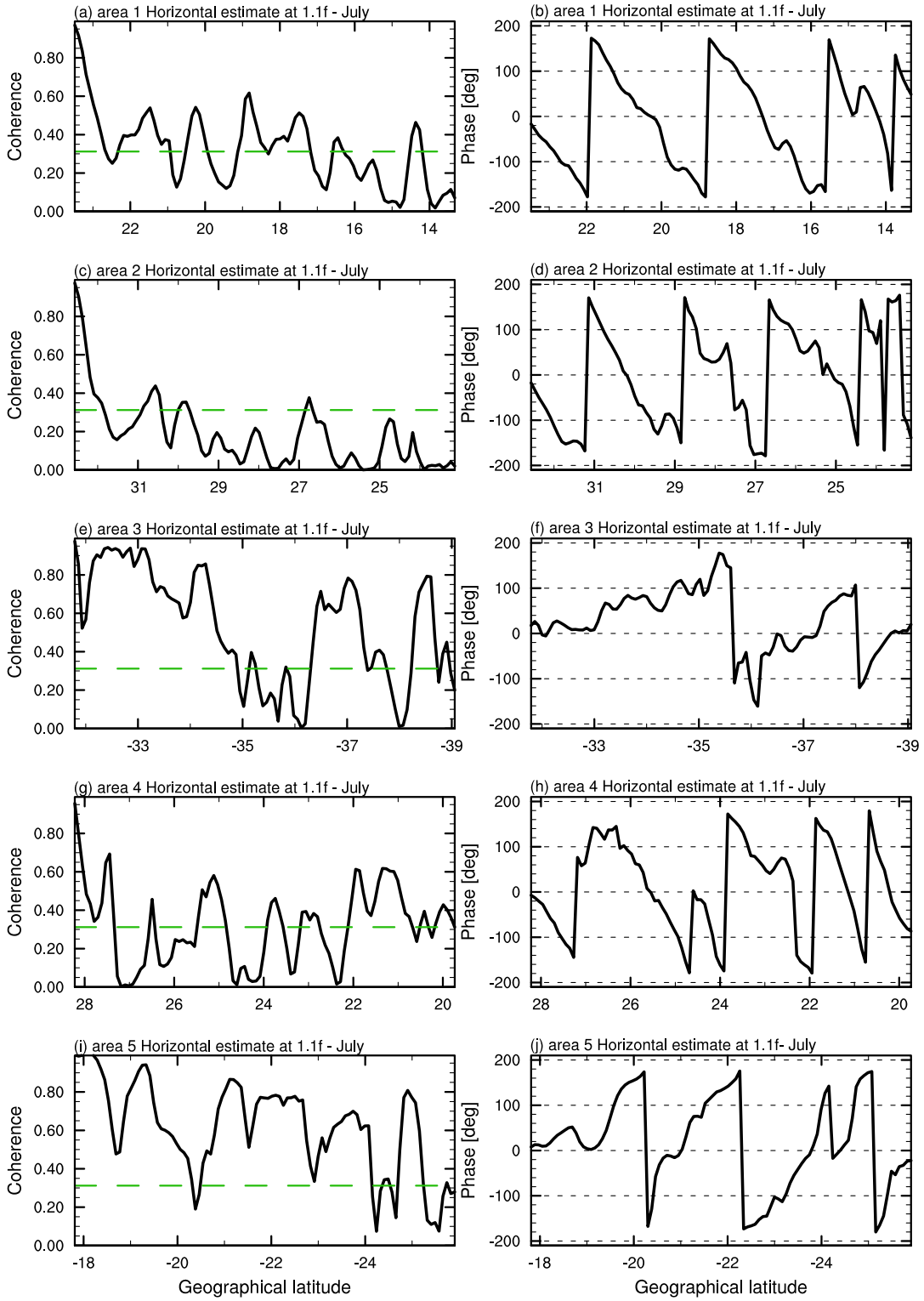

Figure 3.23: (Left panel:) Coherence between pairs of grid points (x_1 and x_2, where x_1 is always fixed point while x_2 moves southward) located along one longitude (Table 3.5) calculated using vertical velocity for each area in Figure 3.13a. Green line represents the critical value at 90% confidence level of zero coherency. (Right panel:) Phase between pairs of grid points located along one longitude calculated using vertical velocity for the same areas. Coherence and phase are estimated near the inertial frequency 1.1f of grid point x_2. Figures show the results obtained for July at 500 m.

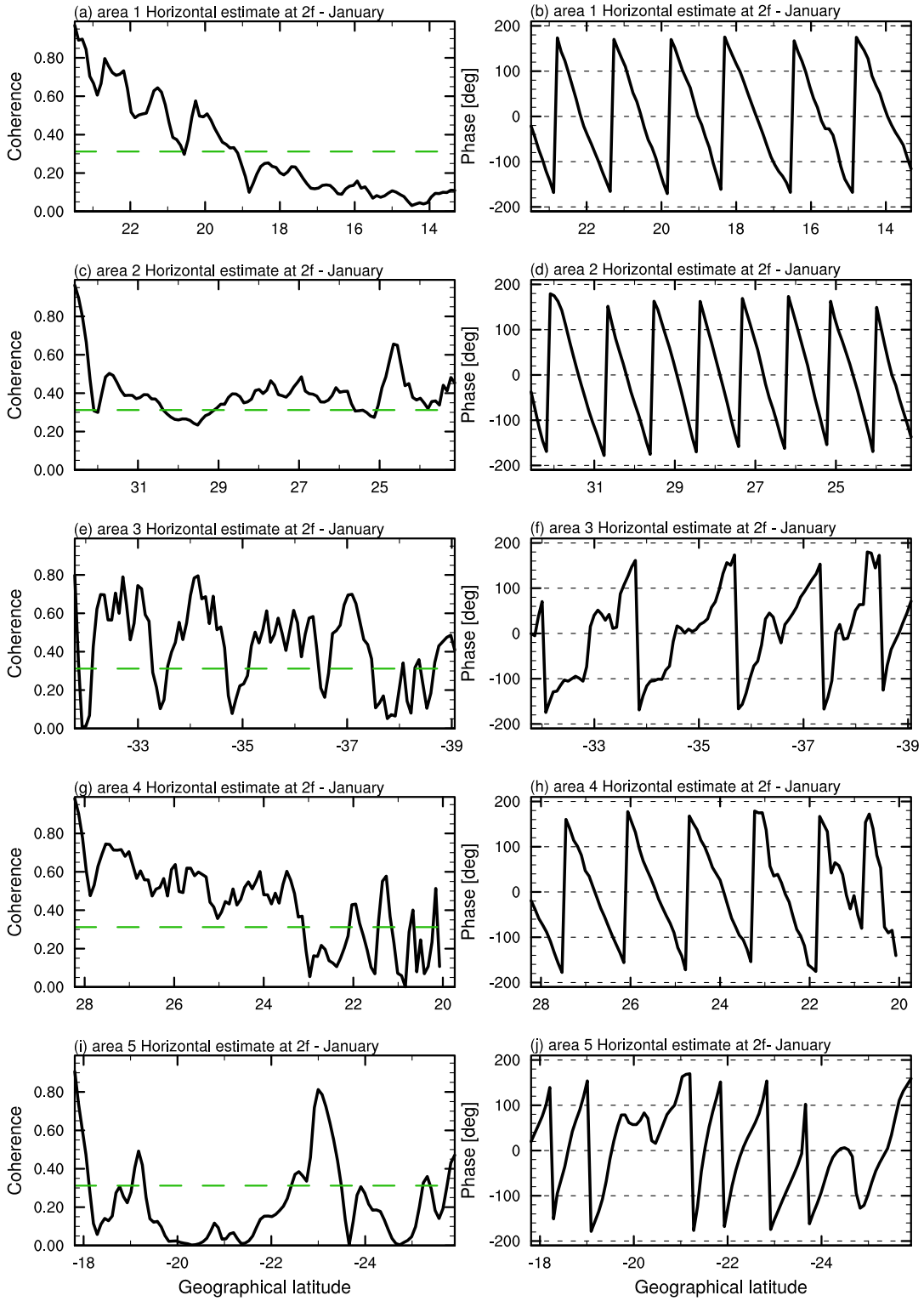

Figure 3.24: (Left panel:) Coherence between pairs of grid points (x_1 and x_2, where x_1 is always fixed point while x_2 moves southward) located along one longitude (Table 3.5) calculated using vertical velocity for each area in Figure 3.12a. Green line represents the critical value at 90% confidence level of zero coherency. (Right panel:) Phase between pairs of grid points located along one longitude calculated using vertical velocity for the same areas. Coherence and phase are estimated at double inertial frequency 2f of grid point x_2. Figures show the results obtained for January at 500 m.

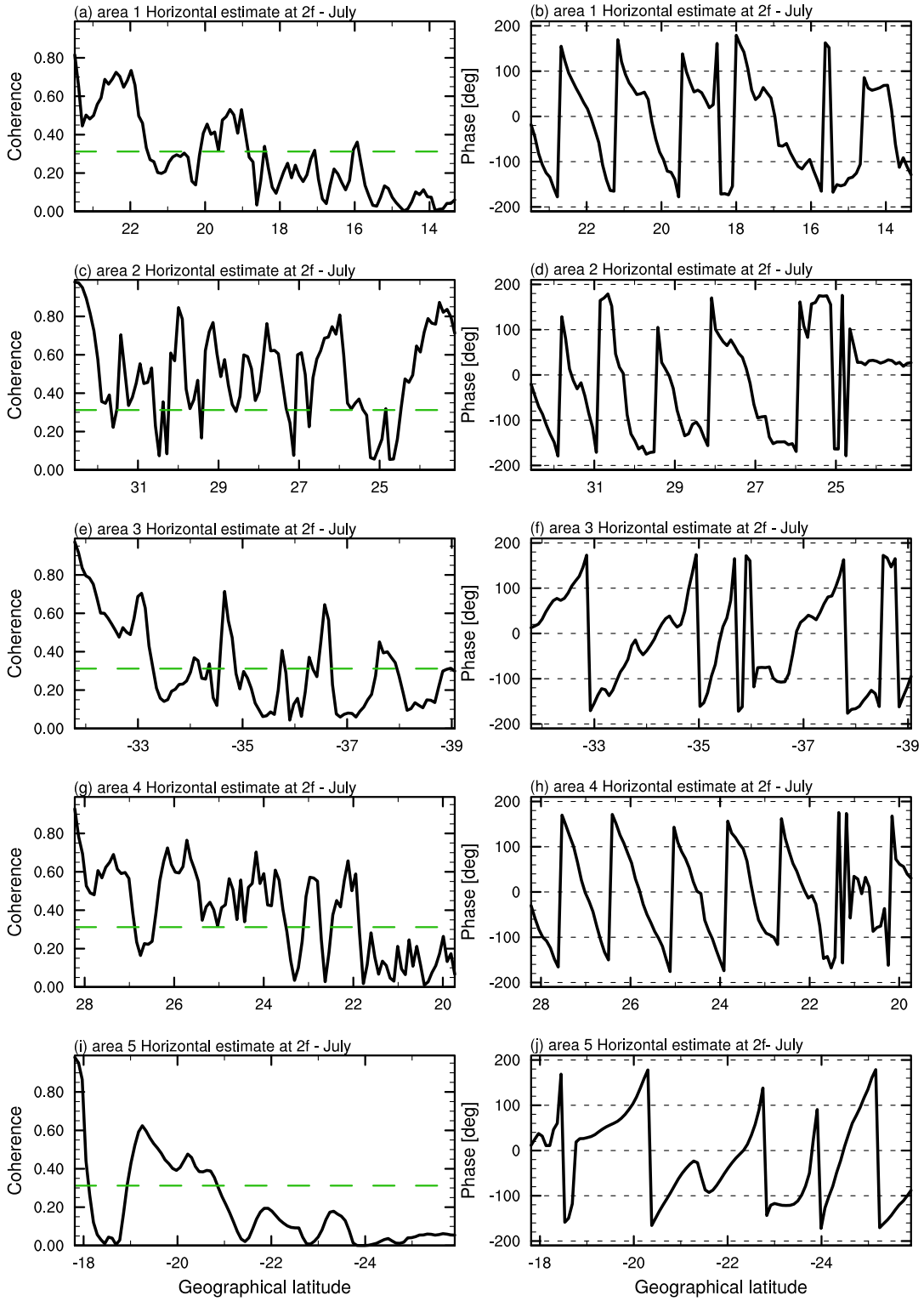

Figure 3.25: (Left panel:) Coherence between pairs of grid points (x_1 and x_2, where x_1 is always fixed point while x_2 moves southward) located along one longitude (Table 3.5) calculated using vertical velocity for each area in Figure 3.13a. Green line represents the critical value at 90% confidence level of zero coherency. (Right panel:) Phase between pairs of grid points located along one longitude calculated using vertical velocity for the same areas. Coherence and phase are estimated at double inertial frequency 2f of grid point x_2. Figures show the results obtained for July at 500 m.

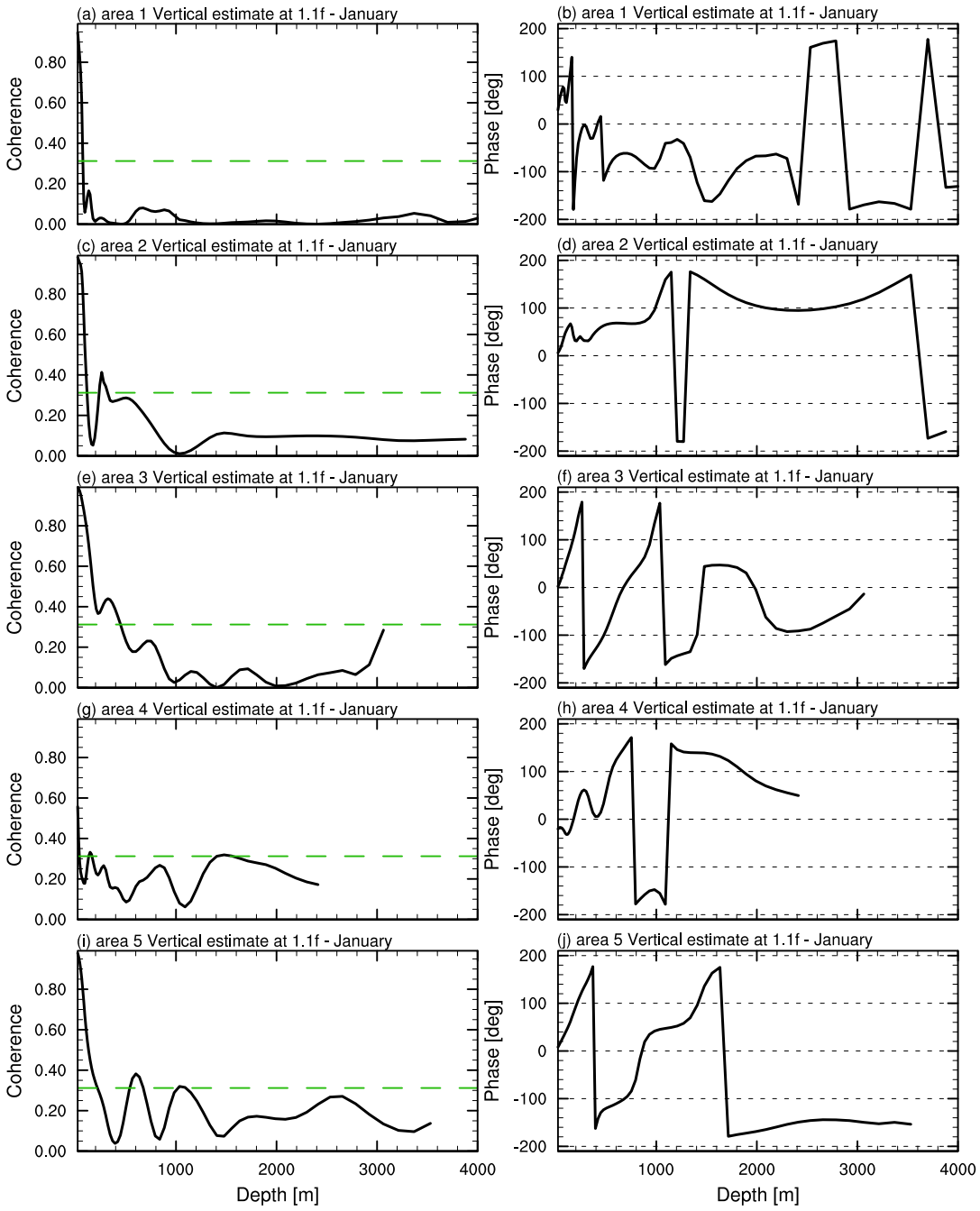

Figure 3.26: (Left panel:) Coherence between pairs of grid points (x_1 and x_2, where x_1 is always fixed point while x_2 moves downward) located at the center of each area from Figure 3.12a. Green line represents the critical value at 90% confidence level of zero coherency. (Right panel:) Phase between pairs of grid points at the center of each area. Coherence and phase are estimated at frequency 1.1f of grid point x_2. Figures show the results obtained for January.

3.5.5 Conclusions

In this subchapter we address the characteristic scales of near-inertial waves. The emphasis is on studying the near-inertial frequency band using vertical velocity simulated by a global ocean general circulation model at 1/10° horizontal resolution and with 80 vertical levels. Wavelength, inertial peak (its maximum and broadness), and coherence and phase for horizontally and vertically separated points are analyzed to study the variability and propagation of near-inertial waves.

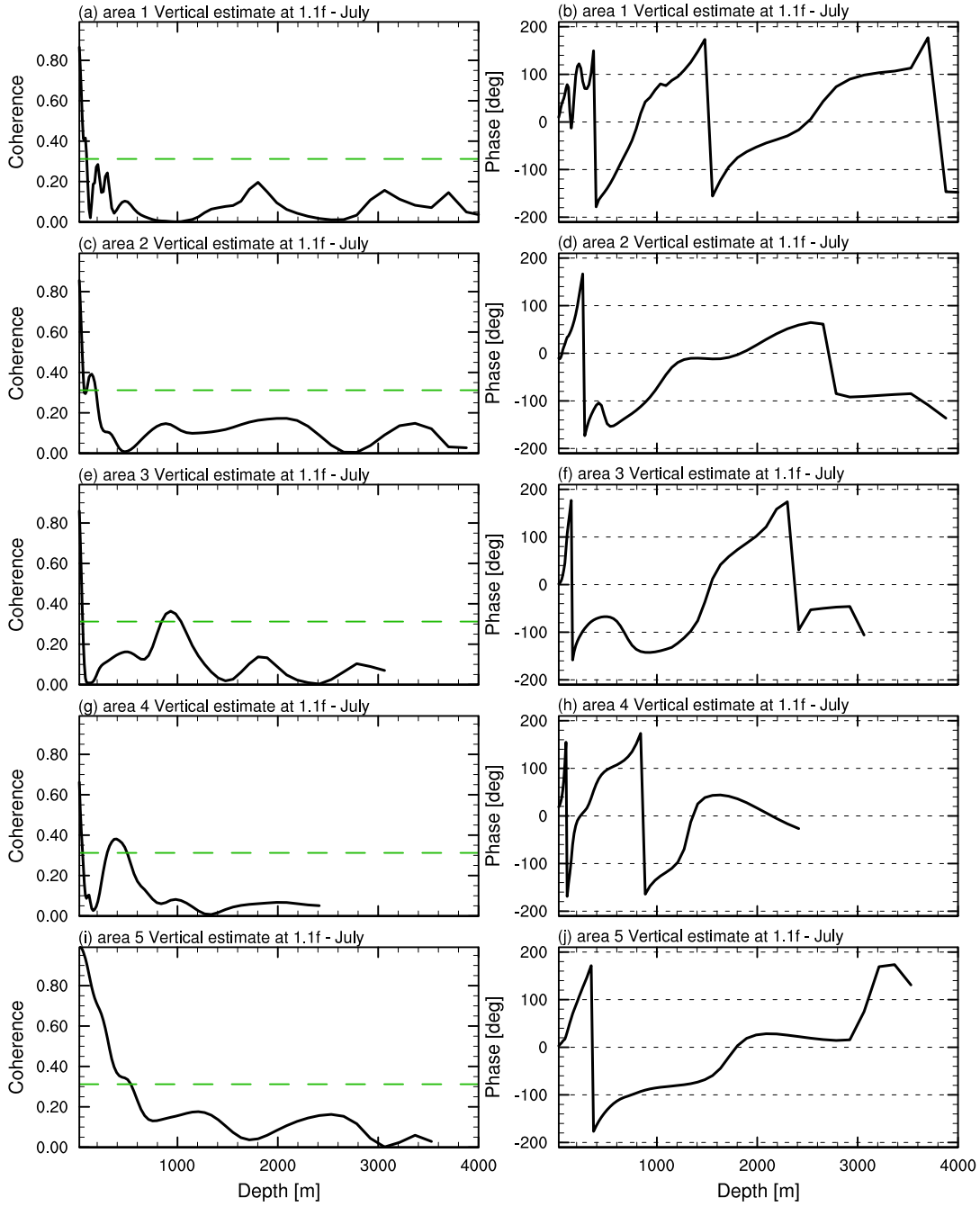

Figure 3.27: (Left panel:) Coherence between pairs of grid points (x_1 and x_2, where x_1 is always fixed point while x_2 moves downward) located at the center of each area from Figure 3.13a. Green line represents the critical value at 90% confidence level of zero coherency. (Right panel:) Phase between pairs of grid points at the center of each area. Coherence and phase are estimated at frequency 1.1f of grid point x_2. Figures show the results obtained for July.

Length and time scales of near-inertial waves are analyzed at two depths in the upper ocean, at 100 and 500 m, and for different areas highlighted in red in Figure 3.12a (for a closer look of the areas we refer the reader to Figure 3.14).

First, we address horizontal length scales of near-inertial waves. There is no clearly defined wavelength, and only the spectral peak for area 1 and area 2 in January has a clear maximum. Wavelengths become clearer when the spectra of zonal and meridional wavenumbers are con-

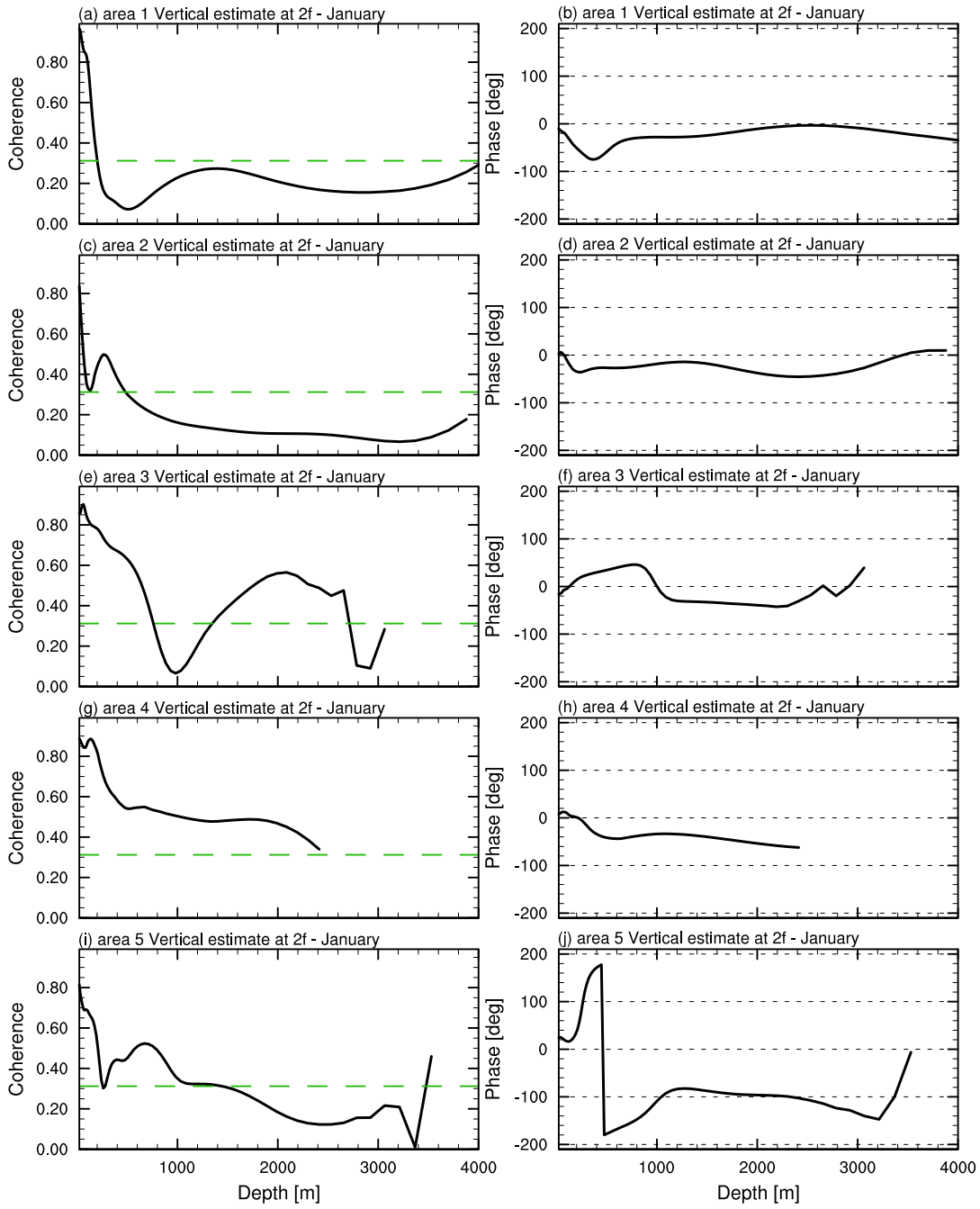

Figure 3.28: (Left panel:) Coherence between pairs of grid points (x_1 and x_2, where x_1 is always fixed point while x_2 moves downward) located at the center of each area from Figure 3.12a. Green line represents the critical value at 90% confidence level of zero coherency. (Right panel:) Phase between pairs of grid points at the center of each area. Coherence and phase are estimated at double inertial frequency 2f of grid point x_2. Figures show the results obtained for January.

sidered separately. Based on clearly defined spectral peak (and maximum) only for meridional wavenumbers, we conclude that near-inertial waves move for all areas mainly in the meridional direction. We find that there is a marked anisotrophy between zonal (east-west) and meridional (north-south) wavenumber spectra (Figure 3.15 and 3.16).

Second, in this section we further quantify time scales of near-inertial waves. In other words, we examine spectral peak, mainly its maximum and broadness, around the local inertial frequency

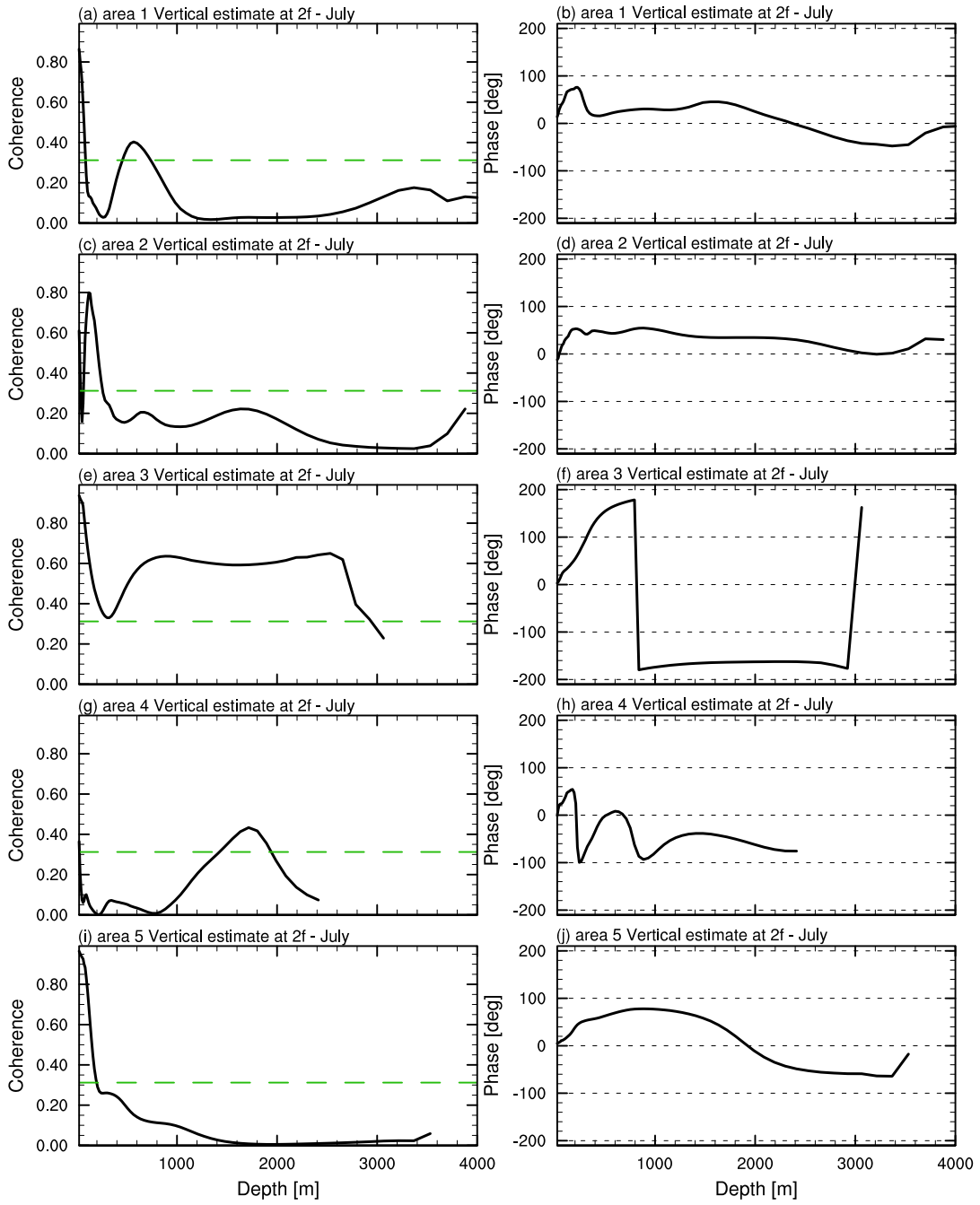

Figure 3.29: (Left panel:) Coherence between pairs of grid points (x_1 and x_2, where x_1 is always fixed point while x_2 moves downward) located at the center of each area from Figure 3.13a. Green line represents the critical value at 90% confidence level of zero coherency. (Right panel:) Phase between pairs of grid points at the center of each area. Coherence and phase are estimated at double inertial frequency $2f$ of grid point x_2. Figures show the results obtained for July.

f and around the double frequency $2f$ by calculating frequency spectrum of vertical velocity at 100 and 500 m. Spectral peaks show strong maximum around f and weaker maximum around $2f$ (except for area 4 in January and area 2 at 100 m in July). This suggests that for our selected regions, near-inertial waves are dominant waves at frequencies ranging from about $0.9f$ to $2.1f$. Spectral shape between f and $2f$ differs between all areas and a universal shape is not evident. Spectra calculated for area 1 and area 2 (centered around 14.34° N and 17.98° N) have broader

Table 3.8: Area name and horizontal and vertical distance between two grid points x_1 and x_2 for which coherence is still above critical value. The horizontal distance is calculated by multiplying number of grid points after which the coherence crosses critical value defined by 90% confidence level of zero coherency and the approximate grid distance in meridional direction of 10 km. The vertical distance s calculated by summation of all depths that correspond to grid points after which the coherence crosses critical value defined by 90% confidence level of zero coherency. Horizontal distance is given in [km] while vertical in [m].

	Area	Distance in January at $1.1f$ [km]	Distance in July at $1.1f$ [km]
horizontal:	area 1	280	90
	area 2	110	80
	area 3	30	440
	area 4	710	120
	area 5	50	320
		Distance in January at $2f$ [km]	Distance in July at $2f$ [km]
horizontal:	area 1	250	200
	area 2	50	100
	area 3	30	220
	area 4	600	160
	area 5	40	40
		Distance in January at $1.1f$ [m]	Distance in July at $1.1f$ [m]
vertical:	area 1	71	94
	area 2	107	60
	area 3	215	50
	area 4	30	50
	area 5	212	28
		Distance in January at $2f$ [m]	Distance in July at $2f$ [m]
vertical:	area 1	195	82
	area 2	120	30
	area 3	782	3052
	area 4	2520	20
	area 5	249	195

peak with slightly notable maximum compared to maxima when the calculation is done for other areas. Also, maxima do not occur at f but at higher frequencies, and the shift of the maxima is more pronounced for calculation at 500 than at 100 m. Spectral peaks become narrower and maxima at f become higher as areas used for calculation are further from the equator. At the same time, frequency shift becomes less pronounced. This suggests that spectra calculated for areas closer to the equator and at higher depth are more influenced by waves propagating from higher latitudes.

Finally, we address coherence and phase of a variable at two positions, x_1 and x_2, to describe correlation between waves at two points and their propagation in space. Coherence and phase are calculated for pairs of meridionally or vertically separated grid points such that one of the points, x_1, is always fixed while the other, x_2, moves southward in meridional or to greater depth in vertical direction. We look at waves propagating at several frequencies (the local inertial frequency f, the double inertial frequency $2f$, and at $1.1f$ of the moving point x_2). Coherence and phase calculated at f between horizontally separated grid points show correlation scale of about 110 to 240 km for

areas with strong wavy structures spanning through all latitudes (e.g., area 2 area 4 and area 5 in January, and area 3 and area 5 in July.) For other areas, namely area 3 in January and area 2 in July, coherence scale is about 20 to 30 km. There, wave structures are not so clearly defined, and a closer look at Figure 3.14 reveals small spatial structures with rapidly changing signs that might have an influence on the wave correlation. Phase calculated at f indicates that our simulated near-inertial motions are waves that propagate equatorward. Coherence and phase calculated at $1.1f$ and $2f$ between two horizontally separated points show similarities with the coherence and phase calculated at f. Two differences are evident. First, coherence scale increases for all areas except for area 5 where it decreases, and second, phase shows more rapid phase change when calculated at $2f$ indicating that waves at higher frequencies have shorter wavelength. Coherence calculated at f between two vertically separated points yield coherence scale of more than 60 m for all areas, with extreme values of 500 to 800 m in area 3 in January and area 5 in July. Phase calculated at f indicates that near-inertial motions are propagating waves with an upward direction, meaning that waves are propagating from the ocean interior towards its surface. Coherence and phase between both horizontally and vertically separated points calculated at $1.1f$ and $2f$ show similarities with the coherence and phase calculated at f. Two differences are evident though. First, coherence scale calculated at $1.1f$ and $2f$ is somewhat higher or the same order of magnitude for all areas except area 5 where it becomes lower. Second, phase calculated at $2f$ suggest that simulated near-inertial motions might be standing waves in area 1, area 2 and area 4 in January, and area 1 and area 2 in July. On the other hand, since coherence in the deep ocean is no longer significant under 90% confidence level of zero coherency test, we can not make a correct estimate whether the motions are propagating or standing waves even though the phase indicates that they are standing waves.

Our estimates of coherence and phase can be connected to previous analyses of near-inertial energy flux in horizontal as well as in vertical direction. Here we look at a group velocity of near-inertial waves, which is directed in the direction of near-inertial wave energy flux, compared to phase velocity of these waves. In general, in horizontal direction a group velocity is oriented in the direction as the phase velocity (Olbers et al., 2012). This would indicate that equatorward near-inertial wave propagation implies equatorward near-inertial energy propagation. In contrast to horizontal propagation, in vertical direction a group velocity is oriented in opposite direction compared to phase velocity (Olbers et al., 2012). This indicates that upward wave propagation leads to downward energy propagation. This conclusion is consistent with the one obtained in Chapter 3.4.

4

Influence of the mesoscale eddies on near-inertial motions

To evaluate the possible influence of mesoscale eddies on wind-induced near-inertial waves in the ocean, we compare experiments performed with the Max Planck Institute Ocean Model (MPIOM) at two different resolutions: one at 1/10° resolution, an experiment in which a significant bulk of mesoscale eddies is simulated, and the other at 0.4° resolution, an experiment which hardly resolves eddies. The model is forced by National Centers for Environmental Prediction (NCEP) reanalysis data (approximately 1.875° horizontal and 6-hourly temporal resolution). Given the length scales of the near-inertial waves of about 200 to 500 km, we expect that the long near-inertial waves simulated by the 1/10° model are, by and large, simulated by the 0.4° model, so that a comparison can indicate the influence of eddies on the simulated waves. Despite the differences in horizontal resolution used in the experiments, the spatial distributions of the near-inertial kinetic energy near the ocean surface and the total wind power input to near-inertial motions at the surface show similarities likely related to the large scale patterns of wind stress variability connected to mid-latitude storms. A change from the 0.4° experiment that hardly resolves eddies to the 1/10° experiment with strong eddy activity results in a threefold increase in the near-inertial kinetic energy in the ocean interior. Vertical transects reveal high levels of near-inertial kinetic energy leaking into the deep ocean in the experiment with eddies. The strong sensitivity of the near-inertial kinetic energy to the presence of mesoscale eddies points to a possibility that the presence of mesoscale eddies plays a crucial role for vertical penetration of near-inertial waves.

4.1 Introduction

Near-inertial waves are believed to be an important source for mixing in the interior of the ocean (Munk and Wunsch, 1998, Wunsch and Ferrari, 2004). They are mostly forced by intermittent atmospheric storms that have scales of the order of 1000 km. However, since Weller (1982), it has been reported that the presence of mesoscale eddies can influence and distort near-inertial

wave structure and decrease the length scale of near-inertial waves down to values smaller than 100 km (Klein et al., 2004b, Danioux et al., 2011). Observational estimates (e.g., Alford et al., 2012) as well as model studies (e.g., Zhai et al., 2005) show that there is a remarkable coincidence between regions with strong mesoscale variability (storm track regions) in both the atmosphere and in the ocean (Zhai et al., 2005). In Figure 2.13 and 2.11b we showed a spatial distribution of the wind-power input to surface near-inertial motions and a spatial distribution of the near-inertial kinetic energy at the first model level, respectively. The figures indicate that regions with a strong wind-power input to the ocean at near-inertial frequencies are also the regions with strong eddy activity. The question that arises is whether and how presence of the eddies influences propagation of near-inertial waves.

Energy of the near-inertial waves in the ocean is redistributed by the β-dispersion effect (Anderson and Gill, 1979) where near-inertial waves are free to propagate equatorward, but are restricted in their poleward propagation. In the vertical direction, the relative vorticity can influence the near-inertial energy propagation (see Figure 3.5) and the decay of the near-inertial energy in the mixed layer. Zhai et al. (2005, 2007) showed that near-inertial energy can be trapped in regions of anticyclonic relative vorticity where the important role is played by anticyclonic eddies for draining near-inertial energy from the surface to the deep ocean through the "internal chimney" effect. Previous studies thus indicate the important role played by mesoscale eddies on the distribution of the near-inertial kinetic energy, but so far limited attempts have been made to quantify the essential differences between the results of the near-inertial waves simulated with ocean models at high horizontal resolutions (e.g., 1/10°, in which significant bulk of eddies is resolved) and at low or medium horizontal resolutions (e.g., 0.4°, in which eddies are only parametrized).

In Section 3.4 we showed the influence of the model resolution on the wind-power input to near-inertial motions at the ocean surface. In our analysis, wind-power input to near-inertial motions in the 1/10° model is 0.34 TW, which is slightly lower than 0.37 TW in the 0.4° model. This results suggest that the higher resolution of the ocean model does not significantly change the wind-power input. On the other hand, Zhai et al. (2005) studied the change of the vertical propagation of storm-induced near-inertial energy with a simplified eddying ocean channel model. To make a difference between the ocean model with eddies and without eddies, they applied the storm forcing to the zonal wind stress (ocean influenced by eddies) or they applied the storm forcing at the resting ocean (ocean without the influence of eddies). They showed that the leakage of near-inertial energy out of the surface layer is strongly enhanced by the presence of eddies, with the anticyclonic eddies acting as a conduit to the deep ocean.

The previous studies thus indicate the importance of mesoscale eddies in near-inertial energy propagation particularly in the vertical direction such that they influence pathways by which near-inertial energy enters the ocean and is ultimately available for deep-ocean mixing. However, the direct comparison between the near-inertial energy obtained from two different model resolutions but forced under the same physical conditions has not been made so far. The ocean model used in this chapter is the Max Planck Institute Ocean Model (MPIOM; Marsland et al., 2003). The experiments are performed with model configured at 1/10° (experiment with eddies) and 0.4° (experiment without eddies) horizontal resolution (von Storch et al., 2012, Jungclaus et al., 2013). The model is forced by the surface fluxes of heat, fresh water and momentum from the National Centers for Environmental Prediction (NCEP) reanalysis (Kalnay et al., 1996) at approximately 1.875° horizontal and 6-hourly temporal resolution. In this chapter we address

the following questions: How is the vertical velocity spectra represented in two different model set-ups? How does the presence of mesoscale eddies influence the near-inertial kinetic energy in the ocean?

4.2 Results

4.2.1 Impact of a model resolution on the velocity spectra at different levels in the ocean

The frequency spectra at three different depths are calculated from the simulated vertical velocity of the experiment with eddies (with 1/10° model) and without eddies (with 0.4° model). We compute the spectra for several neighboring grid points taken from the center of area 3 introduced in Section 3.5.2, and the result is presented as their mean value. The resulting spectra are depicted in Figure 4.1 for January (top) and for July (bottom). Thick lines represent the spectra from the experiment with eddies and thin lines represent the experiment without eddies. We show the spectra calculated at 100 m (black line), 500 m (blue line) and 1700 m (red line). The green dashed lines represent the local inertial frequency f, the double inertial frequency $2f$ and the triple inertial frequency $3f$. Frequency spectra have similar shape around f. The energy starts to increase at frequencies slightly below f and it shows the conspicuous inertial maximum in the vicinity of f. The energy then decreases in the frequency domain of the internal waves (frequencies higher than f).

In general, spectra at two different model resolutions, with eddies and without eddies, show similar shapes for all depths. Some differences are evident though. First, energy levels centered around f for spectra in the experiment without eddies are more than 95% smaller when calculated for January (energy at 100 m for experiment with eddies is $7.96{\cdot}10^{-8}$ $m^2/s^2/h$ while for the experiment without eddies is $0.29{\cdot}10^{-8}$ $m^2/s^2/h$) and 88% smaller when calculated for July (energy at 100 m for experiment with eddies is $4.3{\cdot}10^{-7}$ $m^2/s^2/h$ while for the experiment without eddies is $0.51{\cdot}10^{-7}$ $m^2/s^2/h$) compared to energy levels calculated in the experiment with eddies. Second, the depth dependence of spectral peaks in experiment with eddies is different from the experiment without eddies. Energy at f decreases with depth for the experiment without eddies, while it is almost constant for the experiment with eddies. Furthermore, the peak at $2f$ in experiment with eddies strengthens with increasing depth. Third, spectral peaks at frequencies of multiple f are much more pronounced in the experiment with eddies than without eddies. Finally, there is a shift of spectral peak at f towards higher frequencies in the experiment with eddies. Such a shift is also notable for the peaks at $2f$. This spectral shift is obvious for the experiment with eddies at all depths. As stated in previous chapter (see Section 3.5.3) local inertial frequency can be shifted to higher values due to interaction of locally generated waves with mesoscale flows or due to interaction with waves propagating from higher latitudes. Here, the results indicate that mesoscale flows influence frequency spectra in the experiment with eddies.

4.2.2 Near-inertial kinetic energy at the surface and in the interior of the ocean

Near-inertial kinetic energy is estimated as the variance of the anticyclonically rotating velocity vector at frequencies ω defined as: $0.7f < \omega < 1.3f$, where f denotes the local inertial frequency. We choose this frequency range to be consistent with the analysis of the previous two chapters.

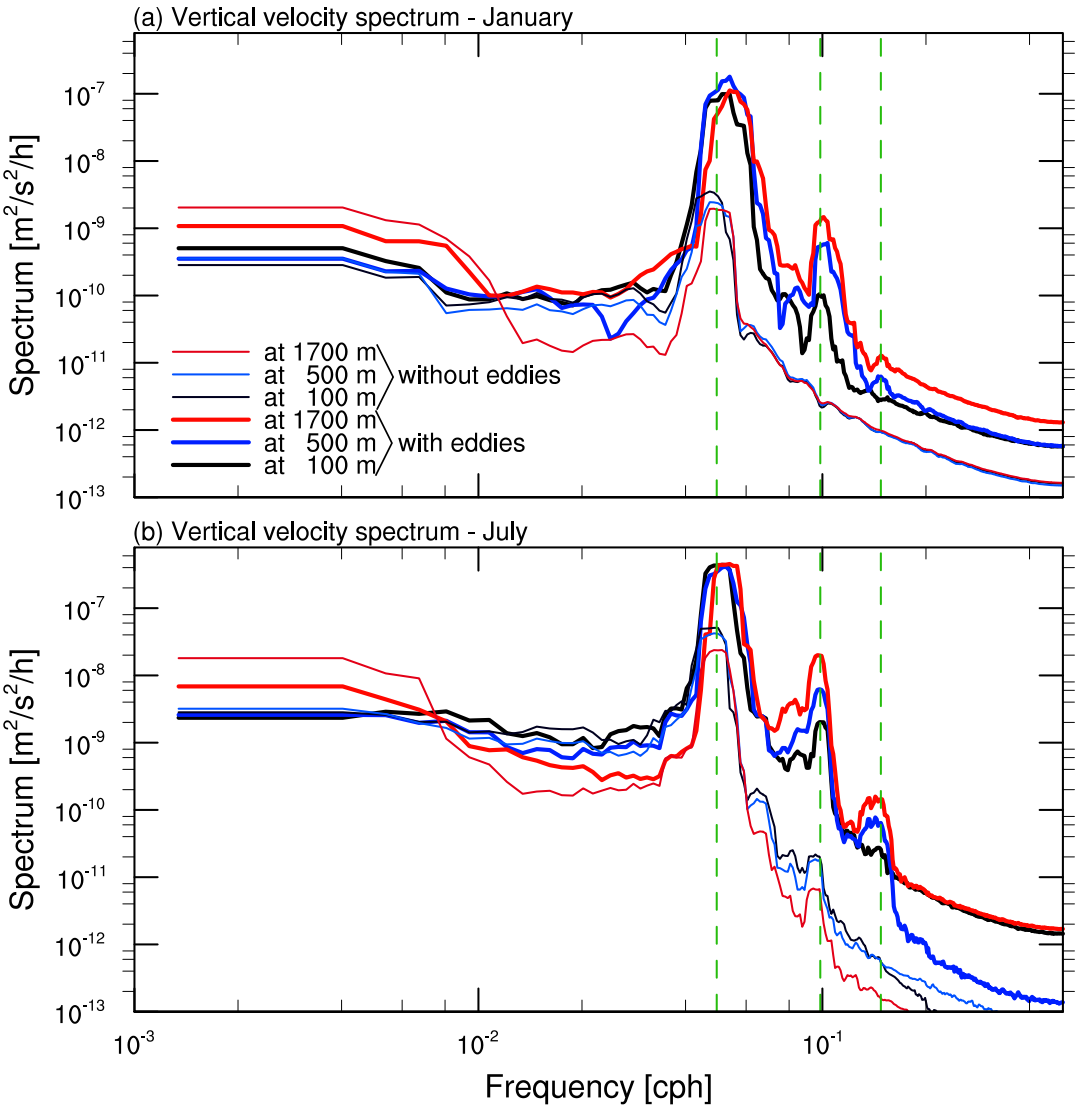

Figure 4.1: Frequency spectra calculated using vertical velocities for area 3 depicted in Figure 3.12a at depths of 100 m (black), 500 m (blue) and 1700 m (red) for January (top) and July (bottom). Thick lines represent spectra calculated using vertical velocity from 1/10° model (with eddies) and thin lines represent the velocity from 0.4° model (without eddies). Green line depicts the local inertial frequency f, the double inertial frequency 2f and the triple inertial frequency 3f.

The calculations are done for January and July 2005 separately, and their mean value at 6 m is presented in Figure 4.2 and at 100 m in Figure 4.3.

Near-inertial kinetic energy at 6 m for the experiment without and with eddies (Figure 4.2a and 4.2b respectively) shows a pronounced maximum around 30°-50° in the mid-latitude storm track regions, consistent with Rimac et al. (2013, references therein; see Chapter 2). At 100 m (Figure 4.3a and 4.3b) the spatial distribution of the near-inertial kinetic energy is different, with a pronounced maximum in the mid-latitude storm track regions seen only in the experiment with eddies. Furthermore, the spatial structure is similar in both model resolutions but the experiment with eddies reveals small scale structures which are not seen in the experiment without eddies where the spatial structure is smooth. Zonal mean of the near-inertial kinetic energy calculated at 6 m (Figure 4.2c and 4.2d) show a pronounced maximum around 30°-40° N and 30°-50° S for experiment with eddies and experiment without eddies, but the highest value is found at 30° N.

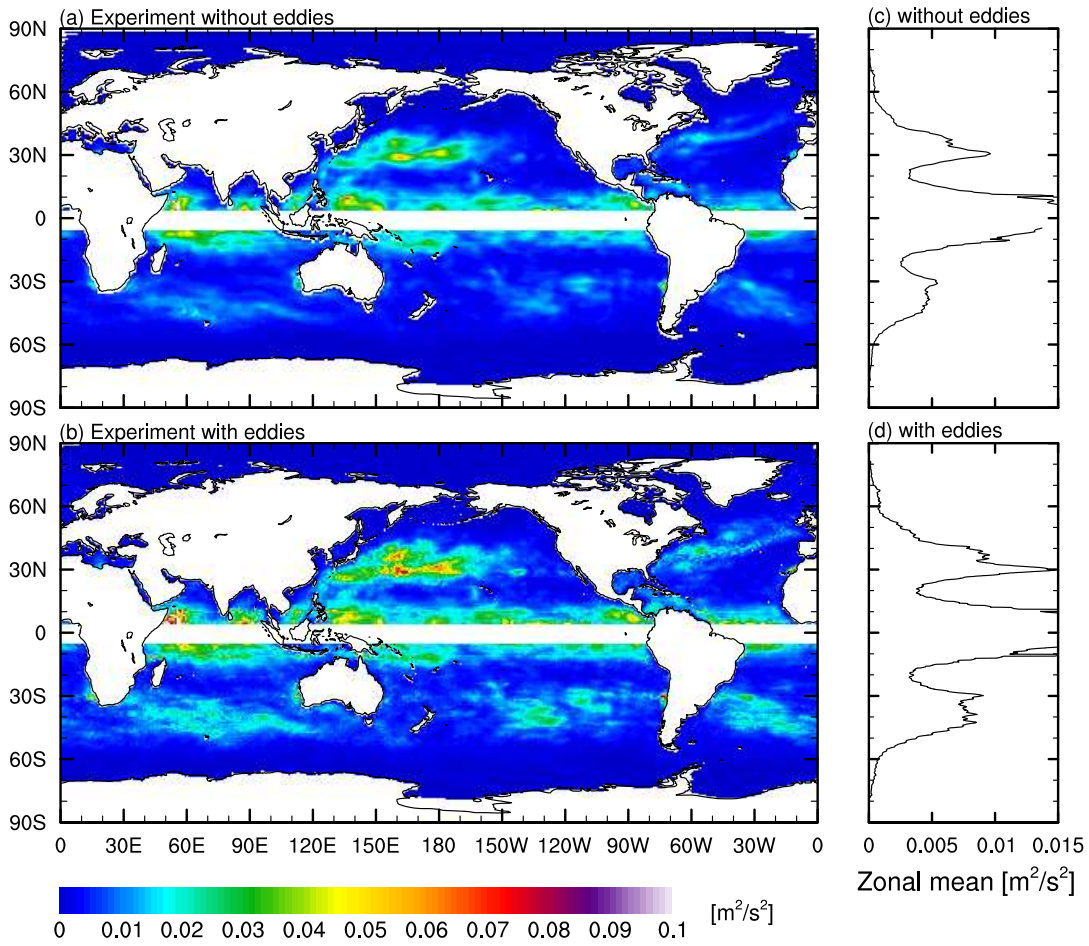

Figure 4.2: Spatial distribution of the near-inertial kinetic energy calculated from the bandpass-filtered model velocities taken from the experiment (a) without eddies and (b) with eddies. Zonal mean of the near-inertial kinetic energy taken from the experiment (c) without eddies and (d) with eddies. Energy is calculated as a mean value between January and July 2005 and it is presented at 6 m depth in [m^2/s^2].

The maxima in both hemispheres are higher for the experiment with eddies. For zonal mean at 100 m (Figure 4.3c and 4.3d), the experiment with eddies shows much larger maxima around 20°-40° N and at 30° S than the experiment without eddies does.

Near-inertial kinetic energy increases when using an ocean model at higher horizontal resolution especially in the deeper ocean. The globally averaged near-inertial kinetic energy at 6 m is $5.6{\cdot}10^{-3}\,m^2/s^2$ in the experiment without eddies and it is $6.4{\cdot}10^{-3}\,m^2/s^2$ in the experiment with eddies. At 100 m, the globally averaged value increases from $0.1{\cdot}10^{-3}\,m^2/s^2$ to $0.4{\cdot}10^{-3}\,m^2/s^2$ with the increasing model resolution.

In Figure 4.3 it is shown that in the presence of mesoscale eddies near-inertial kinetic energy reveals small-scale patchy structures. To illustrate this feature more closely, we present the spatial distribution of the near-inertial kinetic energy for both experiments for a small region in the North Atlantic (Figure 4.4). Spatial distribution of the near-inertial kinetic energy has a maximum over the Grand Banks of Newfoundland for both experiments. By contrast to the experiment without eddies where this maximum is given by a smooth structure (Figure 4.4a), in the experiment with eddies much smaller spatial scales can be seen (Figure 4.4b), reflecting the mesoscale eddy field. Klein et al. (2004b) argued that the influence of mesoscale eddies can regulate the spatial dis-

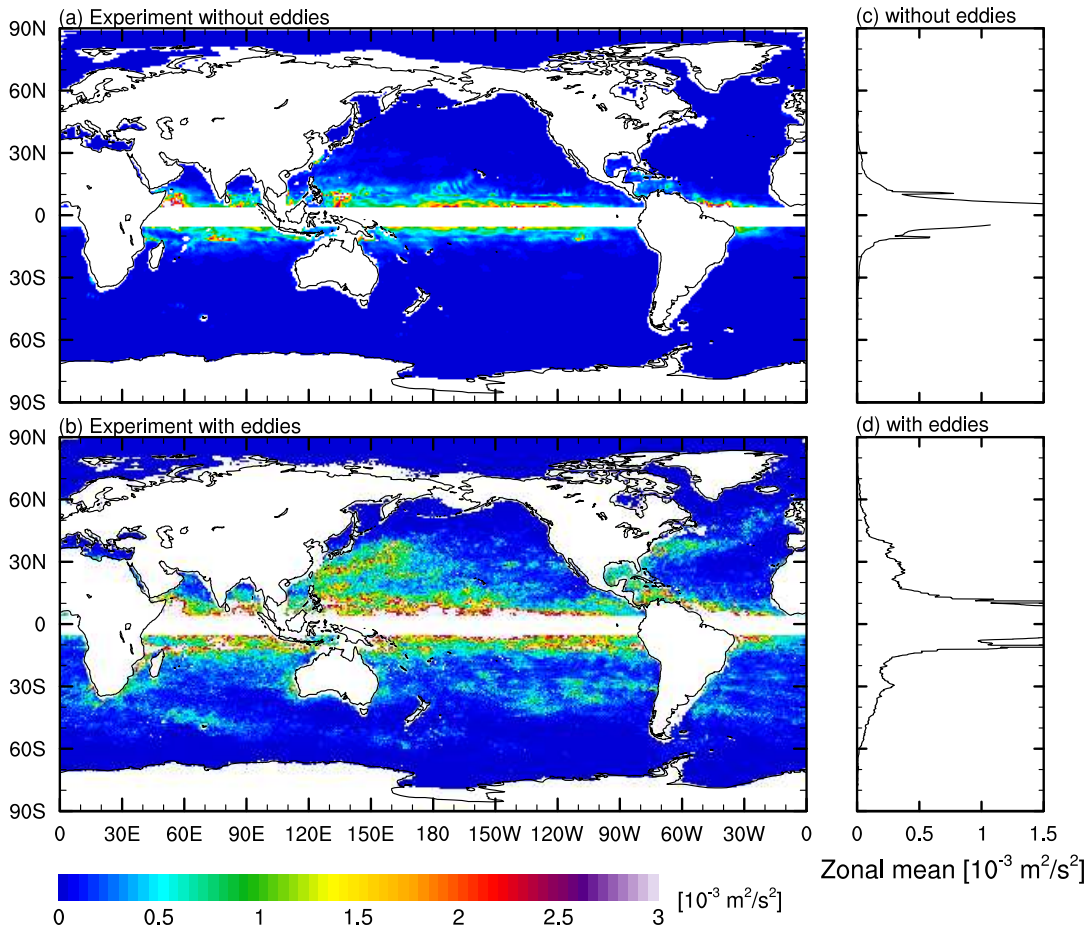

Figure 4.3: Spatial distribution of the near-inertial kinetic energy calculated from the bandpass-filtered model velocities taken from the experiment (a) without eddies and (b) with eddies. Zonal mean of the near-inertial kinetic energy taken from the experiment (c) without eddies and (d) with eddies. Energy is calculated as a mean value between January and July 2005 and it is presented at 100 m depth in [10^{-3} m^2/s^2].

tribution of the near-inertial kinetic energy by lowering its spatial scales compared to the spatial scales of the wind forcing. Vertical transects (Figure 4.4c and 4.4d) reveal a similar picture for both experiments characterized by a relatively high levels of near-inertial kinetic energy in the upper 40 m. Deeper inside significant near-inertial kinetic energy is confined in "chimneys" in the experiment with eddies reflecting the pattern of the eddy field. These patterns are not seen in the experiment without eddies where we can see much weaker and more diffuse downward spreading of the near-inertial kinetic energy. Therefore, the vertical transects indicate a much more efficient transfer of the near-inertial kinetic energy to a greater depth when there are eddies than when there are no eddies.

From the vertical cross-section of near-inertial kinetic energy we could see that in general energy decreases with depth, but there are also high levels of near-inertial kinetic energy in the first 50-200 m in the ocean. To further address the question of how the near-inertial kinetic energy changes with depth, we look at the specific regions in the ocean defined by distinctly different mixed layer depth (e.g., see Figure 3.3a). Figure 4.5 illustrates the vertical profiles of near-inertial kinetic energy averaged over the areas highlighted in Figure 3.3a for January (and in Figure 3.4a for July). Solid lines represent the experiment with eddies while dashed lines represent

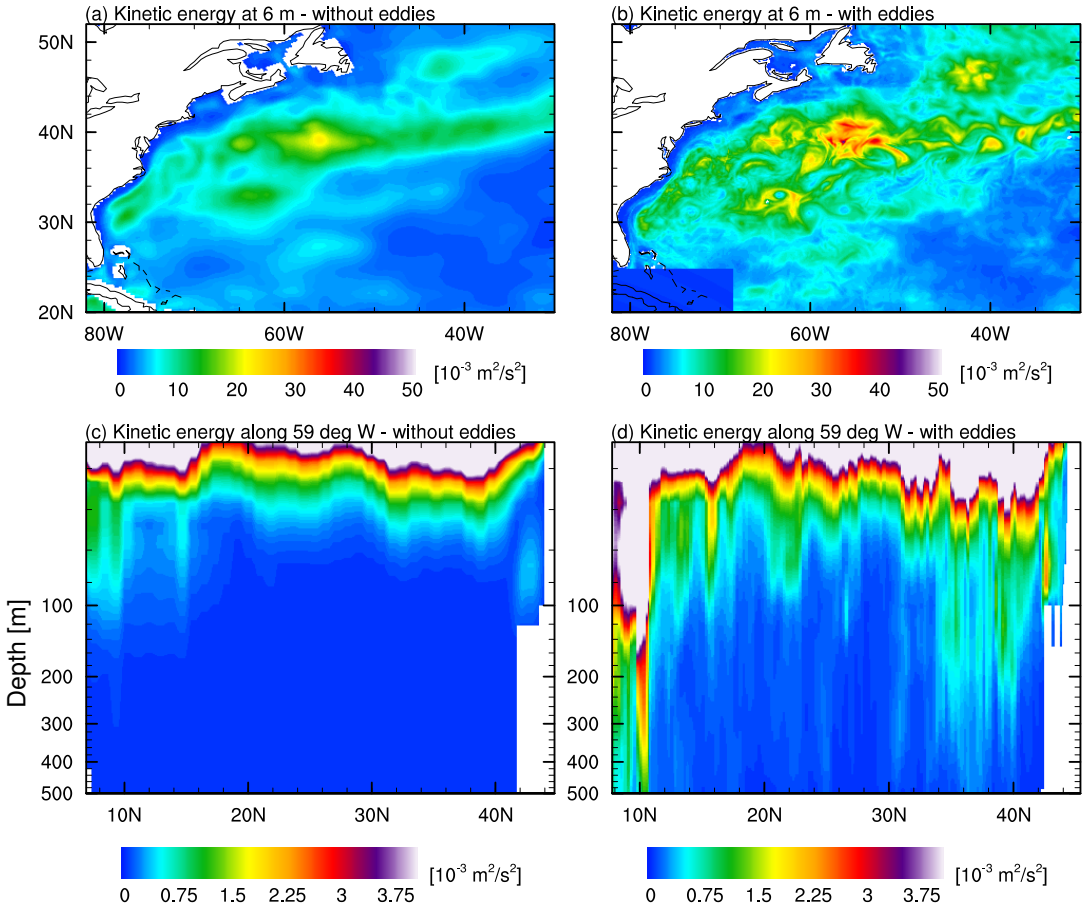

Figure 4.4: Spatial distribution of near-inertial kinetic energy calculated from bandpass filtered model velocities at 6 m depth for the experiment (a) without eddies and (b) with eddies. Vertical cross-section of the near-inertial kinetic energy along 59° W for the experiment (c) without eddies and (d) with eddies.

the experiment without eddies. Energy in general decreases with depth but an increase in the interior with a secondary maxima, marked with black dots, is seen for some areas. The secondary maxima are present in both experiments, but the energy level is lower for the experiment without eddies. In all areas, near-inertial kinetic energy is lower for the experiment without eddies and the reduction with depth is faster. In the upper ocean (above 50 m) energy decrease is similar for both experiments, with almost parallel vertical profiles. Deeper in the ocean this decrease is much more pronounced for the experiment without eddies and the vertical profiles of two experiments are no longer parallel.

4.3 Conclusions

In this chapter we address the influence of the model resolution on the simulated near-inertial kinetic energy in the ocean. More precisely, we investigate the difference in the near-inertial kinetic energy and vertical velocity spectrum by performing experiment with a global ocean general circulation model at 1/10° horizontal resolution (experiment with eddies) and at 0.4° horizontal resolution (experiment without eddies). In both experiments the model is driven by the same surface fluxes of heat, fresh water and momentum obtained from the NCEP reanalysis, and the

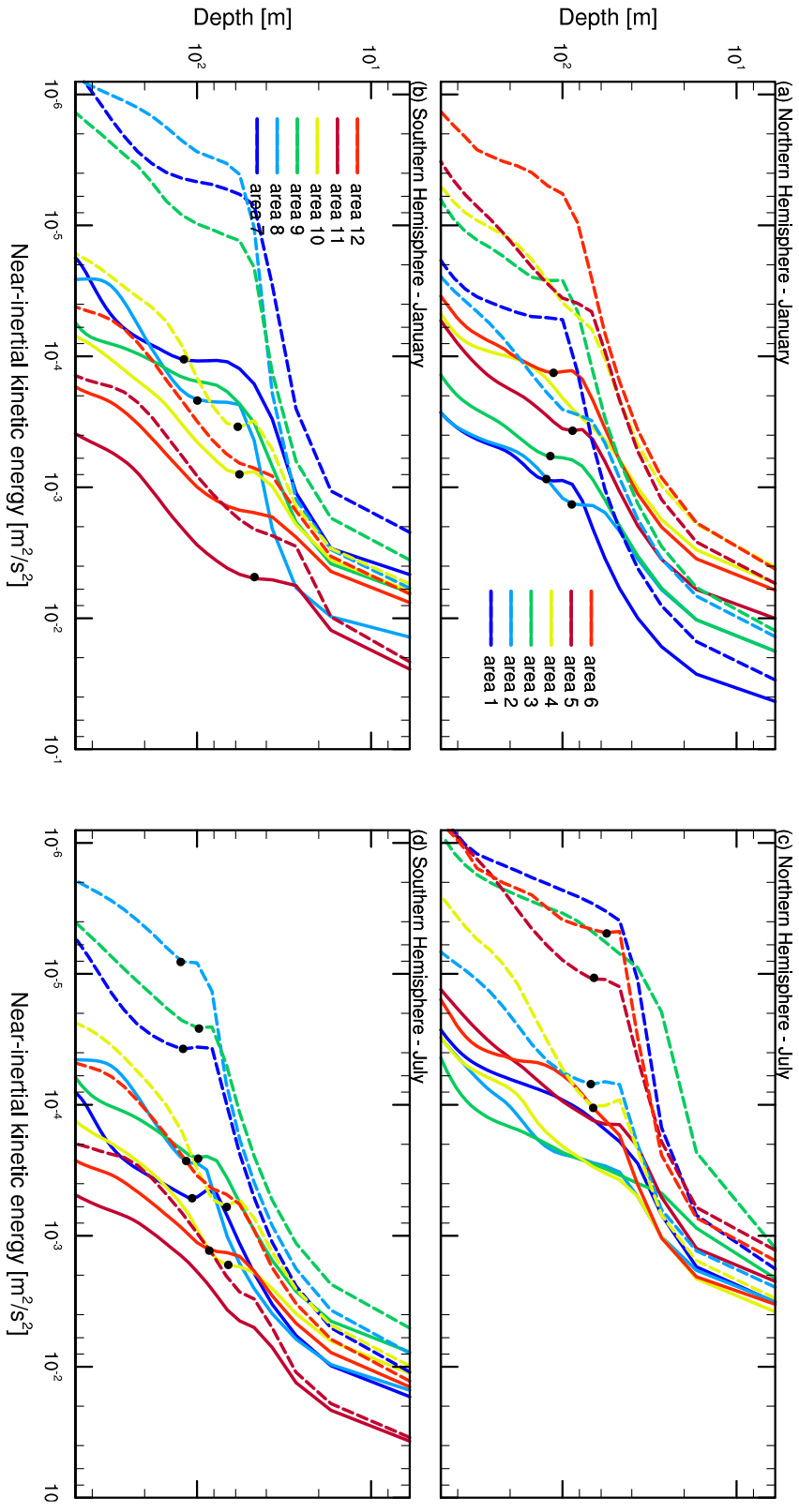

Figure 4.5: Vertical profiles of near-inertial kinetic energy averaged over the areas highlighted in Figure 3.3a. Energy is calculated from the bandpass-filtered model velocities for the areas in (a) the Northern Hemisphere and in (b) the Southern Hemisphere for January, and in (c) the Northern Hemisphere and in (d) the Southern Hemisphere for July. Solid lines represent the experiment with eddies and dashed lines without eddies. Black dots mark the presence of secondary energy maxima in the ocean interior.

only difference between two experiments is the horizontal resolution of the used model. Vertical velocity spectra, calculated for several depths in the interior of the ocean, show that energy in the experiment without eddies is up to 96% lower compared to the experiment with eddies (Figure 4.1). The energy maximum at the local inertial frequency decreases with depth in the experiment without eddies while it is almost constant or slightly enhanced with depth in the experiment with eddies. Also, the spectral peaks are shifted from the local inertial frequency to higher frequencies. This shift is hardly visible in the experiment without eddies where the peaks are centered at f. Although the frequency shift can be caused by the interaction between locally generated waves and waves propagating from higher latitudes, the presence of mesoscale eddies amplifies the frequency shift. The near-inertial kinetic energy in the ocean surface layer is similar for both experiments. At greater depth the energy increases with increasing horizontal resolution of the used model (Figure 4.2 and Figure 4.3). Its area-averaged value is also similar at the ocean surface while at 100 m it is almost three times higher in experiment with eddies compared to experiment without eddies. Horizontal distribution from a small region in the North Atlantic (Figure 4.4) suggests that near-inertial kinetic energy in the presence of mesoscale eddies shows small spatial structures with rapidly varying amplitude. In the experiment without eddies the energy distribution is much smoother. Vertical transects show no significant near-inertial kinetic energy below 100 m in the experiment without eddies, while in the experiment with eddies, energy is confined in vertical "chimneys".

To conclude, our model results suggest that the vertical propagation of near-inertial energy is somewhat enhanced in the presence of mesoscale eddies. There is an important role played by eddies (with anticyclonic orientation, see Section 3.3), which drain near-inertial energy to the deep ocean through the "inertial chimney" effect. The "inertial chimney" effect could be an important way to generate mixing in the ocean interior, since they can drain the near-inertial energy more locally instead of transferring it to lower latitudes (Zhai et al., 2005, 2007). It should also be noted that the weak near-inertial kinetic energy, in particular in the deep ocean can also be related to the fact that the 1/10° model provides a better simulation of waves, including their propagating properties. Additional experiments are needed to further separate the role of eddies and the effect of resolution.

5 Summary and perspectives

5.1 Summary of most relevant findings

In this thesis we investigate wind-induced near-inertial waves and their influence on the energetics of the ocean. This is a relevant subject as the ocean general circulation appears to be a mechanically driven phenomenon. The energy source needed to drive the Meridional Overturning Circulation (MOC) and induce deep-ocean mixing is mainly supplied by the wind stress fluctuations and deep tides. The tidal mixing component can account for approximately half of the required power, whereas the wind provides the remainder. One important way for winds to provide energy, is to generate near-inertial waves. In this thesis we make use of the Max Planck Institute Ocean Model (MPIOM) at a medium (0.4°) and a high horizontal (1/10°) resolution. Model is forced by two different wind stress products, the first obtained from the National Centers for Environmental Prediction/National Centers for Atmospheric Research (NCEP/NCAR) reanalysis at a low spatial and temporal resolution (approximately 1.875°, 6-hourly), and the second from the Climate Forecast System Reanalysis (CFSR) at a high spatial and temporal resolution (approximately 0.35°, 1-hourly). By studying near-inertial waves using an OGCM at a medium-resolution forced by wind stress field at a high-resolution, we believe that we acquire a better quantification of the energy from the winds at the surface of the ocean than previous researchers did who based their studies on slab ocean models. Using a high-resolution model we make the contribution to better understanding of the energy distribution in the ocean interior and its dissipation in the oceanic mixed layer. By studying vertical structure of near-inertial kinetic energy we are able to show that the energy is not only generated at the ocean surface but also in its interior. By analyzing spatial and temporal characteristics of near-inertial waves we can make the conclusions of the general properties of these waves on the global domain. When comparing simulations at two different resolutions, we can perform direct analysis of the influence of mesoscale eddies on the near-inertial kinetic energy in the ocean.

The influence of the resolution of wind stress forcing on the power input to near-inertial motions in the ocean (Chapter 2)

Using MPIOM at a medium horizontal resolution and driven by the same fluxes of heat and fresh water but with different wind stress at a high- and low-resolution in space and time, we address the influence of wind stress forcing on the generation of near-inertial motions in the ocean. For this analysis we use 1-hourly model output for year 2005. We find that:

- The near-inertial kinetic energy increases with increasing resolution in the wind stress forcing. Its area-averaged value is three times higher (up to a factor four in the storm track regions) in experiment CFSR (forced by high-resolution wind stress) compared to experiment NCEP (forced by low-resolution wind stress).
- The wind-power input to surface near-inertial motions is 1.1 TW in the experiment CFSR, while only 0.3 TW in the experiment NCEP.
- Time and space filtering of the CFSR wind stress fields yield less near-inertial kinetic energy, but the stronger reduction comes from time filtering. This suggests that the high-frequency temporal variations in the wind stress field are more efficient in generating near-inertial wave energy than small-scale spatial variations in the wind stress field.

The impact of resolution of the wind stress field has so far been studied using slab ocean models forced by realistic wind stress products (namely NCEP wind stress). Klein et al. (2004a) pointed out that the near-inertial energy integrated over a water column decreases by 20% when wind stress fields are changed from 3- to 6-hourly mean values. They stressed the importance of the temporal resolution of the wind stress field. On the other hand, Jiang et al. (2005) stressed the importance of the spatial resolution. They found an increase in the kinetic energy flux with increasing horizontal resolution. In Chapter 2, we analyze the relative role of the temporal and spatial resolution using an OGCM. We attribute increased wind-power input to near-inertial motions to the better temporal resolution of the CFSR winds compared to NCEP winds. Our results show that there is a strong sensitivity of the kinetic energy and the wind-power input to the resolution of the used wind forcing. This points to a possible underestimation of the wind generated energy available for deep-ocean mixing in previous studies based on wind data with low horizontal and temporal resolutions.

General properties of near-inertial waves simulated using a 1/10° ocean model (Chapter 3)

The second set of research questions is addressed in Chapter 3. Since near-inertial waves are better simulated using a model at higher resolution we use 1/10° ocean model. The model is driven by the NCEP wind stress field at a low horizontal and temporal resolution. For the analysis we use 1-hourly model output from January and July 2005.

First, we investigate the vertical structure of near-inertial kinetic energy in the ocean and the energy change with depth. Here, we also include a realistic spatial distribution of the mixed layer depth calculated from spatially and temporally varying temperature and salinity fields using sigma-t density criterion defined by Levitus (1982). We find that:

- The vertical structure of near-inertial kinetic energy shows high energy levels in the ocean surface layer for both months, but this surface intensification is stronger in the winter hemisphere than in the summer hemisphere. This indicates that the near-inertial kinetic energy has a seasonal cycle with a maximum energy in winter that is mostly pronounced in the upper 200 m. The surface intensification suggests that near-inertial waves are primarily forced at the ocean surface by the passage of the winter storms.

- In the equatorial regions, strong near-inertial kinetic energy is present throughout the water column. This indicates that next to locally generated waves there is an additional source of energy which might be waves propagating from higher latitudes, or other mechanisms such as tropical instability waves.

- Vertical profiles show that the energy is drained into the deep ocean and high energy levels are confined in "internal chimneys".

- The area averaged near-inertial kinetic energy shows that the energy decreases with depth. In winter hemisphere there is a small maximum seen at the base of the mixed layer. This maximum is also seen in summer hemisphere but well below the base of the mixed layer.

Higher near-inertial kinetic energy at the base of the mixed layer suggests the possible existence of additional source of energy in the ocean interior. One basic mechanism that might influence the energy at the base of the mixed layer is the Ekman transport where strong surface flows cause net convergence and downwelling of the ocean flows.

Second, we study the fraction of the total wind-induced near-inertial energy flux leaving the mixed layer using a 1/10° ocean model and a spatially and temporally varying mixed layer. We find that:

- Of 0.34 TW of the mean wind-power input to surface near-inertial motions in two months, the mean near-inertial energy leaving the mixed layer amounts to 0.037 TW. This results in a mean fraction of 10.8% while the remainder of the energy is dissipated in the mixed layer.

- The fraction tends to decrease with increasing depth of the mixed layer and with increasing variability of the wind stress, indicating the strong control of the turbulent dissipation over the fraction inside the mixed layer.

It is important to study the energy flux leaving the mixed layer using a realistic spatial structure of the mixed layer depth, and not only the energy flux at a constant depth in the ocean, because the mixed layer depth signifies the depth waves need to pass before being able to freely propagate into the deep ocean. We further quantify the role of wind stress variability and its influence on the fraction of the total near-inertial energy flux leaving the mixed layer, since the wind stress variability can, on one hand, lead to mixing of the momentum and therefore the dissipation of near-inertial waves within the mixed layer, and on the other hand, it can strengthen the wind-power input to near-inertial waves. Our results suggest a possible overestimation of the wind-power input to near-inertial waves in the ocean interior and the need of other energy sources for deep-ocean mixing or different energy pathways for wind-power input to deep ocean.

In the end, characteristic scales of near-inertial waves are addressed on a global domain and at several oceanic levels using vertical velocity simulations from a high-resolution ocean model. Wavenumber and frequency spectra, coherence and spectral phase are used to analyze the variability, horizontal scale, and horizontal and vertical propagation of near-inertial waves. For the calculation we use the areas where vertical velocity has high variability, where it shows dominant zonal wave structures and it is not influenced by the mesoscale eddies. We find:

- The horizontal length scale of near-inertial waves is in a range of approximately 200-500 km. The energy is in general higher in the winter hemisphere, indicating a strong influence from the winds on the wavenumber spectra. Spectra integrated over all zonal or meridional wavenumbers indicate the dominance of meridional wavenumbers.

- Frequency spectra show a distinct energy maximum near the local inertial frequency f, and for some areas the smaller maximum at the double inertial frequency $2f$. This suggests that near-inertial waves are the dominant motions in the internal wave spectrum. The height and the broadness of the energy maximum depend on the distance of the area used for the calculation from the equator. The maxima are not centered at f and $2f$ but they are shifted to higher frequencies for all areas. The frequency shift is less prominent at 100 m than at 500 m and for the areas further from the equator than for the areas closer to the equator. There is no universal shape over the internal wave frequency range (frequencies higher than f).

- The horizontal coherence scale is about 20 to 240 km, while the vertical coherence scale is about 50 m and more. Phase difference calculated between pairs of grid points x_1 that is always fixed, and x_2 that is moving and estimated at the inertial frequency of grid point x_1 relative to the distance of the grid point x_2 suggests that near-inertial waves propagate towards the equator in horizontal direction, while in the vertical direction near-inertial waves propagate from the deep ocean towards the surface. In the deep ocean spectral phase shows a possible existence of standing waves.

Influence of the meoscale eddies on near-inertial motions (Chapter 4)

In Chapter 4 we address the third research question of the thesis by comparing the results from two different model resolutions to evaluate the influence of mesoscale eddies on simulated near-inertial motions in the ocean. Here, we use the high- (1/10°, a simulation with that a significant bulk of mesoscale eddies can be resolved) and low-resolution (0.4°, a resolution with that no strong mesoscale eddy activity can be simulated) model forced by wind stress at low horizontal and temporal resolution (approximately 1.875°, 6-hourly). We find that:

- Vertical velocity spectra show that the energy is up to 96% smaller in the experiments without eddies compared to experiments with eddies. The spectral peaks are not centered at f and $2f$, but shifted towards higher frequencies in the experiment with eddies.

- The spatial distribution of the near-inertial kinetic energy and the wind-power input to near-inertial motions at the ocean surface are similar in both experiments despite the difference in the model resolutions. The similarities are mostly related to large scale ocean patterns connected to mid-latitude storm tracks. A change from experiments without eddies to

experiments with eddies in the ocean interior results in a threefold increase in the near-inertial kinetic energy.

- Horizontal distribution from a small region in the North Atlantic suggests that near-inertial kinetic energy in the presence of mesoscale eddies shows small spatial structures with rapidly varying amplitudes. This structures are not seen in the experiments without eddies where the near-inertial kinetic energy has a smooth horizontal distribution.

- Vertical transects reveal high levels of near-inertial kinetic energy leaking into the deep ocean in the experiments with eddies.

The vertical propagation of near-inertial kinetic energy is enhanced in the presence of mesoscale eddies. The important role is played by mesoscale eddies with an anticyclonic orientation in draining the energy to the deep ocean through the "internal chimney" effect. This strong sensitivity of the near-inertial kinetic energy to the presence of mesoscale eddies can play a crucial role for mixing in the ocean interior.

5.2 Perspectives

In this thesis we obtain the complete overview of the oceanic near-inertial response to high-resolution wind stress field based on the ocean model MPIOM. In Chapter 3 we show that near-inertial energy induced at the ocean surface propagates into deeper layers of the ocean. The propagation of the energy and its possible dissipation inside the oceanic mixed layer depends on the used mixing scheme. In our ocean model the Pacanowski and Philander (1981) mixing scheme is implemented. It includes a non-constant parametrization of vertical eddy viscosity and eddy diffusivity based on the Richardson number. In its classical form, this mixing scheme underestimates turbulent mixing close to the ocean surface. Therefore, an additional parametrization for wind induced stirring, which is a function of a local 10 m wind speed, is included. Even though this mixing scheme provides more realistic dissipation of near-inertial energy in the upper ocean than a slab ocean with a simple Rayleigh drag does, it is far from being perfect. A similar analysis using other mixing schemes would help to further verify our results. For example, Gaspar et al. (1990) is one of the more sophisticated mixing schemes. It is designed to simulate vertical mixing at all depths, from the upper boundary layer down to the abyss. This scheme includes a single prognostic equation for the turbulent kinetic energy.

In Chapter 3 we provided a simple but fundamental overview of general properties of near-inertial waves. We investigated characteristic spatial and temporal scales of near-inertial waves. One question that arises is whether the defined scales reflect the first baroclinic mode only or as well higher vertical modes. Additional consideration of the Sturm-Liouville eigenvalue problem using the simulated stratification profile is needed to answer this question.

In Chapter 4 we made our analysis on the influence of mesoscale eddies on near-inertial waves based on two different model resolutions, first, a medium-resolution (0.4°) which can hardly resolve mesoscale eddies and second, a high-resolution (1/10°) model which can resolve mesoscale eddies. This study can be extended to study the influence of mesoscale eddies and currents on near-inertial waves. Influence of currents on near-inertial waves can be studied by decomposing wind stress into a yearly mean $\overline{\tau}$, variations on time scales longer than one year τ_{ac} and variations on a time

scales shorter than one year τ'. With this decomposition and with an ocean model at different resolution we may be able to find model configurations capable of quantifying the role of eddies in a more precise manner than the configurations used in Chapter 4.

In Chapter 3 we show that only 10.8% of the total wind-power input at the ocean surface propagates below the mixed layer while the reminder of the energy is dissipated in the mixed layer. This result suggests that there is a need for the existence of other energy sources for deep-ocean mixing or different energy pathways for wind-power input to deep ocean. It is necessary to extend our analysis and to search for different energy sources, such as wave energy generation at the topography, to sustain the global general circulation in the ocean.

A

Mathematical methods

To fully analyze and describe near-inertial motions we need to use some basic mathematical tools such as integrated cross-covariance, band-pass filtered covariance, two-dimensional Fourier decomposition, magnitude squared coherence and spectral phase. In the following sections, this issues are briefly touched. More extensive material may be found in classical textbooks such as e.g., Stull (1988), von Storch and Zwiers (1999).

A.1 A rotary spectral method for analyzing vector time series

In this section, we introduce a rotary spectral method for analyzing geophysical flows influenced by Earth's rotation. The water particles in their motion are resolved along an elliptical orbit because of the Coriolis force. For near-inertial motions, the orbit is purely circular and does not go outside the horizontal plane.

A rotary spectral method decomposes vector motions in counter-rotating (clockwise and anticlockwise) circular components (Gonella, 1972). We define the sea-water velocity rotary-vector component $\mathbf{u}$ as a complex quantity:

$$\mathbf{u} = \mathbf{u}_1 \mp i\mathbf{u}_2, \tag{A.1}$$

where $\mathbf{u}_1$ represents zonal and $\mathbf{u}_2$ meridional velocity vector component, while the sign $\mp$ represents a final vector orientation in the anticyclonic or cyclonic circular direction. Clockwise motions (at positive frequencies) are anticyclonic in the Northern Hemisphere, and cyclonic in the Southern Hemisphere. The opposite is true for anticlockwise motions (at negative frequencies in the Northern Hemisphere. Figure A.1 represents a spatial distribution of the portion of clockwise near-inertial kinetic energy relative to the total near-inertial kinetic energy, i.e., it shows the dominance of clockwise rotary energy over anticlockwise rotary energy near the inertial frequency. Small ratio in the Southern Hemisphere indicates that anticlockwise rotation dominates clockwise rotation. This result confirms the dominance of anticyclonic (clockwise in the Northern Hemisphere and anticlockwise in the Southern Hemisphere) rotary energy near the inertial frequency.

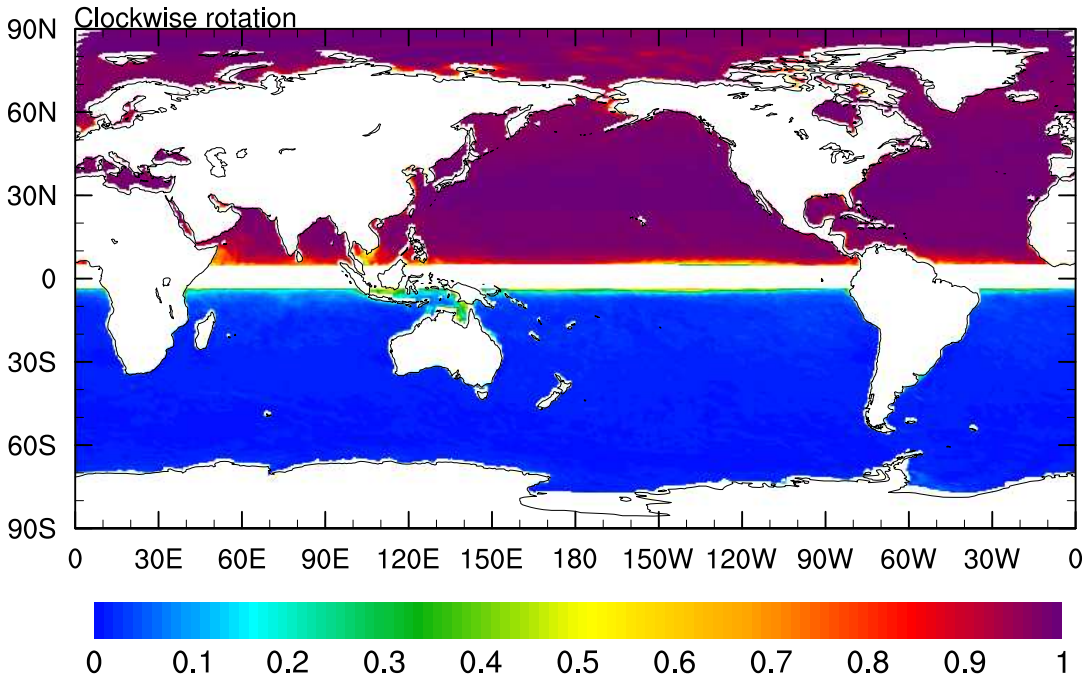

Figure A.1: Spatial distribution of the portion of clockwise near-inertial kinetic energy relative to the total near-inertial kinetic energy. Large values in the Northern Hemisphere (∼1) indicate that clockwise rotation dominates anticlockwise rotation.

A.2 Wind generated power input to near-inertial motions

Two different methods for calculating wind generated power input to near-inertial motions are introduced in this section:

1. Calculating the integrated cross-covariance between wind stress and velocity at near-inertial frequency range.
2. Calculating the covariance between wind stress and velocity. Both wind stress and velocity, are filtered around inertial frequency.

In our calculation of the wind generated power to near-inertial motions, the near-inertial frequency range is defined by frequencies ω: $0.7f < \omega < 1.3f$. Here, f denotes the local inertial frequency defined as: $f = 2\Omega \sin\varphi$, where Ω is the rotation rate of the Earth ($\Omega = 7.2921 \cdot 10^{-5}$ rad/s), and φ is a geographical latitude. In this calculation, we will show that both methods obtain the same result for any frequency range.

A.2.1 Integrated cross-covariance

To calculate an integrated cross-covariance at a near-inertial frequency range, we start with two real time series X_t and Y_t at time $t = 0, ..., T-1$, with T being the total number of time points. Time series X_t and Y_t are, in our case, wind stress and velocity, respectively. These time series can be decomposed in terms of complex valued exponential functions as:

$$\begin{aligned} X_t &= \sum_{k=-n}^{n-1} A_k e^{i2\pi\omega_k t}, \\ Y_t &= \sum_{k=-n}^{n-1} B_k e^{i2\pi\omega_k t}. \end{aligned} \tag{A.2}$$

Fourier coefficients A_k and B_k are defined at the given frequencies $\omega_k = k/T$, with $k = -n, ..., n-1$, where n is the number of resolved frequencies, and T is the total number of time steps. The complex valued coefficients A_k and B_k satisfy relations: $\overline{A_{-k}} = A_k$ and $\overline{B_{-k}} = B_k$, where the overline represents the complex conjugate value. The Fourier coefficients A_k and B_k are defined as:

$$\begin{aligned} A_k &= \frac{1}{T}\sum_{t=0}^{T-1} X_t e^{-i2\pi\omega_k t}, \\ B_k &= \frac{1}{T}\sum_{t=0}^{T-1} Y_t e^{-i2\pi\omega_k t}. \end{aligned} \tag{A.3}$$

We decompose exponential function into sines and cosines:

$$\begin{aligned} A_k &= \frac{1}{T}\sum_{t=0}^{T-1} X_t\big(\cos(2\pi\omega_k t) - i\sin(2\pi\omega_k t)\big) \\ &= \frac{1}{T}\sum_{t=0}^{T-1} X_t\cos(2\pi\omega_k t) - i\frac{1}{T}\sum_{t=0}^{T-1} X_t\sin(2\pi\omega_k t) \\ &= A_k^{Re} + iA_k^{Im}, \end{aligned} \tag{A.4}$$

and

$$\begin{aligned} B_k &= \frac{1}{T}\sum_{t=0}^{T-1} Y_t\big(\cos(2\pi\omega_k t) - i\sin(2\pi\omega_k t)\big) \\ &= \frac{1}{T}\sum_{t=0}^{T-1} Y_t\cos(2\pi\omega_k t) - i\frac{1}{T}\sum_{t=0}^{T-1} Y_t\sin(2\pi\omega_k t) \\ &= B_k^{Re} + iB_k^{Im}. \end{aligned} \tag{A.5}$$

To obtain the integrated cross-covariance of wind stress and velocity $C_{XY\Delta k}$, we need to calculate a cross-periodogram by multiplying the Fourier coefficients A_k and B_k. A cross-periodogram I_{XYk} is defined as (von Storch and Zwiers, 1999):

$$\begin{aligned} I_{XYk} &= TA_k\overline{B_k} \\ &= T(A_k^{Re} + iA_k^{Im})\overline{(B_k^{Re} + iB_k^{Im})} \\ &= T(A_k^{Re}B_k^{Re} - iA_k^{Re}B_k^{Im} + iA_k^{Im}B_k^{Re} + A_k^{Im}B_k^{Im}). \end{aligned} \tag{A.6}$$

In this calculation, we define the near-inertial frequency range with frequencies: $\omega_{k-1} = (k-1)/T$, $\omega_k = k/T$, and $\omega_{k+1} = (k+1)/t$, where k can be positive and negative integer. We obtain the cross-covariance $C_{XY\Delta k}$ by integrating the cross-periodogram $I_{XY\Delta k}$ over the defined near-inertial frequency range:

$$\begin{aligned} C_{XY\Delta k} &= \int_{\Delta\omega} I_{XY\Delta k}\,d\omega \\ &= \frac{I_{XYk-1}}{T} + \frac{I_{XYk}}{T} + \frac{I_{XYk+1}}{T} \\ &\quad + \frac{I_{XY-k+1}}{T} + \frac{I_{XY-k}}{T} + \frac{I_{XY-k-1}}{T} \\ &= 2A_{k-1}^{Re}B_{k-1}^{Re} + 2A_{k-1}^{Im}B_{k-1}^{Im} + 2A_k^{Re}B_k^{Re} \\ &\quad + 2A_k^{Im}B_k^{Im} + 2A_{k+1}^{Re}B_{k+1}^{Re} + 2A_{k+1}^{Im}B_{k+1}^{Im}. \end{aligned} \tag{A.7}$$

A.2.2 Band-pass filtered covariance

We use the Fourier coefficients (Equation A.3) defined in Section A.2.1 to obtain bandpass filtered time series of wind stress $\widetilde{X_t}$ and velocity $\widetilde{Y_t}$. These time series, $\widetilde{X_t}$ and $\widetilde{Y_t}$, are filtered around the inertial frequency, which is in this calculation defined as: $\omega_{k-1} = (k-1)/T$, $\omega_k = k/T$, and $\omega_{k+1} = (k+1)/t$, where k can be positive or negative integer. Bandpass filtered time series are

defined as:

$$\begin{aligned}\widetilde{X_t} &= A_{k-1}e^{i2\pi\omega_{k-1}t} + A_k e^{i2\pi\omega_k t} + A_{k+1}e^{i2\pi\omega_{k+1}t} \\ &\quad + A_{-k+1}e^{-i2\pi\omega_{k-1}t} + A_{-k}e^{i2\pi\omega_{-k}t} + A_{-k-1}e^{-i2\pi\omega_{k+1}t} \\ &= 2A_{k-1}^{Re}\cos(2\pi\omega_{k-1}t) + 2A_k^{Re}\cos(2\pi\omega_k t) + 2A_{k+1}^{Re}\cos(2\pi\omega_{k+1}t) \\ &\quad - 2A_{k-1}^{Im}\sin(2\pi\omega_{k-1}t) - 2A_k^{Im}\sin(2\pi\omega_k t) - 2A_{k+1}^{Im}\sin(2\pi\omega_{k+1}t),\end{aligned}$$

and

$$\begin{aligned}\widetilde{Y_t} &= B_{k-1}e^{i2\pi\omega_{k-1}t} + B_k e^{i2\pi\omega_k t} + B_{k+1}e^{i2\pi\omega_{k+1}t} \\ &\quad + B_{-k+1}e^{-i2\pi\omega_{k-1}t} + B_{-k}e^{i2\pi\omega_{-k}t} + B_{-k-1}e^{-i2\pi\omega_{k+1}t} \\ &= 2B_{k-1}^{Re}\cos(2\pi\omega_{k-1}t) + 2B_k^{Re}\cos(2\pi\omega_k t) + 2B_{k+1}^{Re}\cos(2\pi\omega_{k+1}t) \\ &\quad - 2B_{k-1}^{Im}\sin(2\pi\omega_{k-1}t) - 2B_k^{Im}\sin(2\pi\omega_k t) - 2B_{k+1}^{Im}\sin(2\pi\omega_{k+1}t). \qquad \text{(A.8)}\end{aligned}$$

We calculate the covariance $C_{\widetilde{X_t}\widetilde{Y_t}}$ between wind stress and velocity as a multiple of the bandpass filtered time series $\widetilde{X_t}$ and $\widetilde{Y_t}$ as:

$$\begin{aligned}C_{\widetilde{X_t}\widetilde{Y_t}} &= \frac{1}{T}\sum_{t=0}^{T-1}\widetilde{X_t}\widetilde{Y_t} \\ &= 2A_{k-1}^{Re}B_{k-1}^{Re} + 2A_{k-1}^{Im}B_{k-1}^{Im} + 2A_k^{Re}B_k^{Re} \\ &\quad + 2A_k^{Im}B_k^{Im} + 2A_{k+1}^{Re}B_{k+1}^{Re} + 2A_{k+1}^{Im}B_{k+1}^{Im}. \qquad \text{(A.9)}\end{aligned}$$

To conclude, the wind generated power input to near-inertial motions is calculated using two different methods. We calculate the integrated cross-covariance between wind stress and velocity, and the covariance of the bandpass filtered wind stress and velocity. Both calculations are done at the near-inertial frequency range defined with frequencies: $\omega_{k-1} = (k-1)/T$, $\omega_k = k/T$, and $\omega_{k+1} = (k+1)/t$. We show that both methods give the same result (Equation A.7 equals Equation A.9), which depends only on the Fourier coefficients A_k and B_k.

A.3 Two-dimensional Fourier decomposition for analyzing spatial scales of near-inertial motions

In this section we introduce the concept of two-dimensional (2D) Fourier decomposition and its application for calculating a wavenumber energy spectrum of near-inertial motions. The wavenumber represents the spatial frequency of a wave, either in cycles per unit distance or radians per unit distance. It can be envisaged as the number of waves that exist over a specified distance (analogous to frequency being the number of cycles or radians per unit time). The wavenumber spectrum represents the distribution of the wave energy at the wavenumber of interest.

To calculate a wavenumber energy spectrum of near-inertial motions, we start from a real time series of vertical velocity F_{xy}. Velocity is defined at zonal $x = 0, ..., X-1$, and meridional $y = 0, ..., Y-1$ positions, with X and Y being the total number of points in zonal and meridional direction, respectively. The time series F_{xy} can be decomposed in terms of a complex valued exponential function as:

$$F_{xy} = \sum_{p=-n_x}^{n_x-1} \sum_{q=-n_y}^{n_y-1} A_{pq} e^{i2\pi(\nu_p x + \nu_q y)}. \tag{A.10}$$

The 2D Fourier coefficient A_{pq} is given at a zonal and meridional wavenumber $\nu_p = p/X$ and $\nu_q = q/Y$, respectively, with $p = -n_x, ..., n_x-1$ and $q = -n_y, ..., n_y-1$. The numbers of resolved zonal and meridional wave numbers are n_x and n_y. The Fourier coefficient A_{pq} is defined as:

$$A_{pq} = \frac{1}{XY} \sum_{x=0}^{X-1} \sum_{y=0}^{Y-1} F_{xy} e^{-i2\pi(\nu_p x + \nu_q y)}. \tag{A.11}$$

Since F_{xy} is a function of two spatial variables x and y 2D Fourier decomposition can be obtained by repeating the one-dimensional Fourier decomposition in zonal and then in meridional direction.

Using the Fourier coefficient A_{pq} we compute a periodogram $I_{A_{pq}}$ as: $I_{A_{pq}} = 2|A_{pq}|^2$. Furthermore we estimate 2D spectrum $\widehat{\Gamma}(\nu_p, \nu_q)$ using the Daniell spectral estimator following von Storch and Zwiers (1999) as:

$$\widehat{\Gamma}(\nu_p, \nu_q) = \frac{1}{mn} \sum_{i=p-(m-1)/2}^{p+(m-1)/2} \sum_{j=q-(n-1)/2}^{q+(n-1)/2} I_{A_{pq}}. \tag{A.12}$$

The Daniell spectral estimator is defined as the average of an odd number of the periodogram ordinates, that are given with m and n. Finally, we calculate the horizontal kinetic energy spectrum as an average of all points at the same radial distance (the same horizontal wave number K_h) from the origin of the coordinate system. The horizontal wavenumber is calculated from the discrete wavenumbers in zonal ν_p and meridional ν_q direction as:

$$K_h = \sqrt{\nu_p^2 + \nu_q^2}. \tag{A.13}$$

A.4 Coherence spectrum and spectral phase

In this section we introduce the concept of coherence spectrum and spectral phase, and their application for understanding correlation between two waves that are represented by two time series, and their direction of propagation. In our calculation, the coherence spectrum is smoothed by using the Daniell spectral estimator (von Storch and Zwiers, 1999), and it is thought of as a squared correlation coefficient that depends upon frequency.

To calculate the coherence spectrum, we start from from two real time series of velocity X_t and Y_t. These time series X_t and Y_t can be decomposed in terms of complex valued exponential functions as:

$$\begin{aligned} X_t &= \sum_{k=-n}^{n-1} A_k e^{i2\pi\omega_k t}, \\ Y_t &= \sum_{k=-n}^{n-1} B_k e^{i2\pi\omega_k t}. \end{aligned} \tag{A.14}$$

Fourier coefficients A_k and B_k are defined at the given frequencies $\omega_k = k/T$ with $k = -n, ..., n-1$, where n is the number of resolved frequencies and T is the total number of time steps. The complex valued coefficients A_k and B_k satisfy the relations: $\overline{A_{-k}} = A_k$ and $\overline{B_{-k}} = B_k$, where the overline represents the complex conjugate value. The Fourier coefficients A_k and B_k are defined as:

$$\begin{aligned} A_k &= \frac{1}{T}\sum_{t=0}^{T-1} X_t e^{-i2\pi\omega_k t}, \\ B_k &= \frac{1}{T}\sum_{t=0}^{T-1} Y_t e^{-i2\pi\omega_k t}. \end{aligned} \tag{A.15}$$

Next, we calculate a cross-periodogram I_{XYk} by multiplying the Fourier coefficients A_k and B_k as: $I_{XYk} = TA_k\overline{B_k}$. Furthermore, we estimate a cross-spectrum using Daniell cross-spectral estimator following von Storch and Zwiers (1999) as:

$$\begin{aligned} \widehat{\Gamma}(\omega_k) &= \frac{1}{T^2}\sum_{i=k-(m-1)/2}^{k+(m-1)/2} I_{XYk}, \\ \widehat{\Gamma}(\omega_k) &= \frac{1}{T}\sum_{i=k-(m-1)/2}^{k+(m-1)/2} A_k\overline{B_k}. \end{aligned} \tag{A.16}$$

In the equations, m is an odd number of periodogram ordinates which we use to smooth our periodogram. In the same way we calculate auto-periodogram $I_{XXk} = TA_k\overline{A_k}$ and $I_{YYk} = TB_k\overline{B_k}$ to obtain auto-spectrum:

$$\begin{aligned}\widehat{\Gamma_X}(\omega_k) &= \frac{1}{T^2}\sum_{i=k-(m-1)/2}^{k+(m-1)/2} I_{XXk},\\ \widehat{\Gamma_X}(\omega_k) &= \frac{1}{T}\sum_{i=k-(m-1)/2}^{k+(m-1)/2} A_k\overline{A_k}.\end{aligned} \tag{A.17}$$

and

$$\begin{aligned}\widehat{\Gamma_Y}(\omega_k) &= \frac{1}{T^2}\sum_{i=k-(m-1)/2}^{k+(m-1)/2} I_{YYk},\\ \widehat{\Gamma_Y}(\omega_k) &= \frac{1}{T}\sum_{i=k-(m-1)/2}^{k+(m-1)/2} B_k\overline{B_k}.\end{aligned} \tag{A.18}$$

In the end, we calculate the coherence spectrum $\widehat{\rho_{XY}}(\omega_k)$ as:

$$\widehat{\rho_{XY}}(\omega_k) = \frac{\widehat{\Gamma}^2(\omega_k)}{(\widehat{\Gamma_X}(\omega_k)\widehat{\Gamma_Y}(\omega_k))}. \tag{A.19}$$

To obtain the spectral phase we calculate the ratio between imaginary and real part of the Equation A.16.

References

Alford, M., 2001: Internal swell generation: The spatial distribution of energy flux from the wind to mixed layer near-inertial motions. *Journal of Physical Oceanography*, **31**, doi:http://dx.doi.org/10.1175/1520–0485(2001)031<2359:ISGTSD>2.0.CO;2.

Alford, M., 2003a: Improved global maps and 54-year history of wind-work on ocean inertial motions. *Geophysical Research Letters*, **30**, doi:10.1029/2002GL016 614.

Alford, M., 2003b: Redistribution of energy available for ocean mixing by long-range propagation of internal waves. *Nature*, **423**, doi:10.1038/nature01 628.

Alford, M., 2010: Sustained, full-water-column observations of internal waves and mixing near mendocino experiment. *Journal of Physical Oceanography*, **40**, doi:10.1175/2010JPO4502.1.

Alford, M., M. Cronin, and J. Klymak, 2012: Annual cycle and depth penetration of wind-generated near-inertial internal waves at ocean station papa in the northeast pacific. *Journal of Physical Oceanography*, **42**, doi:10.1175/JPO–D–11–092.1.

Anderson, D. and A. Gill, 1979: Beta dispersion of inertial waves. *Journal of Geophysical Research*, **84**, doi: 10.1029/JC084iC04p01 836.

Baines, P. and J. Turner, 1969: Turbulent buoyant convection from a source in a confined region. *Journal of Fluid Mechanics*, **37**, doi:http://dx.doi.org/10.1017/S0022112069000 413.

Chaigneau, A., O. Pizarro, and W. Rojas, 2008: Global climatology of near-inertial current characteristics from lagrangian observations. *Geophysical Research Letters*, **35**, doi:10.1029/2008GL034 060.

Coman, M., R. Griffiths, and G. Hughes, 2006: Sandström's experiments revisited. *Journal of Marine Research*, **64**, 783–796.

Danioux, E. and P. Klein, 2008: A resonance mechanism leading to wind-forced motions with a 2f frequency. *Journal of Physical Oceanography*, **38**, doi:10.1175/2008JPO3822.1.

Danioux, E., P. Klein, M. Heckt, and N. Komori, 2011: Emergence of wind-driven near-inertial waves in the deep ocean triggered by small-scale eddy vorticity structures. *Journal of Physical Oceanography*, **41**, doi:10.1175/2011JPO4537.1.

Danioux, E., P. Klein, and P. Rivière, 2008: Propagation of wind energy into the deep ocean through a fully turbulent mesoscale eddy field. *Journal of Physical Oceanography*, **38**, doi:10.1175/2008JPO3821.1.

D'Asaro, E., 1985: The energy flux from the wind to near-inertial motions in the surface mixed layer. *Journal of Physical Oceanography*, **15**, doi:http://dx.doi.org/10.1175/1520–0485(1985)015<1043:TEFFTW>2.0.CO;2.

Dickey, J., et al., 1994: Lunar lasser ranging: a continuing legacy af the apollo program. *Science*, **265**, doi:10.1126/science.265.5171.482.

Egbert, R. and R. Ray, 2000: Significant dissipation of tidal energy in the deep ocean inferred from satellite altimeter data. *Nature*, **405**, doi:10.1038/35015 531.

Elipot, S. and R. Lumpkin, 2008: Spectral description of oceanic near-surface variability. *Geophysical Research Letters*, **35**, doi:10.1029/2007GL032 874.

Ferrari, R. and C. Wunsch, 2009: Ocean circulation kinetic energy: reservoirs, sources and sinks. *Annual Review Fluid Mechanics*, **41**, doi:10.1146/annurev.fluid.40.111 406.102 139.

Fu, L., 1981: Observations and models of inertial waves in the deep ocean. *Reviews of Geophysics and Space Physics*, **19**, doi:10.1029/RG019i001p00 141.

Furuichi, N., T. Hibiya, and Y. Niwa, 2008: Model-predicted distribution of wind-induced internal wave energy in the world's oceans. *Journal of Geophysical Research*, **113**, doi:10.1029/2008JC004 768.

Garrett, C., 1999: What is the near-inertial band and why is it important. 215–221.

Garrett, C. and W. Munk, 1975: Space-time scales of the internal waves. *Geophysical Fluid Dynamics*, **3**, doi:10.1029/JC080i003p00 291.

Gaspar, P., Y. Gregoris, and J. Lefevre, 1990: A simple eddy kinetic energy model for simulations of the oceanic vertical mixing: Tests at station papa and long-term upper ocean study site. *Journal of Geophysical Research*, **95**, doi:10.1029/JC095iC09p16 179.

Gill, A., 1982: *Atmosphere-ocean dynamics*. Academic Press, San Diego, California, 662 pp.

Gonella, J., 1972: A rotary-component method for analysing meteorological and oceanographic vector time series. *Deep Sea Research*, **19**, doi:10.1016/0011–7471(72)90 002–2.

Green, J. and J. Nycander, 2012: A comparison of tidal conversion parametrizations for tidal models. *Journal of Physical Oceanography*, **43**, doi:http://dx.doi.org/10.1175/JPO–D–12–023.1.

Griffies, S., et al., 2009: Coordinated ocean-ice reference experiments (cores). *Ocean Modelling*, **26**, doi:http://dx.doi.org/10.1016/j.ocemod.2008.08.007.

Hallberg, R., 2003: The ability of large-scale ocean models to accept parametrizations of boundary mixing, and a description of a refined bulk mixed-layer model. internal gravity waves and small-scale turbulence.

Huang, R., 1999: Mixing and energetics of the oceanic thermohaline circulation. *Journal of Physical Oceanography*, **29**, doi:http://dx.doi.org/10.1175/1520–0485(1999)029<0727:MAEOTO>2.0.CO;2.

Jackson, L., R. Hallberg, and S. Legg, 2008: A parametrization of shear-driven turbulence for ocean climate models. *Journal of Physical Oceanography*, **39**, doi:dx.doi.org/10.1175/2009/JPO4085.1.

Jeffreys, H., 1925: On fluid motions produced by differences of temperature and humidity. *Quarterly Journal of the Royal Meteorological Society*, **51**, doi:10.1002/qj.49705121 604.

Jiang, J., Y. Lu, and W. Perrie, 2005: Estimating the energy flux from the wind to ocean inertial motions: The sensitivity to surface wind fields. *Geophysical Research Letters*, **32**, doi:10.1029/2005GL023 289.

Jochum, M., B. Briegleb, G. Danabasoglu, W. Large, S. Jayne, M. Alford, and F. Bryan, 2013: On the impact of oceanic near-inertial waves on climate. *Journal of Climate*, doi:10.1175/JCLI–D–12–00 181.1.

Jungclaus, J., et al., 2013: Characteristics of the ocean simulations in mpiom, the ocean component of the mpi earth system model. *Journal of Advances in Modeling Earth Systems*, **5**, doi:10.1002/jame.20 023.

Kalnay, E., et al., 1996: The ncep/ncar 40-year reanalysis project. *Bulettin of American Meteorological Society*, **77**, 437–470.

Kantha, L., C. Tierney, J. Lopez, S. Desai, M. Parke, and L. Drexler, 1995: Barotropic tides in the global oceans from a nonlinear tidal model assimilating altimetric tides. 1. model description and results; 2. altimetric and geophysical implications. *Journal of Geophysical Research*, **25**, doi:10.1029/95JC02 577.

Klein, P., G. Lapeyre, and W. Large, 2004a: Wind ringing of the ocean in presence of mesoscale eddies. *Geophysical Research Letters*, **31**, doi:10.1029/2004GL020 274.

Klein, P., S. Smith, and G. Lapeyre, 2004b: Organization of near-inertial energy by an eddy field. *Quarterly Journal of the Royal Meteorological Society*, **130**, doi:10.1256/qj.02.231.

Kuhlbrodt, T., A. Griesel, M. Montoya, A. Levermann, M. Hofmann, and S. Rahmstorf, 2007: On the driving processes of the atlantic meridional overturning circulation. *Reviews of Geophysics*, **45**, doi:2004RG000 166.

Large, W. and G. Crawford, 1995: Observations and simulations of upper-ocean response to wind events during the ocean storms experiment. *Journal of Physical Oceanography*, **25**, doi:http://dx.doi.org/10.1175/1520–0485(1995)025<2831:OASOUO>2.0.CO;2.

Leaman, K. and T. Sanford, 1975: Vertical energy propagation of inertial waves: a vector spectral analysis of velocity profiles. *Journal of Geophysical Research*, **80**, doi:10.1029/JC080i015p01 975.

Levitus, S., 1982: Climatological atlas of the world ocean. *NOAA Professional Paper*, **13**, 173.

MacMillan, D., D. Beckley, and P. Fang, 2004: Monitoring the topex and jason - 1 microwave radiometers with gps and vlbi wet zenith path delays. *Marine Geodesy*, **27**, doi:10.1080/014904104909047 80.

Marsland, S., H. Haak, J. Jungclaus, M. Latif, and F. Röske, 2003: The max-planck-institute global ocean/sea ice model with orthogonal curvilinear coordinates. *Ocean Modelling*, **5**, doi:10.1016/S1463–5003(02)00 015–X.

Mellor, G. and A. Blumberg, 2004: Wave breaking and ocean surface layer thermal response. *Journal of Physical Oceanography*, **34**, doi:http://dx.doi.org/10.1175/2517.1.

Müller, M., 2013: On the space- and time-dependance of barotropic-to-baroclinic tidal energy conversion. *Ocean Modelling*, **72**, doi:10.1016/j.ocemod.2013.09.007.

Munk, W., 1966: Abyssal recipes. *Deep-Sea Research*, **13**, doi:10.1016/0011–7471(66)90 602–4.

Munk, W., 1981: Internal waves and small-scale processes. *Evolution of physical oceanography*, 264–291.

Munk, W. and C. Wunsch, 1998: Abyssal recipes ii: energetics of tidal and wind mixing. *Deep Sea Research*, **45**, doi:10.1016/S0967–0637(98)00 070–3.

Nikurashin, M. and R. Ferrari, 2010: Radiation and dissipation of internal waves generated by geostrophic flows impinging on small-scale topography: Application to the southern ocean. *Journal of Physical Oceanography*, **40**, doi:10.1175/2009JPO4199.1.

Nikurashin, M. and R. Ferrari, 2011: Global energy conversion rate from geostrophic flows into internal lee waves in the deep ocean. *Geophysical Research Letters*, **38**, doi:10.1029/2011GL046 576.

Niwa, T. and T. Hibiya, 1999: Response of the deep ocean internal wave field to traveling midlatitude storms as observed in long-term current measurements. *Journal of Geophysical Research*, **104**, doi:10.1029/1999JC900 046.

Olbers, D., J. Willebrand, and C. Eden, 2012: *Ocean dynamics*. Springer, 704 pp.

Pacanowski, R. and S. Philander, 1981: Parametrization of vertical mixing in numerical models of tropical oceans. *Journal of Physical Oceanography*, **11**, doi:http://dx.doi.org/10.1175/1520–0485(1981)011<1443:POVMIN>2.0.CO;2.

Plueddemann, A. and J. Farrar, 2006: Observations and models of the energy flux from the wind to mixed layer inertial currents. *Deep Sea Research II*, **53**, doi:10.1016/j.dsr2.2005.10.017.

Rimac, A., J.-S. von Storch, C. Eden, and H. Haak, 2013: The influence of high-resolution wind stress field on the power input to near-inertial motions in the ocean. *Geophysical Research Letters*, **40**, doi:10.1002/grl.50 929.

Saha, S., et al., 2010: The ncep climate forecast system reanalysis. *Bulletin of the American Meteorological Society*, **91**, doi:10.1175/2010BAMS3001.1.

Sandström, J., 1908: Dynamische versuche mit meerwaser. *Annls in Hydrodynamic Marine Meteorology*, 6.

Sandström, J., 1916: Meteorologische studien im schwedischen hochgebirge. *Göteborgs Kungl. Vetenskaps- och Vitterhetssamhälles Handlingar*, **7**, 1–48.

Silverthorne, K. and J. Toole, 2009: Seasonal kinetic energy variability of near-inertial motions. *Journal of Physical Oceanography*, **39**, doi:http://hdl.handle.net/1721.1/52317.

Simmons, H. and M. Alford, 2012: Simulating the long-range swell of internal waves generated by ocean storms. *Oceanography*, **25**, doi:http://dx.doi.org/10.5670/oceanog.2012.39.

Simmons, H., R. Hallberg, and B. Arbic, 2004: Internal wave generation in a global baroclinic tide model. *Deep Sea Research, Part II*, **51**, doi:10.1016/j.dsr2.2004.09.015.

Steele, M., M. Morley, and W. Ermold, 2001: Phc: A global ocean hydrography with a high quality arctic ocean. *Journal of Climate*, **14**, doi: http://dx.doi.org/10.1175/1520–0442(2001)014<2079:PAGOHW>2.0.CO;2.

Stern, M., 1975: *Ocean circulation physics*. Academic Press, New York, New York, 246 pp.

St.Laurent, L. and H. Simmons, 2006: Estimates of power consumed by mixing in the ocean interior. *Journal of climate*, **19**, 4877–4890.

Stull, R., 1988: *An introduction to boundary layer meteorology*. Springer, Milton Keynes, United Kingdom, 669 pp.

Tandon, A. and C. Garrett, 1994: Mixed layer restratification due to a horizontal density gradient. *Journal of Physical Oceanography*, **24**, doi:http://dx.doi.org/10.1175/1520–0485(1994)024<1419:MLRDTA>2.0.CO;2.

von Storch, H. and F. Zwiers, 1999: *Statistical analysis in climate research*. Cambridge University press, Edinburgh, United Kingdom, 484 pp.

von Storch, J.-S., 2010: Variations of vertical velocity in the deep oceans simulated by a 1/10° ogcm. *Ocean Dynamics*, **60**, doi:10.1107/s10236–010–0303–5.

von Storch, J.-S., C.Eden, I. Fast, H. Haak, D. Hernandez-Deckers, E. Maier-Reimer, J. Marotzke, and D. Stammer, 2012: An estimate of the lorenz energy cycle for the world ocean based on the 1/10° storm/ncep simulation. *Journal of Physical Oceanography*, **42**, doi:10.1175/JPO–D–12–079.1.

von Storch, J.-S., H. Sasaki, and J. Marotzke, 2007: Wind-generated power input to the deep ocean: An estimate using a 1/10° general circulation model. *Journal of Physical Oceanography*, **37**, doi:10.1175/JPO3001.1.

Watanabe, M. and T. Hibiya, 2002: Global estimates of the wind-induced energy flux to inertial motions in the surface mixed layer. *Geophysical Research Letters*, **29**, doi:10.1029/2001GL014422.

Weller, R., 1982: The relation of near-inertial motions observed in the mixed layer during the jasin (1978) experiment to the local wind stress and to the quasi-geostrophic flow field. *Journal of Physical Oceanography*, **12**, doi: http://dx.doi.org/10.1175/1520–0485(1982)012<1122:TRONIM>2.0.CO;2.

Wunsch, C., 1998: The work done by the wind on the oceanic general circulation. *Journal of Physical Oceanography*, **28**, doi: http://dx.doi.org/10.1175/1520–0485(1998)028<2332:TWDBTW>2.0.CO;2.

Wunsch, C. and R. Ferrari, 2004: Vertical mixing, energy, and the general circulation of the oceans. *Annual Review of Fluid Mechanics*, **36**, doi:10.1146/annurev.fluid.36.050802.122121.

Zhai, X., R. Greatbatch, and C. Eden, 2007: Spreading of near-inertial energy in a 1/12° model of the north atlantic ocean. *Geophysical Research Letters*, **34**, doi:10.1029/2007GL029895.

Zhai, X., R. Greatbatch, C. Eden, and T. Hibiya, 2009: On the loss of wind-induced near-inertial energy to turbulent mixing in the upper ocean. *Journal of Physical Oceanography*, **39**, doi:10.1175/2009JPO4259.1.

Zhai, X., R. Greatbatch, and J. Zhao, 2005: Enhanced vertical propagation of storm-induced near-inertial energy in an eddying ocean channel model. *Geophysical Research Letters*, **32**, doi:10.1029/2005GL023643.

Zhai, X., H. Johnson, and D. Marshall, 2010: Significant sink of ocean eddy energy near western boundaries. *Nature Geoscience*, **3**, doi:10.1038/ngeo943.

Zhai, X. and D. Marshall, 2013: Vertical eddy energy fluxes in the north atlantic subtropical and subpolar gyres. *Journal of Physical Oceanography*, **43**, doi: http://dx.doi.org/10.1175/JPO–D–12–021.1.

Acknowledgments

This thesis does not only contain three years of my work at the keyboard, but also memories that are closely linked to people with whom I have built and shared my life here. There are number of people whom I would like to express my gratitude to, because without them this thesis would never seen the light of the day and I would not be the person I am today.

First and foremost I would like to thank my advisor, Jin-Song von Storch for introducing me to the fascinating world of ocean energetics. Thank you for your guidance, for your support, for always having your office door opened for discussions and for your patience in answering my questions. I would also like to thank my coadvisor, Carsten Eden for his constructive comments and tremendous knowledge about ocean physics. Thanks to Bjorn Stevens for serving as my panel chair and for maintaining my panel meeting highly relaxed but always focused on a perspective of finishing the project. I thank the rest of my thesis committee, Johanna Baehr, Markus Jochum and Valerio Lucarini for evaluating my work and for giving it fair and honest judgement. Special thanks to Martin Claussen for stepping in as a committee member shortly before the defense. Since I did not have a nerves breakdown that day I probably never will.

Throughout these three years I had the chance to be the part of the IMPRS. This thesis would not be possible without the support of Antje. Thank you for always having time to listen to my complains. More importantly thank you for not allowing me to quit when I had the hardest time and for constantly reminding me about the importance of finishing my PhD. Thank you, Conni, Wiebke and Christina for providing great support for all the bureaucratic things needed for my living here. Angela, thanks for providing me moral support throughout my PhD.

Preparing the data for experiments and running the model was much easier with help of Helmuth Haak. Thank you for your in-depth knowledge about the ocean model and for being available every time I had a question, no matter how stupid it might have been.

I am very grateful to the members of the Ocean Department. Special thanks to my office-mate, Laura. You have seen all my tears and laughs over the past three years, and thank you for your kind words of support when I needed them. Also, thank you for introducing me to NCL and Latex, and for proofreading this thesis and all my former reports. Thanks to Eleftheria and Daniel Hernandez, my former group-mates, for their encouragements and long distance support.

Big thank you to Mirjana, Vladimir, Bart and Suvi. You were my family here and thanks for allowing me to be myself around you. And of course, thanks to many others that made my life nicer at the institute. Among them are Mathias, Florian, Francesco, Fabio, Alberto 2x, Juan-Pedro, Levi and Brittany, Jan, Josi, Rosi, Steffen by IMPRS buddy, Cedrick, Ritthik, Daniela and Linda, and others whom I forgot now. Thanks to IMPRS interview committee for recognizing that even a girl coming from a small scientific community has a will and attitude to finish PhD. Thanks to Jochem Marotzke for allowing me to be the part of the Ocean Department. Special thanks to Mirko Orlić and Branko Grisogono for writing letters of support for my application.

I am greatly indebted to my family, my mother Đurđica, brother Stipe and sister Željka, for the unconditional support they gave me throughout my life. Mom, your high regard for education and your encouragement to always perform more no matter what I do is probably why I pursued a PhD. Thank you for guiding me through my life and for making me the person I am. Stipe and Željka, thanks for every second of your life shared with me. Thanks for all the conversations, all the laughs and fights, but more importantly thanks for your infinite love and for being true brother and sister to me. Thanks to all my cousins, aunts and uncles for their support through my life.

Thank you, Chiel, for being by myside through my life in Hamburg. Thanks for always supporting me and believing in me. Thanks to Netteke and Peter for always welcoming me in your home, for introducing me to Dutch cuisine and for spending numerous hours watching tokkie tv with me. Nu is het tijd om te leren Nederlands te leren en zuurkool te leren bereiden.

There is a great deal of people whose English is not their strongest point, or I simply want to thank them in my own language, so I will switch to Croatian now. Hvala Josipu Oreškoviću, čovjeku koji je postavio temelje mojoj privrženosti fizici. Da nije bilo Vašeg entuzijazma i ponekad torture, ja vjerojatno nikad nebi studirala fiziku. Veliko hvala Prof. Mirku Orliću i Prof. Branku Grisogonu. Prof. Orliću, hvala Vam što ste me naučili da ocean nije samo nakupina kapi nego živi sistem. Prof. Grisogono, hvala Vam što ste me naučili da skromnost, entuzijazam i upornost vode do pravih rezultata. Hvala Vam na podršci i ohrabrenju tokom prijave na moj PhD.

Hvala mojim prijateljima i kolegama koji su djelili sve moje avanture ali i slušali moje bezgranične gluposti o svijetu i životu općenito. Slonica Gogica, hvala ti što postojiš jer bez tebe moj mali svijet nebi bio isti. Marina, hvala što si samnom djelila školsku klupu i znanje tokom testova pune četiri godine. Hvala ti na tvojoj iskrenosti i energiji koja zraći gdje god da se pojaviš. Sanja, hvala ti što si bila moja prva prava prijateljica. Djetinjstvo uz tebe i naše igre bilo je puno smijeha i zabave. Danijela, hvala ti što si ušla u moj život i što si uvijek spremna na razgovor pa makar i ako trebalo samo tračati Petra. Petre, iako si danas velečasni, za mene ćeš uvijek biti onaj klinac iz vrtića koji nije znao vezati cipele. Hvala ti na svim molitvama i podršci zadnjih godina. Hvala svima ostalima koji su bar malo utjecali na moj život. Hvala Veronika sto si bila najbolja cimerica na svijetu. Hvala Ivanu, Ivi, Mii, Ivici, Goranu, Josipu, Andreju, Lovri, Ani, Radi, Nikoli i ostalim kolegama s PMF-a i mojim kolegama iz 4E razreda. Veliko hvala djelatnicima Druge Gimnazije Varaždin i ravnateljici Zdravki Grđan. Vi ste me primili u školu kada mi je ne samo materijano nego i psihički bilo najteže, i pokazali ste mi da je zanimanje profesora plemenito i premalo cijenjeno, stoga hvala Vam. Hvala Mladenu Plačku i Nikoli Slunjskom što su učinili svaki odmor zanimljivim i zabavnim.

Posebno hvala ljudima koji su meni i mojoj obitelji financijski i moralno pomogli da početak mog života u Hamburgu bude laksi. Zahvaljujem teti Mladenki, teti Andreji, teti Karmen i obitelji Petrović, teti Miri, Velečasnom Stjepanu Najmanu i Sestri Heleni.

Mama, Stipe i Željka, ova dizertacija je za vas. Mama, hvala ti što si žrtvovala svoj život da bi ja i moja braća mogli biti obrazovani. Hvala ti što si svoju djecu uvijek stavljala ispred sebe i što si u svojoj nesebičnosti našu sreću stavljala ispred svoje. Stipe i Željka hvala vam što ste tako jednostavni a opet savršeni. Hvala vam na svakom razgovoru, svakoj svađi, svakoj igri i svakom trenutku provednom zajedno. Hvala vam što ste moji brat i sestra.

In the end, I would like to dedicate this thesis to my deceased father, Ante. You were gone too early for us to ever meet but memories from other people make you alive for me and our family. I am forever proud to be called your daughter.

Eidesstattliche Versicherung

Declaration on oath

Hiermit erkläre ich an Eides statt, dass ich die vorliegende Dissertationsschrift selbst verfasst und keine anderen als die angegebenen Quellen und Hilfsmittel benutzt habe.

I hereby declare, on oath, that I have written the present dissertation by my own and have not used other than the acknowledged resources and aids.

Hamburg, den

Hinweis / Reference

Die gesamten Veröffentlichungen in der Publikationsreihe des MPI-M
„Berichte zur Erdsystemforschung / Reports on Earth System Science“,
ISSN 1614-1199

sind über die Internetseiten des Max-Planck-Instituts für Meteorologie erhältlich:
http://www.mpimet.mpg.de/wissenschaft/publikationen.html

All the publications in the series of the MPI -M
„Berichte zur Erdsystemforschung / Reports on Earth System Science“,
ISSN 1614-1199

are available on the website of the Max Planck Institute for Meteorology:
http://www.mpimet.mpg.de/wissenschaft/publikationen.html